THE TRANSITION FROM INTERNAL OXIDATION TO EXTERNAL OXIDATION IN SILVER-ZINC ALLOYS

By

MICHAEL NICKOLAS LESYCHYN, B.ENG.

A Thesis

Submitted to the School of Graduate Studies

in Partial Fulfilment of the Requirements

for the Degree

Master of Engineering

McMaster University

March 1980

THE TRANSITION FROM INTERNAL OXIDATION TO EXTERNAL OXIDATION IN SILVER-ZINC ALLOYS

MASTER OF ENGINEERING (1980) McMaster University
(Metallurgy and Materials Science) Hamilton, Ontario

TITLE: The transition from internal oxidation to external oxidation in silver-zinc alloys

AUTHOR: Michael Nickolas Lesychyn, B.Eng. (McMaster University, 1978)

SUPERVISORS: Professors W. W. Smeltzer and G. R. Purdy

NUMBER OF PAGES: xii, 165

ABSTRACT

The investigation concentrates on the morphology of the oxidation products produced in Ag-1.8, 7.5, 10.9, 12.9 and 18.7 wt % Zn alloys at 550°C under an oxygen pressure of 1 atm. Particular attention is given to the structure of the internal ZnO produced and the morphological development of the internal precipitation zone in the alloys containing Ag-1.8, 7.5 and 10.9 wt % Zn. Penetration depth of the internal ZnO was measured using a light microscope, and was observed to obey the parabolic law. A model based on volume diffusion control of oxygen has been proposed for the velocity of the internal ZnO precipitates.

The Ag-12.9 wt % Zn alloy was observed to form an internal ZnO scale in combination with an external ZnO scale. An exclusive protective external scale of ZnO is formed on the Ag-18.7 wt % Zn alloy. The growth of the scale was found to obey parabolic kinetics. The morphological development of the external ZnO on the above alloys has also been studied.

The theoretical basis for the transition from internal to external scale formation has been given according to the Wagner[26] criteria for binary alloys.

It was necessary to extend the Wagner binary treatment for the transition into a ternary thermodynamic and diffusion analysis. A portion of the Ag-Zn-O ternary isotherm has been proposed, thus making possible the placement of representative diffusion paths.

ACKNOWLEDGEMENTS

Grateful acknowledgement is made to Dr. W. W. Smeltzer for suggesting the problem, guidance and advice during all stages of the project. Appreciation and thanks are also made to Dr. G. R. Purdy for his interest and stimulating discussion concerning the internal oxide morphology and also for acting as supervisor of the project during Dr. Smeltzer's sabbatical leave.

The author also wishes to thank the technical staff and graduate students in the oxidation group for their help and stimulating discussions. In particular, thanks are due to Messrs. D. Hodgson, J. Hudack, H. Neumayer, M. Van Oosten, F. Pearson and F. Smith. Thanks are also due to Mrs. H. Kennelly for typing the manuscript.

The author would also like to thank Luba, his wife, for her understanding and constant encouragement during the course of the project.

This project was supported by a graduate fellowship from the Department of Metallurgy and Materials Science of McMaster University and the National Research Council for the research grant to Dr. Smeltzer.

TABLE OF CONTENTS

LIST OF FIGURES

LIST OF TABLES

CHAPTER I

INTRODUCTION

Internal oxidation is a process whereby precipitates of the alloying element oxide are observed to form at an advancing reaction front within the solvent metal matrix. The process is generally a diffusion controlled phenomenon, for which the diffusion equations can be solved using numerical or analytical techniques to predict the reaction kinetics. Internal oxidation is classified into two categories, the first with and a second without external scale formation. These different categories have been established for the oxidation of dilute solid solution alloys composed of a solvent metal such as Ag, Cu, Ni and Fe, with a small content of a less noble alloying element, such as In, Be, Cr, Mn, Si, Al or Zr[1].

Internal oxidation is usually undesirable because its occurrence results in a depletion of the alloying element within the internal oxidation zone. This may result in accelerated (non-protective) oxidation which can lead to a change in the alloy microstructural and mechanical properties. The most extensively examined mechanical property is hardness[2,3,4,5]. Creep[6,7,8] processes have also been examined.

Finely dispersed oxides such as ThO_2, Al_2O_3, CeO_2,

Y_2O_3 and oxides of other rare earth metals greatly enhance the oxidation properties of alloys based on Ni-Cr, Co-Cr, or Fe-Cr at temperatures above 800°C[9]. These dispersed oxides lower the chromium content necessary for exclusive external protective Cr_2O_3 scale formation and provide improved adhesion of a Cr_2O_3 scale to the substrate[9].

Silver-cadmium alloys are also worth mentioning due to their importance as medium duty electrical contact material. In these alloys the internal CdO precipitates reduce the strength of the welds which form between contacts and consequently the rate of arc erosion of the contact material[10].

Internal oxidation does occur in steels[11,12,13,14,15] and has the potential to affect both the properties of steels while being processed and during service. Processing problems fall into two classifications: (i) subsurface inclusions which introduce rolling (or forging) defects, and (ii) alloy losses which affect subsequent heat treatment. Significant internal oxidization during carburization may affect the life of a carburized component by redistribution of residual stress, production of non-martensitic transformation products and surface cracking due to severe grain boundary oxidation.

The objective of this research project is to study the transition from internal to external oxidation in Ag-Zn alloys. The following Ag-Zn alloys Ag - 1.8, 7.5, 10.9, 12.9 and 18.7 wt % Zn were oxidized at 550°C and under an oxygen pressure of 1 atmosphere. The morphological develop-

ment of the internal oxide, and the internal oxidation zone that occurs in the above alloys to where a protective external scale is formed is investigated. A number of experimental techniques have been used to identify, observe and collect data for the oxidation scales produced: alloy preparation, chemical analysis, metallographic preparation, optical and scanning electron microscopy, X-ray diffraction and X-ray energy dispersive analysis.

The internal and external scales of ZnO were observed to grow according to parabolic kinetics, and simple models for the growth of these two scales will be proposed. The Wagner[26] criteria for the transition from internal to external oxidation has been expanded from a binary oxidation model into a ternary oxidation model. This allows the calculation of a value ε_o^{Zn} which is required for the formation solely of an external scale (of ZnO) on a Ag - 18.7 wt % Zn alloy.

In the following chapter, the literature is reviewed and the relevant theory for internal oxidation is presented. Chapter 3 gives the experimental techniques and procedure used to obtain the experimental results. In Chapter 4, the experimental results are presented according to the oxidation products produced. The last major chapter, number 5, is a general discussion of the experimental observations and their correlation with scale growth models.

CHAPTER 2

LITERATURE REVIEW AND THEORY

2.1 Introduction

This chapter is divided into three major sections: i) Classical kinetic studies of internal oxidation, ii) ternary oxidation formalism and, iii) nucleation and growth (including morphological developments of internal oxides).

2.2 Classical Work in Internal Oxidation

2.2.1 The Phenomena

Generally, the process of internal oxidation in alloys occurs by the dissolution of atomic oxygen into the base metal at its external surface or at the metal/external scale interface. The dissolved oxygen diffuses inward through the solvent metal matrix (assuming no defects and large grain size) which contains a volume fraction of previously precipitated internal oxide particles. The internal oxidation front advances essentially perpendicular to the external surface since inward diffusion of oxygen and outward diffusion of the alloying element to the reaction front provide the reactants in concentrations which exceed the solubility product of the alloying element oxide in the metal matrix. A repeated process of nucleation and growth of the oxide

particles, generally results in an inward advance of the front at a decreasing rate following parabolic kinetics[1].

For internal oxidation to occur in a binary alloy during isothermal oxidation at constant oxygen pressure, the following conditions must be met:

i) The free energy of formation (per mole of oxygen) of the lowest oxide for the solvent metal must be less negative than the free energy of formation (per mole of oxygen) of the solute metal in the solvent matrix;

ii) To achieve the required activity of dissolved oxygen at the reaction front, the pure solvent metal must have a reasonable solubility and diffusivity for atomic oxygen at the oxidation temperature;

iii) The solute concentration of the alloy must be less than that required to achieve the transition from internal to external scale formation;

iv) At the initiation of oxidation, a surface or near-surface layer formed by chemical, mechanical or metallurgical preparation of the alloy surface must not prevent the dissolution of oxygen into the alloy or cause formation of an external scale[1].

2.2.2 Internal Oxidation in the Absence of External Scale Formation

Several investigators have derived relationships which describe the kinetics of internal oxidation, oxide formation and growth in the absence of an external scale. If diffusion control of oxygen and alloying element are maintained, the depth ζ of internal oxidation zone is a parabolic function of time. One usually assumes the formation of a stoichiometric oxide in the internal oxidation zone, zero solubility of the alloying element in the internal oxidation zone and zero solubility of oxygen in the bulk alloy at the oxidation front. These assumptions led C. Wagner[1] to postulate the following model, schematically shown in Figure 2.1.

In the alloy A-B, let A be the solvent and B the solute. If one assumes that the precipitating particles do not interfere with oxygen diffusion in the solvent metal, then for the profile of oxygen shown in Figure 2.1, Fick's second law can be written ($D_O \neq D_O(x)$):

$$\frac{\partial N_O}{\partial t} = D_O\left(\frac{\partial^2 N_O}{\partial^2 x}\right) . \qquad (2\text{-}1)$$

For the alloying element we can write also:

$$\frac{\partial N_B}{\partial t} = D_B \frac{\partial^2 N_O}{\partial^2 x} . \qquad (2\text{-}2)$$

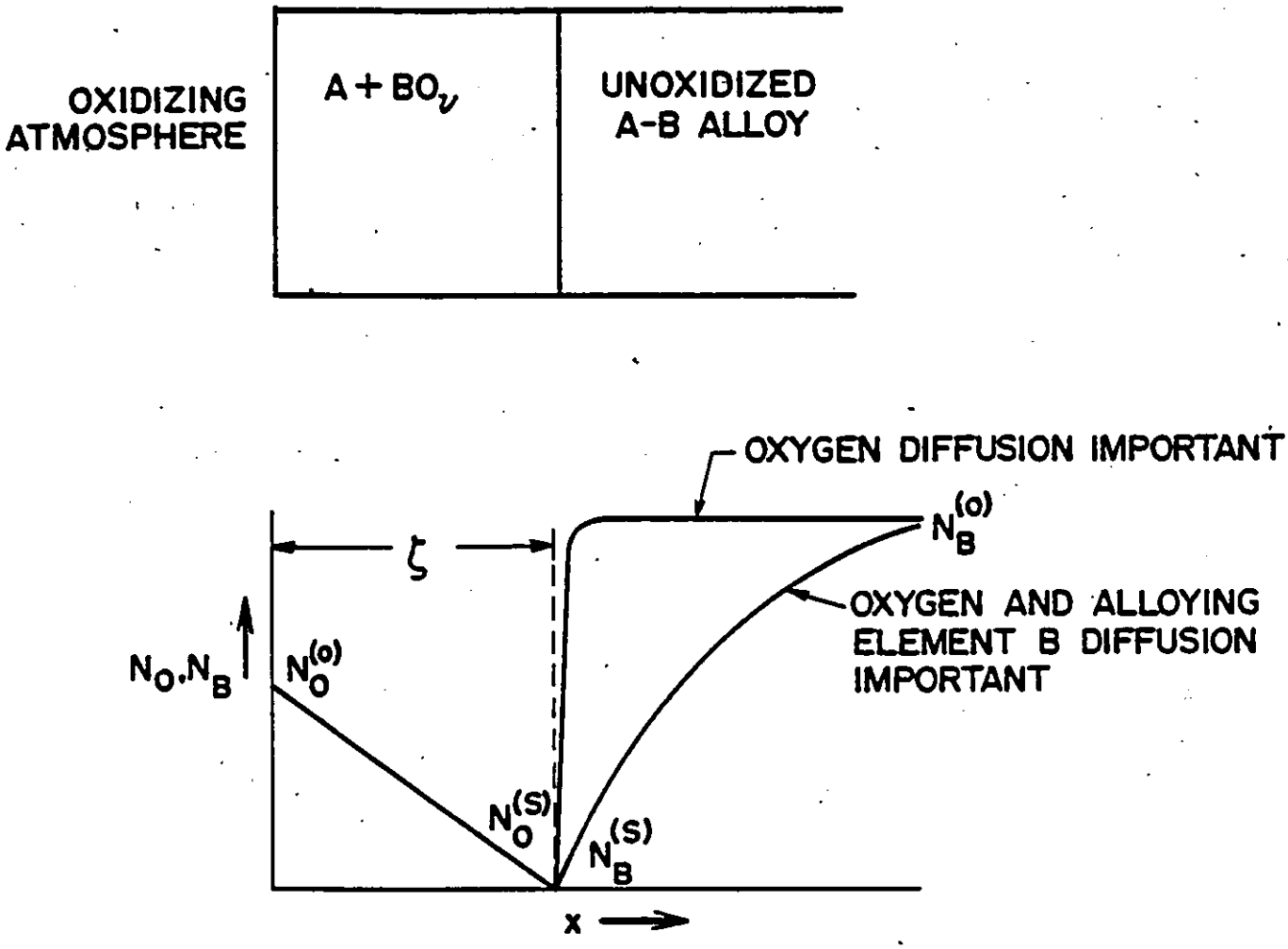

Figure 2.1 Steady-state concentration profiles for internally oxidized A-B alloy $A\text{-}B+\nu O \rightarrow A+BO_\nu$. (Ref. 1)

In these expressions, t is the time and the symbols are given in Figure 2.1. Using the appropriate boundary conditions from Figure 2.1, the solutions to (2-1) and (2-2) are:

$$N_O = N_O^O\{1 - \frac{\text{erf}[x/2(D_O t)^{1/2}]}{\text{erf}\ \gamma}\} \qquad (2\text{-}3)$$

$$N_B = N_B^O\{1 - \frac{\text{erfc}[x/2(D_B t)^{1/2}]}{\text{erfc}((\gamma\phi)^{1/2})}\} \qquad (2\text{-}4)$$

where $\phi = D_O/D_B$.

Upon equating the flux of oxygen and B atoms at the internal oxidation zone:

$$\lim_{\varepsilon\to 0}\{[-D_O(\frac{\partial N_O}{\partial x})_{x=\zeta-\varepsilon}] = [\nu D_B(\frac{\partial N_B}{\partial x})_{x=\zeta+\varepsilon}]\} \ . \qquad (2\text{-}5)$$

In (2-5) ν is the number of oxygen ions per B ion in the oxide Bo_ν. Substitution of (2-3) and (2-4) into (2-5) leads to:

$$\frac{N_O^O}{N_B^O} = \frac{\nu\ \exp(\gamma^2)\text{erf}(\gamma)}{\phi^{1/2}\exp(\gamma^2\phi)\text{erf}(\gamma\phi^{1/2})} \ . \qquad (2\text{-}6)$$

γ must be obtained from a graphical or numerical solution. If $\gamma << 1$ and $\gamma\phi^{1/2} >> 1$ which is equivalent to $\frac{D_B}{D_O} << \frac{N_O^{(o)}}{N_B^{(o)}} << 1$, equation (2-6) can be simplified to:

$$\gamma \cong [\frac{N_O^{(o)}}{2\nu N_B^O}]^{1/2} \ . \qquad (2\text{-}7)$$

Thus it can be easily shown:

$$\zeta = 2\left[\frac{N_o^{(o)}}{2\nu N_B^{(o)}}\right]^{1/2} [D_o t]^{1/2} \qquad (2\text{-}8)$$

and hence the velocity of the front:

$$V(\zeta) = \frac{d\zeta}{dt} = \left[\frac{N_o^o}{2\nu N_B^o}\right]^{1/2} [D_o/t]^{1/2} . \qquad (2\text{-}9)$$

Equations (2-8) and (2-9) are valid under the conditions that the inward penetration of the precipitation front is determined by the diffusion of oxygen in the solvent metal (Figure 2.1)[1].

In the second limiting case as in the first $\gamma << 1$, but now $\gamma\phi^{1/2} << 1$ which is equivalent to $N_o^o/N_B^o << D_B/D_o << 1$. Thus:

$$\gamma \cong \frac{\pi^{1/2}\phi^{1/2}N_o^o}{2\nu N_B^{(o)}} \qquad (2\text{-}10)$$

$$\zeta = \frac{\pi^{1/2}\phi^{1/2}\ N_o^o}{\nu N_B^o} (D_o t)^{1/2} . \qquad (2\text{-}11)$$

The concentration profile for B in this case is also given in Figure 2.1.

Many investigators[16,17,18,19] have shown the validity of equations (2-8) and (2-11), by studying such systems as Ag, Cu, Fe, and Ni alloys. For example, R. Rapp et al[20] have internally oxidized a series of dilute Ag-In alloys in air at temperatures between 500 and 800°C, and

derived the product $N_o D_o$ in (2-8) from measured values of ζ (and checked $N_o D_o$ from other techniques). Deviations from these ideal kinetics can occur for restricted solute mobility (lower temperatures), oxygen solubility in the internal oxidation zone and alloy, and finally for the precipitation of extremely stable internal oxides, leading to formation of non-stoichiometric solute-oxygen clusters[1].

Wagner[1] further introduced equations to calculate the degree of solute enrichment in the internal oxidation zone. If f is the mole fraction of solute B present as BO_ν in the internal oxide and v is the molar volume of solvent, then f/v is molar concentration of oxide BO_ν per unit volume. If the front advances $d\zeta$ in an area A in a time dt, thus in the volume element $Ad\zeta$, the number of moles of oxides BO_ν precipitating equals the number of moles of B arriving at the front through diffusion from $x > \zeta$, or

$$(\frac{f}{v})Ad\zeta = \lim_{\varepsilon \to 0} [\frac{D_B A}{v} (\frac{\partial N_B}{\partial x})_{x = \zeta + \varepsilon}]dt \quad . \qquad (2\text{-}12)$$

Upon substitution into equation (2-12) from (2-13) and

$$\frac{d\zeta}{dt} = \gamma (\frac{D_o}{t})^{1/2} \qquad (2\text{-}13)$$

$\frac{\partial N_B}{\partial x}$ from (2-4), and defining an enrichment factor α as f/N_B^o, the fraction of solute enrichment in the zone of internal oxidation can be calculated from:

$$\alpha = \frac{f}{N_B^O} = [\pi^{1/2}\phi^{1/2}\exp(\gamma^2\phi)\mathrm{erfc}(\gamma\phi^{1/2}]^{-1} \qquad (2\text{-}14)$$

under the conditions in Figure 2.1, oxygen diffusion important, negligible enrichment occurs. For the conditions in Figure 2.1 where both oxygen and alloying element (B) diffusion are important, an enrichment of solute as Bo_ν in the oxidizing zone results in a depletion of solute from the bulk alloy. At constant temperature and oxygen pressure during oxidation, the degree of solute enrichment is constant within the internally oxidized zone[1].

2.2.3 Internal Oxidation in Combination with External Scale Formation

Most practical systems susceptible to internal oxidation form external scales with the internal oxide below it. Rhines[21] and Maak[22] have developed a diffusion model for this case which is schematically represented in Figure 2.2[23].

The concentration of oxygen at metal/scale interface is set by dissociation pressure of AO_x oxide. One assumes here also that the solubility of B in the internal oxide is zero while the solubility of oxygen in the alloy at the precipitation front is also zero. The change in thickness (ζ-X) of internal oxide with time (assuming a constant oxygen gradient) is given by[23]:

$$\frac{d(\zeta-X)}{dt} = \frac{a}{(\zeta-X)} - b \qquad (2\text{-}15)$$

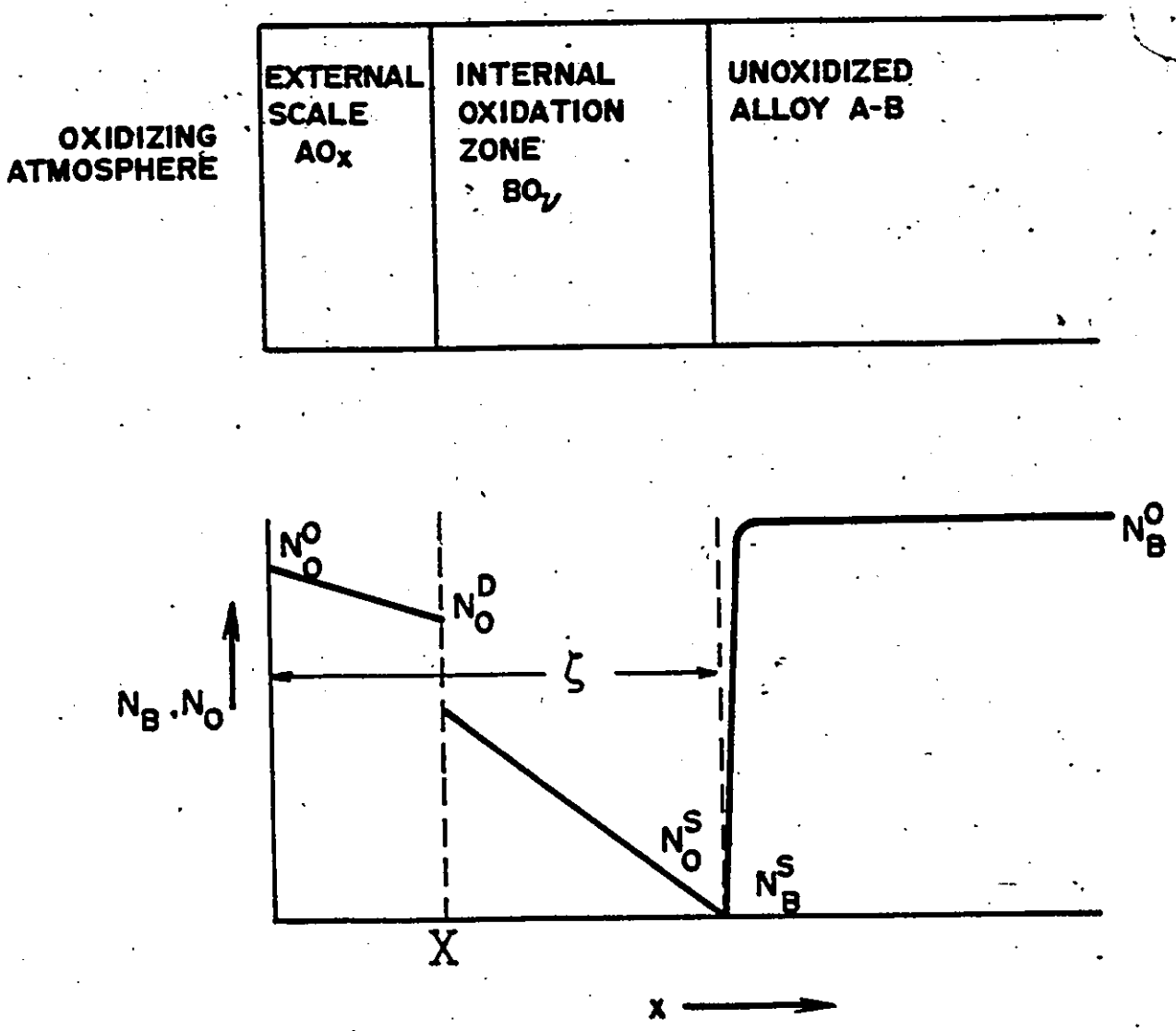

Figure 2.2 Steady-state concentration profiles for O and B in alloy with external and internal oxidation $A\text{-}B+xO+\nu O \rightarrow AO_x+BO_\nu$. (ref. 23)

where a and b are independent of time, and b is given by

$$\frac{dX}{dt} = b \quad . \qquad (2\text{-}16)$$

Equations (2-15) and (2-16) show that at the start of oxidation $a/\zeta - X$ will exceed b, and the thickness of the internal oxidation zone will increase. As the zone thickness increases, the first and second term become equal; thus the zone reaches limiting thickness of $(\zeta - X)$ equal to a/b. Now solving the diffusion equations to obtain the concentration profiles at steady-state for oxygen in the internal oxidation zone of $(\zeta - X)$ thickness and for solute B in the unoxidized alloy[23].

Thus for the 1-dimensional case using (2-1) and (2-2) and applying the appropriate boundary conditions* we obtain for oxygen and solute B:

$$N_O(x,t') = N_O^D\left\{\frac{\exp[-b/D_O(x-bt)]-\exp[-b/D_O(\zeta - X)]}{1-\exp[-b/D_O(\zeta - X)]}\right\} \qquad (2\text{-}17)$$

$$N_B(x,t') = N_B^O\{1-\exp[-(b/D_B)(x-bt-(\zeta - X))]\} \quad . \qquad (2\text{-}18)$$

Again for precipitation of BO_ν oxide at internal oxidation front, the flux of oxygen arriving at the front must be equivalent to the flux of solute B. Thus using (2-5) and substituting (2-17) and (2-1) into it, an equation in terms of $(\zeta - X)$ can be written[23].

---

*See Appendix 1, for detailed calculations of (2-17) and (2-18).

$$(\zeta - X) = -\frac{D_o}{b} \ln \frac{\nu N_B^o}{N_o^D + \nu N_B^o} . \qquad (2\text{-}19)$$

Equation (2-19) allows the evaluation of the constant a in equation (2-15):

$$a = -D_o \cdot \ln \left[\frac{\nu N_B^o}{N_o^o + \nu N_B^o}\right] . \qquad (2\text{-}20)$$

This equation predicts the steady-state width of an internal oxidation zone formed under an external scale which grows at a constant rate b. Once again the solute enrichment as BO_ν in the internal oxidation zone may be calculated. Using equation (2-12) and substitution of $\frac{d\zeta}{dt'} = \frac{dX}{dt'} = b$ from (2-16) and also differentiating (2-18) for $\partial N_B/\partial x$, the enrichment factor α is calculated to equal unity or:

$$\alpha = \frac{f}{N_B^o} = 1 . \qquad (2\text{-}21)$$

R. Rapp[23] has tested the model for Cb-Zr alloys at 1000°C and has found general agreement with his experimental results.

One can modify this model for external scales which follow the parabolic law by using:

$$X^2 = Kc2t \qquad (2\text{-}22)$$

for (2-16). Solving for this new case we obtain for the oxygen and the alloying element concentration profiles:

$$N_o = N_o^D\left\{\frac{\text{erf }\gamma - \text{erf}[x/2(D_o t)^{1/2}]}{\text{erf }\gamma - \text{erf}(K_c/2D_o)^{1/2}}\right\}$$

$$N_B = N_B^o\left\{1 - \frac{\text{erfc}[x/2(D_B t)^{1/2}]}{\text{erf}(\gamma\phi^{1/2})}\right\}. \qquad (2\text{-}24)$$

This model has been tested for copper-base alloys in several investigations[2,16,22,24]. For Cu-Al[24] and Cu-Be[22] the model was found to deviate for both the internal and external scale depths.

2.2.4 Kinetic Disturbances

An alloy which is under going internal oxidation and following equations (2-1), (2-2), (2-17), (2-18), (2-23) or (2-24) will deviate upon a change in temperature or oxygen pressure. Following a temperature or oxygen pressure change, the condition in (2-5) must remain constant, by a change in velocity of the precipitation front. The front may accelerate, decelerate or reverse the direction of its motion. Which effect occurs depends upon the kind and extent of change in temperature or oxygen pressure. If the precipitation front should reverse its direction of movement and temporarily recede toward the outer surface, a second reversal must occur later, after the new experimental conditions are satisfied[1].

A change in velocity $d\zeta/dt$ will result in a corresponding sudden change in (f/v), the molar concentration of BO_ν oxide particles per unit volume (2-12). When a reversal

in direction occurs $\frac{d\zeta}{dt} = 0$, an infinite molar concentration of the oxide is predicted by (2-12) (experimentally a large molar concentration is found). Thus by keeping $\frac{d\zeta}{dt} = 0$ in theory it would be possible to form a continuous internal oxide layer[1].

For Ag-In alloys, Rapp has calculated and tested a temperature-time program, designed to maintain $\frac{d\zeta}{dt} = 0$, so that a compact and protective band of In_2O_3 would form within the silver matrix. For alloys with $N^o_{In} \geq .077$, protection from further oxidation was achieved by these internal In_2O_3 bands. Bosch et al[25] attempted to form protective bands in Ag-Mg alloys by a pressure-time program but failed.

2.3 Ternary Representation of Internal Oxidation

2.3.1 Wagner Criteria for Internal Oxidation

The Wagner[26] criteria for internal oxidation will now be derived, with some modifications to the models in Figures 2.1 and 2.2. The boundary conditions at the alloy-scale interface have been changed to include solubility, see Figure 2.3.

$$N_o = N_o^S \neq 0 \quad , \quad x \geq \zeta \, , \; t > 0 \qquad (2\text{-}24)$$

$$N_B = N_B^{(S)} \neq 0 \, , \quad x \leq \zeta \, , \; t > 0 \, . \qquad (2\text{-}25)$$

The revised solution to Ficks' second law for the new boundary conditions are:

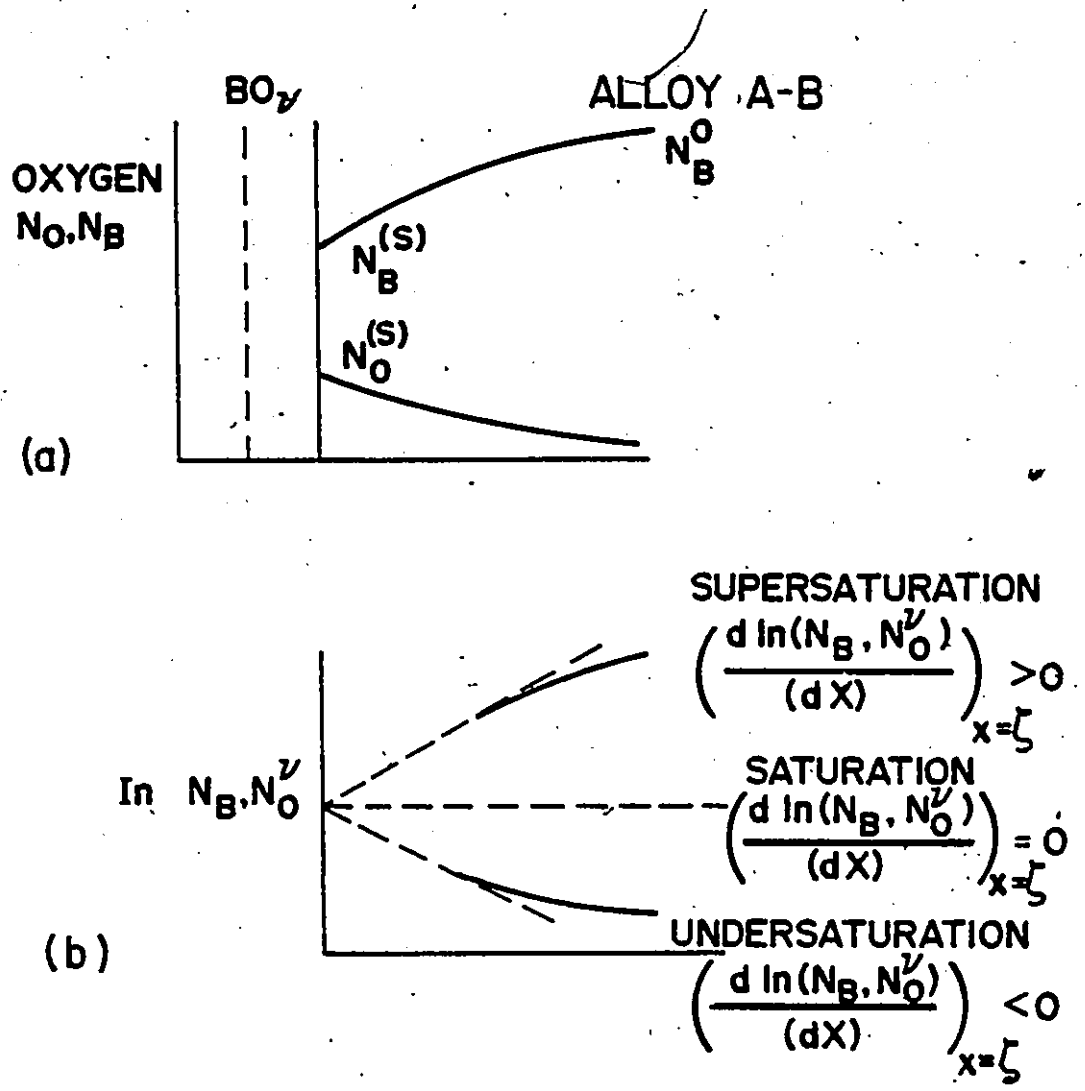

Figure 2.3 a) Cross-section showing concentration of solute B and oxygen in the underlying alloy.

b) The product $N_B \cdot N_O^\nu$ as a function of distance in the underlying alloy demonstrating the three possibilities. (Ref. 26)

$$N_B = N_B^o - (N_B^o - N_B^{(S)}) \frac{\operatorname{erfc}(x/2\sqrt{D_{AB} \cdot t})}{\operatorname{erfc}\sqrt{k/2D_{AB}}} \qquad (2\text{-}26)$$

$$N_o = N_o^{(S)} \frac{\operatorname{erfc}(x/2\sqrt{D_o t})}{\operatorname{erfc}(\sqrt{k/2D_o})} \quad , \quad x \geq \zeta \qquad (2\text{-}27)$$

In equations (2-26) and (2-27) the interdiffusion coefficients and k the corrosion constant are introduced. The position of the actual alloy surface ζ at any time is given by:

$$\zeta = (2kt)^{1/2} \; . \qquad (2\text{-}28)$$

Upon performing a mass balance at the alloy scale interface and substituting for N_B, N_o (26,27), one obtains:

$$N_B^{(S)} = \frac{N_B^o - F(\mu)}{1 - F(\mu)} \qquad (2\text{-}29)$$

where $\mu = (\frac{k}{2D_{AB}})^{1/2}$ and the auxilary function $F(\mu)$ is given by:

$$F(\mu) = (\pi)^{1/2} \exp \mu^2 \operatorname{erfc} \mu \; . \qquad (2\text{-}30)$$

The following equilibrium defines the relationship between the oxide and alloy components at the alloy/oxide interface:

$$BO_\nu = B(\text{alloy}) + \nu O(\text{alloy}) \qquad (2\text{-}31)$$

thus enabling a solubility constant K to be defined such that:

$$K = N_B^{(S)} \cdot N_o^{(S)\nu} \quad \text{at} \quad x = \zeta \; . \qquad (2\text{-}32)$$

Hence the criterion for internal oxidation then becomes whether $N_B \cdot N_O^{\nu} > K$ at positions within the alloy, away from the interface[26]. Using (2-26), (2-27), (2-30) and (2-32):

$$\partial/\partial x \, (N_B \cdot N_O^{\nu}) \quad \text{at} \quad x = \zeta \tag{2-33}$$

$$= \frac{2K}{\sqrt{\pi} 2\sqrt{D_{AB} t}} \left[\frac{(N_B^o - N_B^{(S)}) \exp(-k/2D_{AB})}{N_B^{(S)} \operatorname{erfc} \sqrt{k/2D_{AB}}} \right. \tag{2-34}$$

$$\left. \nu \left(\frac{D_{AB}}{D_o}\right)^{1/2} \frac{\exp(-k/2D_o)}{\operatorname{erfc} \sqrt{k/2D_o}} \right] .$$

The three possibility are shown in Figure 2.3; only when $[\partial/\partial x (N_B \cdot N_O^{\nu})]_{x=\zeta} > 0$ is internal oxidation possible. Equation (2-34) may be simplified because in most systems $D_o >> k$ and D_{AB} and hence[26]:

$$\operatorname{erfc}(\sqrt{k/2D_o}) \cdot \exp(k/2D_o) \geq 1 . \tag{2-35}$$

Thus the criteria for I.O. becomes:

$$\frac{N_B^{(o)} - N_B^{(S)}}{\nu N_B^{(S)}} \left(\frac{D_o}{D_{AB}}\right)^{1/2} \frac{\exp(-k/2D_{AB})}{\operatorname{erfc}\sqrt{k/2D_{AB}}} > 1 \tag{2-36}$$

$$N_B^{(o)} \geq \frac{F(\mu) + \frac{1}{\nu} \left(\frac{D_o}{D_{AB}}\right)^{1/2} u\pi^{1/2}}{1 + \frac{1}{\nu} \left(\frac{D_o}{D_{AB}}\right)^{1/2} u\pi^{1/2}} . \tag{2-37}$$

(no internal oxidation)

2.3.2 Ternary Representation of Wagner Criterion for Internal Oxidation

The oxidation model proposed by Wagner[1] may be placed into a ternary thermodynamic and diffusion formalism using A-B-O ternary isotherm and the placement of the representative diffusion paths on this isotherm. The oxidation model is given in Figure 2.3, while Figure 2.4 shows the possible diffusion paths on the ternary system.

Here three diffusion paths are considered. Path (1) is constructed as tangential to the oxygen solubility curve in the alloy, which is assumed to increase in slope with increasing A content of the alloy according to (2-32). Path (2) corresponds to the case for external scale formation accompanied by internal oxidation. Path (3) represents the case of internal oxidation only. The virtual diffusion path cuts into the two-phase BO_ν+alloy field leading to oxygen supersaturation, and hence nucleation of internal oxides[26].

If the slope of the solubility curve at the composition corresponding to the alloy/surface scale interface is obtained from (2-32) then:

$$\left(\frac{dN_O}{dN_B}\right)^{\text{solubility}}_{x=\zeta} = -\frac{N_O^{(S)}}{\nu N_B^{(S)}} . \qquad (2\text{-}38)$$

One can also get the gradient of the internal diffusion path DP, at the alloy/scale interface from

$$\left(\frac{dN_O}{dN_B}\right)^{DP}_{x=\zeta} \qquad (2\text{-}39)$$

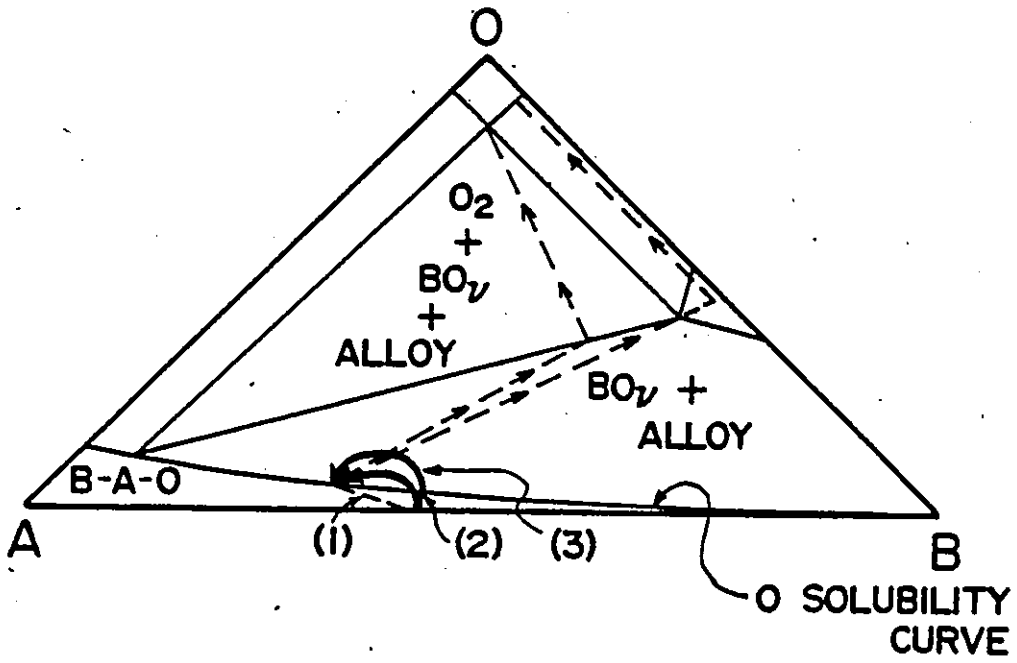

Figure 2.4 Diffusion path for metal and oxygen superimposed on A-B-O ternary isotherm. (Ref. 26)

$$\left(\frac{dN_O}{dN_B}\right)^{DP}_{x=\zeta} = \left(\frac{\partial N_O}{\partial x}\right) \Big/ \left(\frac{\partial N_B}{\partial x}\right)_{x=\zeta} \qquad (2\text{-}40)$$

and using the solutions for concentration profiles (2-26), (2-27) into (2-40) one obtains:

$$\left(\frac{dN_O}{dN_B}\right)^{DP}_{x=\zeta} = -\frac{N_O^{(S)}}{N_B^O - N_B^{(S)}} \left(\frac{D_{AB}}{D_O}\right)^{1/2} \frac{\operatorname{erfc}(k/2D_{AB})^{1/2}}{\exp(-k/2D_{AB})} \; . \qquad (2\text{-}41)$$

The gradients in (2-38) and (2-41) can be compared to define the condition of oxidation. Thus for internal oxidation to occur:

$$\left(\frac{dN_O}{dN_B}\right)^{DP}_{x=\zeta} \geq \left(\frac{dN_O}{dN_B}\right)^{\text{solubility}}_{x=\zeta} \; . \qquad (2\text{-}42)$$

substitution of (2-38) and (2-41) into (2-42)

$$\frac{N_O^{(S)}}{\nu N_B^{(S)}} \geq \frac{N_O^S}{N_B^0 - N_B^{(S)}} \left(\frac{D_{AB}}{D_O}\right)^{1/2} \frac{\operatorname{erfc}(k/2D_{AB})^{1/2}}{\exp(-k/2D_{AB})} \; . \qquad (2\text{-}43)$$

upon rearrangement of (2-43) arrive at (2-37)[26].

2.3.3 Ternary Diffusional Analysis of the Transition from Internal Oxidation to External Scale Formation

One can formulate a more general expression for the diffusion path criteria presented above, by introducing, the thermodynamics of oxygen solubility and its variation with composition. Secondly, the effect of thermodynamic interaction on the diffusion profiles in the alloy and hence on the

shape of the diffusion path can be introduced[26].

Liquid binary alloys, in which one element is selectively oxidized from the solvent metal exhibit a minimum in the oxygen solubility curve. Using the Wagner formalism for solution thermodynamics, St. Pierre[27] and Blackburn, Feldman[28] and Kirkaldy have derived solubility relations to interpret the experimental oxygen solubility curves in iron melts. A similar formalism can be used to interpret the oxygen solubility curves in solid binary alloys[26].

The oxide alloy equilibrium may therefore be written as:

$$A_\delta B_{1-\delta} O_\nu = (1-\delta)B + \delta A + \nu O \qquad (2\text{-}44)$$

where A is the solvent metal such that its concentration in the oxide is small ($\delta << 1$). If the activity of the oxide is constant $A_\delta B_{1-\delta} O_\nu$

$$\begin{aligned} \ell nK &= \ell n \; a_A{}^{\delta} B^{1-\delta} O^{\nu} \\ &= \ell n \; N_A{}^{\delta} N_B{}^{1-\delta} N_O{}^{\nu} + \ell n \gamma_A{}^{\delta} \cdot \gamma_B{}^{1-\delta} \gamma_O{}^{\nu} \end{aligned} \qquad (2\text{-}45)$$

where K is the equilibrium constant. The oxygen solubility curve for the alloy is then defined by:

$$\frac{d \; \ell nK}{d \; N_B} = 0 \; . \qquad (2\text{-}46)$$

If the dissolved oxygen concentration in the solvent metal A is very small, then the activity coefficients in (2-45).

can be expressed by:

$$\ell n\gamma_B = \ell n\gamma_B^o + \varepsilon_B^o N_o + \varepsilon_B^B N_B \qquad (2\text{-}47)$$

$$\ell n\gamma_o = \ell n\gamma_o^o + \varepsilon_o^o N_o + \varepsilon_o^B N_B \qquad (2\text{-}48)$$

$$\ell n\gamma_A = 0 \quad ; \quad N_A \simeq 1-N_B \; . \qquad (2\text{-}49)$$

Substituting (2-47), (2-48) and (2-49) in (2-45) and using (2-46) with $\varepsilon_o^B = \varepsilon_B^o$:

$$\{\frac{1-\delta}{N_B} - \frac{\delta}{1-N_B} + (1-\delta)\varepsilon_B^B + \nu\varepsilon_o^B\} + \{\frac{\gamma}{N_o} + (1-\delta)\varepsilon_o^B + \nu\varepsilon_o^o\} \frac{dN_o}{dN_B} = 0. \qquad (2\text{-}50)$$

Now the gradient of this solubility curve can be calculated at $x=\zeta$, the interface between alloy and growing scale of $\delta << 1$ and $N_B^S \lesssim 1$, the last equation becomes:

$$(\frac{dN_o}{dN_B})^{sol.}_{x=\zeta} = - \frac{N_o^S}{N_B^S} \; (\frac{1+N_B^S\varepsilon_B^B+\nu N_B^S\varepsilon_o^B}{\nu+N_o^S\varepsilon_o^B+\nu N_o^S\varepsilon_o^o}) \; . \qquad (2\text{-}51)$$

Equation (2-51) reduces to (2-38) if ε_B^B, ε_o^o, and ε_o^B are zero.

This equation (2-51) can be used to define the minimum in the oxygen solubility curve at this point $dN_o/dN_B = 0$.

$$N_B^* = - \frac{1}{\nu\varepsilon_o^B+\varepsilon_B^B} \qquad (2\text{-}52)$$

where N_B^* equals the atom fraction of B at minimum in solubility curve. For Henrian behavior $\varepsilon_B^B = 0$ thus:

$$N_B^* = - \frac{1}{\nu\varepsilon_o^B} \; . \qquad (2\text{-}53)$$

A distinction between Henrian and non-Henrian solution behavior is essential when coupling thermodynamic and diffusional parameters to interpret reaction kinetics. Where non-Henrian behavior occurs the slope of the oxygen solubility curve and coupling of diffusional fluxes on the two independent compositional profiles becomes significant[26].

2.3.4 The Ternary Oxidation Model

The diffusional model is given in Figure 2.5. The ternary oxide $A_\delta B_{1-\delta} O_\nu$ is assumed to correspond closely with the composition of binary oxide ($\delta << 1$) and oxygen solubility curve may exhibit a minimum.

Oxygen is the only component which is regarded as diffusing on both its own and on the metal gradient:

$$D_{OO} >> D_{BB} \text{ and } /\partial N_O/\partial x/ << /\partial N_B/\partial x/. \qquad (2\text{-}54)$$

The flux equations for the conditions in Figure 2.5 are

$$j_B = - D_{BB} \frac{\partial N_B}{\partial x} \qquad (2\text{-}55)$$

$$j_O = - D_{OO} \frac{\partial N_O}{\partial x} - D_{OB} \frac{\partial N_B}{\partial x}$$

$$= - D_{OO} \left(\frac{\partial N_O}{\partial x} + \varepsilon_O^B N_O \frac{\partial N_B}{\partial x}\right) \qquad (2\text{-}56)$$

where the dilute solution approximation has been substituted for off-diagonal diffusion coefficient D_{OB}:

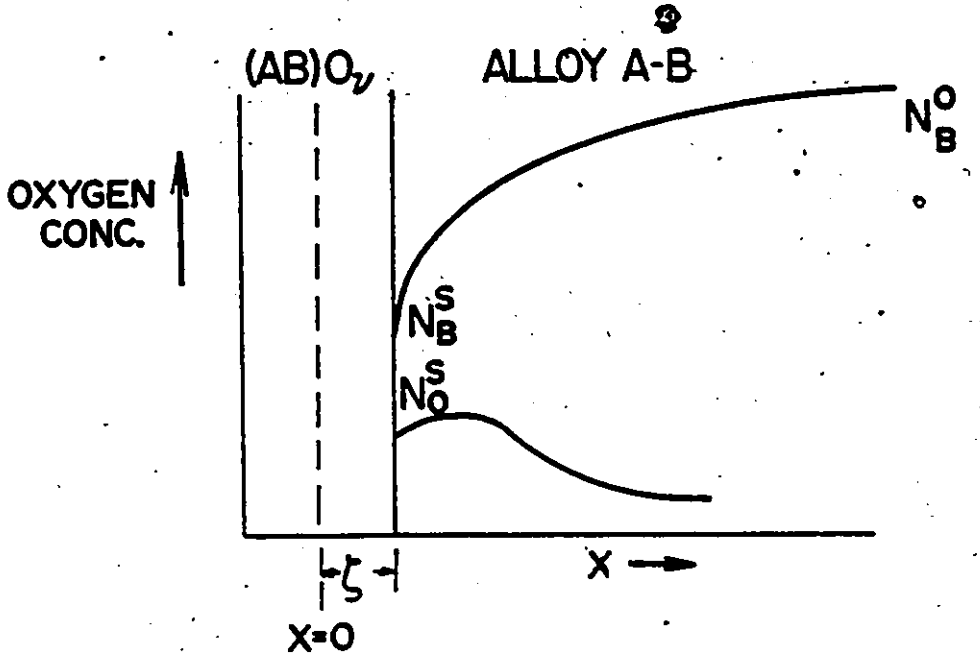

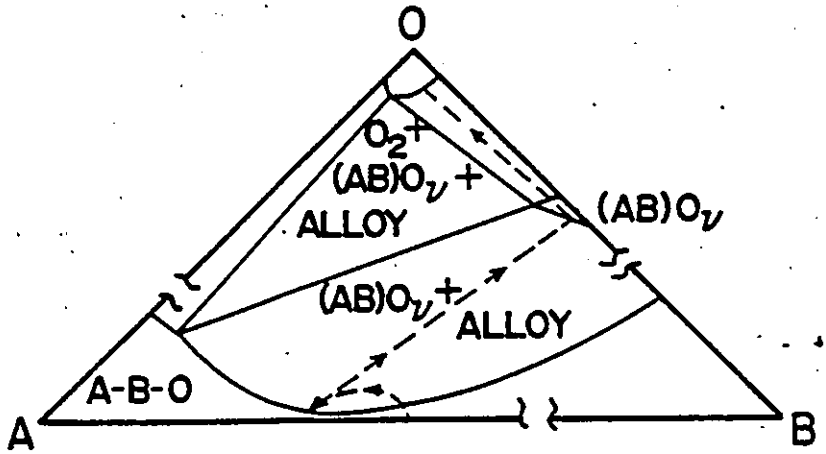

---- VIRTUAL DIFFUSION PATH

Figure 2.5 Ternary oxidation model. (Ref. 26)

$$D_{oB} = D_{oo}\varepsilon_o^B N_o \quad . \tag{2-57}$$

Assuming D_{BB} and D_{oo} are concentration independent then divergence of the fluxes may be written as:

$$\frac{\partial N_B}{\partial t} = \frac{\partial}{\partial x}\left(D_{BB}\frac{\partial N_B}{\partial x}\right) = D_{BB}\frac{\partial^2 N_B}{\partial^2 x} \tag{2-58}$$

$$\frac{\partial N_o}{\partial t} = \frac{\partial}{\partial x}\left|D_{oo}\left(\frac{\partial N_o}{\partial x} + \varepsilon_o^B N_o \frac{\partial N_B}{\partial x}\right)\right| \tag{2-59}$$

$$= D_{oo}\frac{\partial^2 N_o}{\partial 2_x} + D_{oo}\varepsilon_o^B \frac{\partial}{\partial x}\left(N_o \frac{\partial N_B}{\partial x}\right) \quad .$$

Since ternary interaction assumed not to influence B, then the solution to (2-58) is (2-26). The solution of the oxygen profile is given by Bolze et al[29] assumes off-diagonal coefficient D_{oB} and D_{oo} are constant, gives:

$$N_o = D_{oB}(N_B^o - N_B^S)\frac{\operatorname{erfc}(x/2\sqrt{D_{BB}t}}{\operatorname{erfc}((k/2D_{BB})^{1/2})} + N_o^S\frac{\operatorname{erfc}(x/2\sqrt{D_{oo}t})}{\operatorname{erfc}(k/2\,D_{oo})^{1/2}}$$

$$- \frac{D_{oB}}{D_{oo}}(N_B^o - N_B^S)\frac{\operatorname{erfc}(x/2\sqrt{D_{oo}t}}{\operatorname{erfc}((k/2\,D_{oo})^{1/2}} \tag{2-60}$$

where N_o^S is mole fraction of oxygen at the alloy/scale interface, which is also the oxygen solubility limit for an alloy of composition N_B^S. The gradient of oxygen profile at interface $x = \zeta$ is:

$$\left(\frac{\partial N_o}{\partial x}\right)_{x=\zeta} = \frac{N_B^o - N_B^S}{(\pi D_{oo}t)^{1/2}}\left\{\frac{D_{oB}}{D_{oo}} - \frac{D_{oB}}{(D_{oo}D_{BB})^{1/2}}\cdot\frac{\exp(-k/2\,D_{BB})}{\operatorname{erfc}(k/2\,D_{BB})^{1/2}} - \frac{N_S^o}{N_B^o - N_B^S}\right\} \tag{2-61}$$

Again approximation (2-35) is made: Proceeding as before for the slope of virtual diffusion path with off-diagonal approximation (2-57) we get:

$$\left(\frac{dN_O}{dN_B}\right)^{DP}_{x=\zeta} = -N_O^S\left(\frac{D_{BB}}{D_{OO}}\right)^{1/2}\frac{\operatorname{erfc}(k/2\ D_{BB})^{1/2}}{\exp(-k/2D_{BB})}\left\{\frac{1}{N_B^O-N_B^S}+\right.$$

$$\left. + \varepsilon_O^B\left(\frac{D_{OO}}{D_{BB}}\right)^{1/2}\cdot\frac{\exp(-k/2\ D_{BB})}{\operatorname{erfc}(k/2\ D_{BB})^{1/2}} - \varepsilon_O^B\right\} . \qquad (2\text{-}62)$$

Now use (2-42) with (2-51) to include oxygen interaction solubility. This tangent to the compositional profile of the virtual diffusion path has to be compared to the tangent to the solubility curve at the composition of the alloy scale interface (N_B^S, N_O^S) as given by (2-51). Equation (2-51) provides the limiting criterion for the transition from external scale formation accompanied with internal oxidation, to external ocidation formation only. For internal oxidation to occur (2-42) must be satisfied.

$$\frac{N_B^O-N_B^S}{N_B^S}\left(\frac{1+N_B^S\varepsilon_B^B+\nu N_B^S\varepsilon_O^B}{\nu+N_O^S\varepsilon_O^B+\nu N_O^S\varepsilon_O^B}\right)\left(\frac{D_{OO}}{D_{BB}}\right)^{1/2}\frac{\exp(-k/2\ D_{BB})}{\operatorname{erfc}(k/2\ D_{BB})^{1/2}}\{1/ \qquad (2\text{-}63)$$

$$1 + (N_B^O-N_B^S)\varepsilon_O^B\left[\left(\frac{D_{OO}}{D_{BB}}\right)^{1/2}\cdot\frac{\exp(-k/2\ D_{BB})}{\operatorname{erfc}(k/2\ D_{BB})^{1/2}} - 1\right]\} > 1$$

This equation (2-63) defines the limiting atom fraction of solute B above which internal oxidation of the alloy would not occur. Making the following simplification since ε_B^B and ε_O^O are generally much less than ε_O^B, $N_O^S \ll N_B^S$ one obtains:

$$\frac{1+\varepsilon_B^B N_B^S+\nu\varepsilon_O^B N_B^S}{\nu+\varepsilon_O^B N_O^S+\nu\varepsilon_O^O N_O^S} \cong \frac{1+\nu\varepsilon_O^B N_B^S}{\nu} \quad . \qquad (2\text{-}64)$$

Using (2-64) in (2-63) one obtains:

$$\frac{N_N^O - F(\mu)}{1-N_B^O} \geq \frac{\sqrt{\pi}}{\nu} u\sqrt{\frac{D_{OO}}{D_{BB}}} \left\{ \frac{1+\nu\varepsilon_O^B N_B^O - F(\mu)\,[1+\nu\varepsilon_O^B]}{1+\sqrt{\pi}u\varepsilon_O^B\sqrt{\frac{D_{OO}}{D_{BB}}}(1-N_B^O) - F(\mu)\,[\varepsilon_O^B(1-N_B^O)+1]} \right\} \qquad (2\text{-}65)$$

Where ideal behavior occurs $\varepsilon_O^B = 0$, (2-65) reduces to (2-37).

Smeltzer[26] and Whittle have recently put forth this ternary oxidation model for the transition from internal to external oxidation. The application of this model suffers from extreme limitations:

i) the lack of oxygen solubility data in solid binary alloys.

ii) very limited data are available for ternary interaction parameters (except for liquid iron alloys).

iii) lack of ternary A-B-O phase diagrams.

These limitations prevent any conclusion from the analysis to be made at the present time. Nevertheless, when studying internal oxidation one should try to apply ternary-Wagner formalism without solubility and ternary interaction data[26].

2.4 Formation and Growth of Internal Oxides

2.4.1 Nucleation and Growth

In most alloy systems exhibiting internal oxidation, classical nucleation[30,31] theory can be used for understanding the mechanisms by which internal oxides form. However, discoveries of internal oxide clusters less than 10 Å in diameter have been made within the last twenty years. Classical nucleation theory cannot provide any explanation of the mechanisms by which these oxides form. This topic will be discussed in the following section.

As mentioned in the introduction, a repeated process of nucleation and growth of the oxide particles is generally thought to occur at the internal oxidation front (ζ), resulting in an inward advance of the front. The oxygen and solute metal concentration profiles have been previously derived. Once the solubility product has been exceeded locally nucleation of internal oxides may occur at the front. On the microscopic scale at the internal oxidation front, there will be random fluctuations in the concentration profiles which may be represented by infinitely small sinusoidal perturbations[32].

The driving force for nucleation is the volume free energy change accompanying the transformation, ΔG_v, minus the volume strain energy arising from the size or shape misfit between the nucleus and matrix. The barrier to nucleation is the interfacial free energy of the nucleus:

matrix ΔG_S and ΔG_n^o for formation of an embryo with its three components is sketched in Figure 2.6. The driving force is obtained from the ternary free energy versus composition diagram by constructing planes tangent to the parent phase free energy curve at the bulk composition, (see Figure 2.7) and determining the vertical distance $V_{B_{1-x}A_xO}\Delta G$ to the precipitate composition and $\Delta\mu_1 = K\sigma V_A^{B_{1-x}A_xO}$, $\Delta\mu_2 = K\sigma V_A^{B_{1-x}A_xO}$, $\Delta\mu_3 = -K\sigma V_O^{B_{1-x}A_xO}$ where K is curvature, σ interfacial free energy and $V_i^{B_{1-x}A_xO}$ partial molar volume of i in the oxide precipitate[31].

Investigation of morphology and structure of nucleated internal oxide particles has mainly concentrated on the copper and silver solvent metal system. Ashby[33] and Smith have studied the internal oxides formed in dilute copper-silicon and dilute copper-aluminum alloys by T.E.M. In the Cu-Si system they found the oxides formed as amorphous silica particles in the size range of 15 - 50,000 Å (diameter). The shape of the particles were found to be spherical when located intergranularily while those located at grain boundaries were lenticular. Whether the particles nucleated coherently or incoherently was not determined. Growth of the particles by a vacancy mechanism led to incoherency of the particle with the matrix. The calculated energy of the copper/silica interface was determined to be between 1000 and 1200 ergs/cm^2. In the Cu-Al system, they

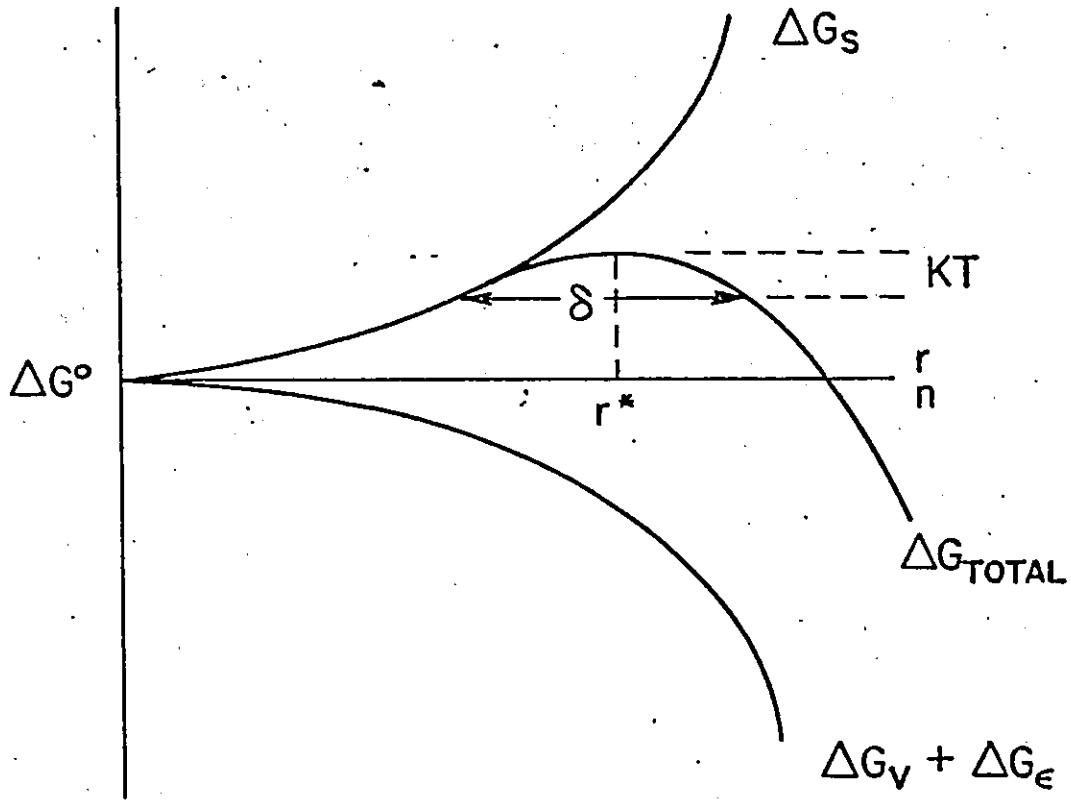

Figure 2.6 Variation of ΔG° for embryo formation with radius r and number of atoms in the embryo, n. (Ref. 30) (KT-thermal activation energy for fluctuations in nucleus of critical size δ).

Figure 2.7 Equilibrium construction for $B_{1-x}A_xO$ nuclei of critical size., with critical curvature K°. The alloy composition of $B_{1-x}A_xO$. ($O+xA+1-xB \rightarrow B_{1-x}A_xO$). (Model in Figure 2.5). (Ref. 31)

found internal oxides to form as crystalline γ-Al_2O_3 (cubic, spinel type, a = 7.9 Å) and occasionally α-Al_2O_3 was found. The particles nucleated coherently, with particle size being between 15 - 250 Å. The particles were rectangular in shape and the flat pieces of alumina particles lay parallel to {111} planes of copper matrix, with their edges parallel to <110> directions. The particles commenced to lose coherency at sizes > 35× 10 Å by the introduction of dislocation loops around the particle, thus relieving some of the elastic strain. Doneliya[38] et al, studied Cu-Al-Ti system and found agreement with the work of Ashby and Smith for internal oxides of aluminium.

Bolsaitis[35] and Kahlewit have examined dilute Cu-Si alloys, and have found that silica first forms as isolated dendritic internal oxides near the surface during the initial stages of oxidation. As growth proceeds these dendritic oxides transform to spherical geometry. The nature and shape of particles was not studied in detail.

Wood et al[36] have investigated dilute Cu-Ti alloys at temperatures in the 700 to 900°C by T.E.M. They postulated that the internal oxides first nucleated as coherent TiO (NaCl structure) and further oxidized to TiO_2 (rutile modification). The nature and extent of coherency loss of TiO_2 and the Cu matrix could not be completely evaluated. One of the reasons for this was due to the large mismatch between the matrix and TiO_2 structures. One would

expect coherency loss at a diameter of 30 Å, but coherent particles were found up to sizes of 200 Å. It was found that the larger particles remained coherent by forming certain faults which could not be identified. The particles were found to be nearly spherical with an interfacial energy in the range of 400 to 700 erg/cm^2.

Peddler[37] has recently examined a large number of Ag-Cd alloys. The internal oxide formed was CdO (NaCl type structure). The oxide particles nucleated as semi-coherent truncated octahedra bounded by {111} and {200} faces. The particle size was found to be in the range of 100 Å in diameter and as the particles grew larger they became fully incoherent. The interfacial energy between particle and matrix was found to be 450 erg/cm^2.

2.4.2 Internal Oxide Clusters

The formation of extremely small (< 10 Å) oxygen clusters has been investigated in a number of different systems[38,39,40]. Wriedt[38] and Darken oxidized dilute Ag-Al alloys (0.19 wt % Al) between 350°C - 850°C. Gravimetric measurements indicated an oxygen intake far greater than that required to form stoichiometric Al_2O_3; the ratio of excess oxygen increased with decreasing temperature and decreasing alloy content. Swann[39] et al, using both low-angle X-ray scattering and transmission electron microscopy, found at an oxidizing temperature of 800°C that the particles had a diameter in the range 30 to 140 Å. At

oxidizing temperatures less than 600°C, no clearly resolved particles are formed, and it was suspected that these clusters were less than 10 Å.

More recently D. J. Peddler[40] et al, have investigated clusters of internal oxides in Cu-0.3 wt % Si, Cu-0.05 wt % Si, Cu-0.05 wt % Al, and Cu-0.01 wt % Mg utilizing field ion microscopy. This technique was used because the oxides immediately below the surface in the internally oxidized samples were below the resolution limit of T.E.M. The mean particle diameters were determined to be Cu-0.05 wt % Si - 700°C - 17 Å, Cu-0.05 wt % Al - 800°C - 2.7 Å, and Cu-0.1 wt % Mg - 800°C - 1.5 Å.

Some of the conditions necessary for form these minute clusters are:

i) low affinity of the solvent metal for oxygen,

ii) high affinity of the solute metal for oxygen,

iii) a high diffusivity and mobility of oxygen in the solvent metal (which is interstitial) at the oxidizing temperature

iv) a low diffusivity and mobility of the solute in the solvent (which is substutional) metal at the oxidizing temperature.

v) the ratio of iii) and iv) increases greatly as temperature is decreased.

An example of this type of system would be Ag-Al-O. A simple schematic 2-dimensional model for the formation and

growth of clusters in the system was given by Wriedt and Darken[41] (Figure 2.8). At lower temperatures, 300 - 400°C, the oxygen would be moving thousands of atomic distances in the time it takes Al to move one. Thus at the $\lim_{T \to 300°C} \frac{D(Al)_{Ag}}{D(O)_{Ag}} \approx 0$ Al would not be moving at all, and the configurations given in Figure 2.8 would apply. In Figure 2.8 the intersections represent silver atoms. A small migration of aluminum during the oxidation process leads to a cluster as shown in the center, and a larger cluster. Substantially larger migration would lead to a much larger cluster and finally to corundum Al_2O_3. Classical nucleation theory cannot be used to predict the formation of these clusters, but, a bond energy approach like quasi-chemical theory might be of some use.

The clustering results obtained in internal nitriding of iron - Ti, V, Nb, Ta, Cr, Mo, W, Mn alloys should be mentioned due to their similarities to internal oxygen clustering[42,43,44]. K. H. Jack[42] has found (Fe, Mo, N) clusters in Fe - 5.0 wt % Mo alloys in the earliest stages of precipitation during internal nitriding. At intermediate temperatures 500°C - 650°C and high supersaturations, isothermal formation of substitutional-interstitial solute atom clusters, ie. zones may form. These zones, initially are coherent with the matrix, forming disc-shaped zones on {100} matrix planes. They are 6 - 12 Å thick and a composition near $Fe_{12}Mo_4N_2$. Once stable, the zones proceed to form one or more intermediate metastable phases coherent at first

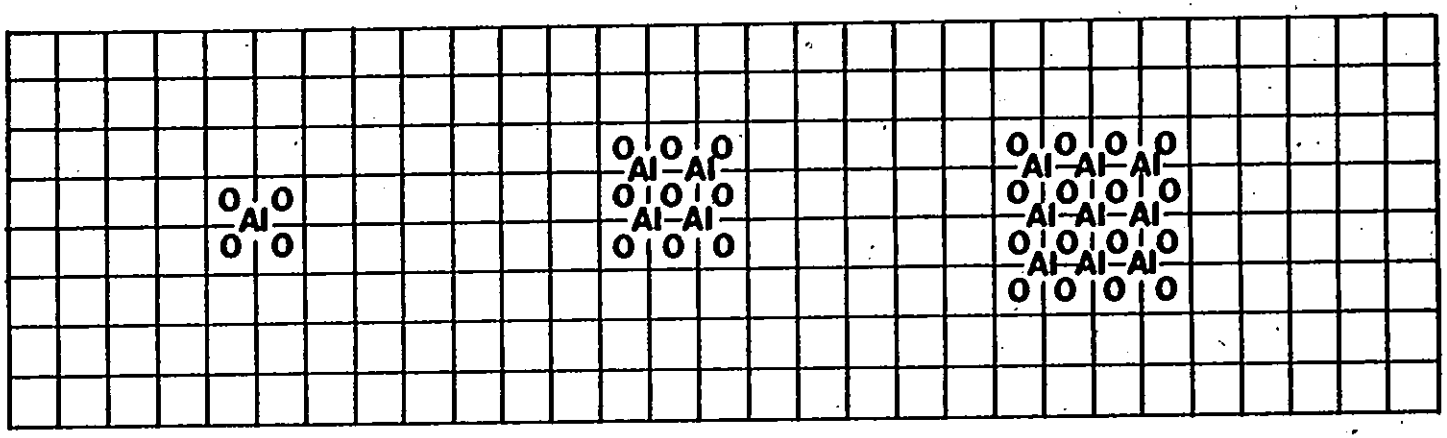

Figure 2.8 Schematic representation of aluminum-oxygen clusters on silver lattice. (Ref. 41)

and then becoming incoherent, which leads to finally the equilibrium precipitate. The precipitation goes through a sequence analagous to that recognized in the classical work on Al - 4 wt % Cu and the transmission electron micrographs give a similar "tweed" pattern[42].

Clustering during internal oxidation will be one of the most exciting topics in the near future because S.T.E.M. will provide the much needed resolution and analysis capability to study their formation and growth.

2.4.3 Number of Primary Oxide Particles Per Unit Volume

For a given volume fraction of precipitated internal oxides, the size (or number) of the precipitates and therefore the precipitate morphology will be determined principally at the reaction front, through the competition for solute atoms between the processes of growth of the existing particles and nucleation of the new precipitates. Kahlweit[45] treated the nucleation of BO_ν precipitates in internal oxidation quantitatively by the following model.

They calculated the concentration profiles and gross displacement under the assumption of finite solubility product Ksp of the BO_ν oxide. Equations (2-26) and (2-27) are valid here. Kahlweit[45] proposed the following diffusion controlled model for precipitate nucleation which is shown in Figure 2.9. The solubility product is given by (2-32):

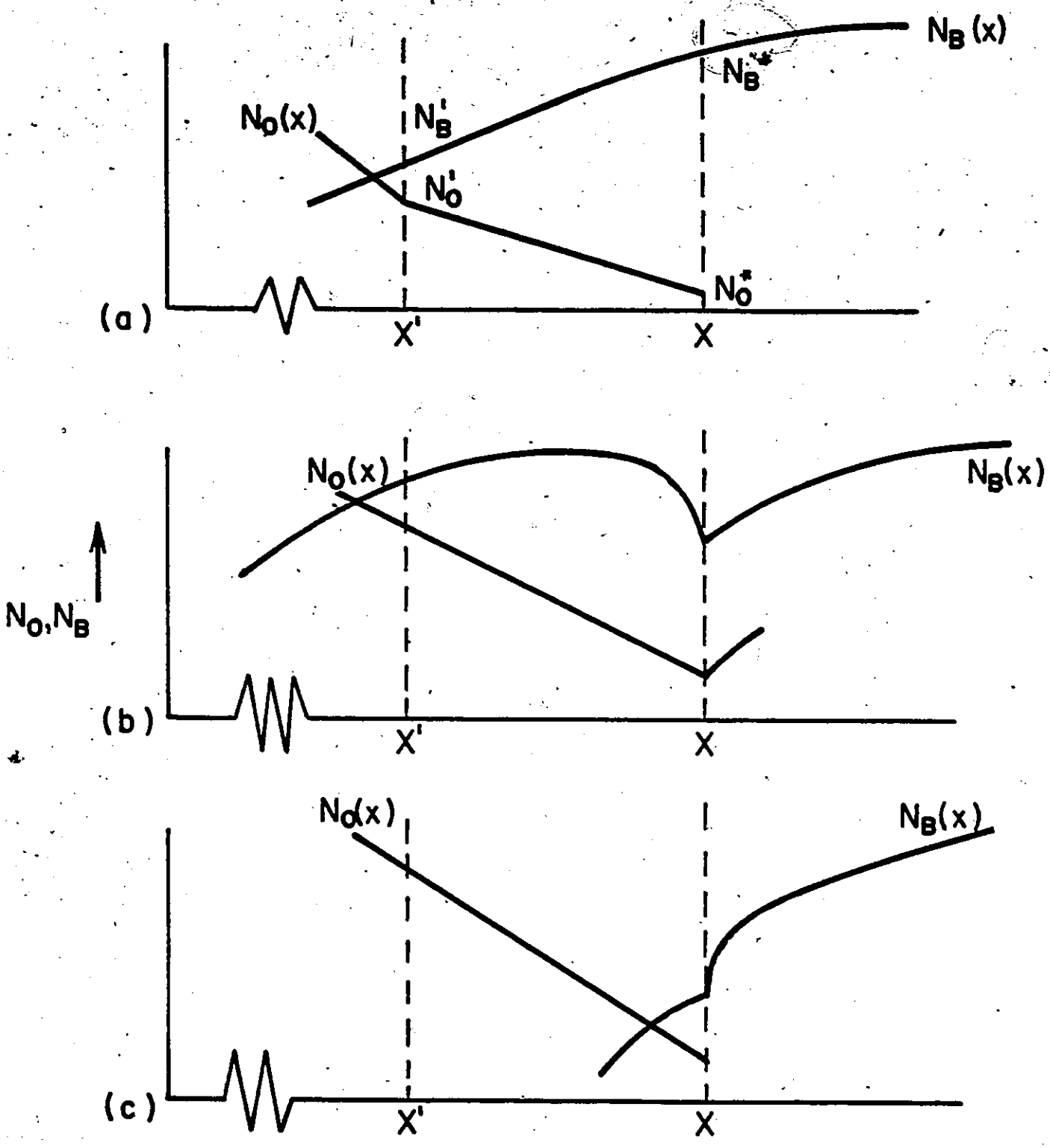

Figure 2.9 Concentration profiles in the immediate vicinity of the precipitation front (Note: $N_B^* B_O^*$ concentration product of a nucleus of critical size). (Ref. 45)

$$Ksp = (N_o')(N_B') \ .$$

Figure 2.9(a) represents the concentration profiles before the start of precipitation at position x. Figure 2.9(b) shows the profile after start of precipitation; the oxygen concentration at x would be reduced to a low value because of the relatively high B concentration. Excess B about the particle is removed after growth hence the gradient in B about the particle is removed. Thus fewer inward diffusing oxygen atoms are consumed in particle growth so that the oxygen concentration can again increase to a profile equivalent to that of Figure 2.9(a), where the cycle repeats itself[45].

Where diffusion controlled precipitate growth occurs, the average precipitate spacing is given by the distance between two successive points of nuclei formation $\Delta x = x' - x$. Thus the number of precipitates Z(x) per unit volume may be given by:

$$Z(x) \approx (\Delta x)^{-3} = \left(\frac{x}{\Delta x}\right)^3 \frac{1}{x^3} \ . \qquad (2\text{-}66)$$

Z(x) must be evaluated in terms of the unknown parameters N_o, N_B, N_o^* and N_B^* (see Appendix 1).

$$Z(x) = \frac{N_o^3}{x^3} \beta \qquad (2\text{-}67)$$

$$\beta = \frac{1}{N_o^3} \frac{x}{\Delta x} \qquad (2\text{-}68)$$

where β is a function of D_o/D_B, N_B^o, Ksp and $(N_o^*)(N_B^*)$ but

not $N_o^{(S)}$ or x. Using (2-67) the number of precipitates per unit volume of a given (N_o') depends inversely on the cube of the distance of the precipitation site from the external surface. Also, the number of precipitates per unit volume at a given x varies directly as the cube of the oxygen mole fraction at the external surface. If one knows Ksp, $(N_o^*)(N_B^*)$, D_o, D_B and $N_o^{(S)}$, the particle density can be predicted[45].

If solute enrichment is negligible (Figure 2-1(a)) then the radius of a spherical precipitate is expressed as

$$z\,\frac{4\pi r^3}{3} = V_{BO_\nu}\, N_B^{(o)} \tag{2-69}$$

$$r(x) = \left(\frac{3\, V_{BO_\nu}\, N_B^{(o)}}{4\pi\beta}\right)^{1/3} \frac{x}{(N_o^S)}\,. \tag{2-70}$$

Equation (2-69) gives the number of ppt/unit volume while (2-70) gives the radius of the precipitates[45].

Unfortunately the model has drawbacks; equation (2-70) cannot be used to calculate small or large precipitate sizes. Small sizes cannot be predicted because in many systems oxygen-solute clusters precede stable equilibrium nuclei. The model deviates at higher particle sizes because oxide needles or platelets are generally observed rather than spherical particles. Bohm[46] and Kahlweit have experimentally tested (2-67) for dilute Ag-Cd alloys

over a small range of oxygen pressures and have found general agreement. Bolsaitis[35] and Kahlweit have used the model for Cu-Si alloys, and obtained good results over a limited size range.

2.4.4 Morphological Development Leading to the Transition from Internal to External Oxidation

For simplicity, consider binary alloys where only the solute forms an (stoichiometric) internal or external oxide and the solvent does not (e.g. silver base alloys at temperatures greater than 500°C). Let A be the solvent and B the solute in the ternary A-B-O system.

The transition from internal to exclusive external oxidation should occur when the solute B is sufficient to form a critical volume of BO_ν at the internal oxidation front. Once formed the oxides act as local barriers for oxygen and solute atom movement because diffusion of these species can only occur in the channels between those particles which are previously precipitated. Thus, further reaction at the internal oxidation zone may occur by ripening of particles BO_ν (requires low supersaturation), or by the nucleation of new BO_ν particles (higher supersaturation required). If ripening or sidewise growth of the particles BO_ν were maintained (without nucleation), the particles would grow together forming a compact BO_ν layer, preventing further internal oxidation. Hence the critical B content

would be that necessary to maintain the sidewise growth of BO_ν, without continued nucleation. If this sidewise growth occurs at the very start of oxidation, a protective layer is formed at the surface. The critical solute content is given by equation (2-37) [47].

CHAPTER III

EXPERIMENTAL PROCEDURE

3.1 Introduction

This chapter is devoted to specimen preparation and chemical analysis, the oxidation apparatus and procedure, analysis of internal and external oxides by optical microscopy, scanning electron microscopy, X-ray energy dispersive analysis, electron microprobe analysis and X-ray diffraction.

3.2 Sample Preparation and Chemical Analysis

3.2.1 Specimen Preparation

Ag (99.999% purity) and Zn (99.999% purity) used in this study were purchased from Alpha Division Venturon Corporation. Portions of each metal were weighed to yield alloys with nominal compositions of .1, 2, 8, 11, 15, and 20% wt.% Zn. The phase diagram for the Ag-Zn system is given in Figure 3.1. Useful thermodynamic parameters for the Ag-Zn system are given in Appendix 2. The alloys were prepared by melting the pure metals of desired proportion in an argon atmosphere by means of induction heating. They were vertically cast into a cylindrical graphite mold and cooled to room temperature in the argon atmosphere. The

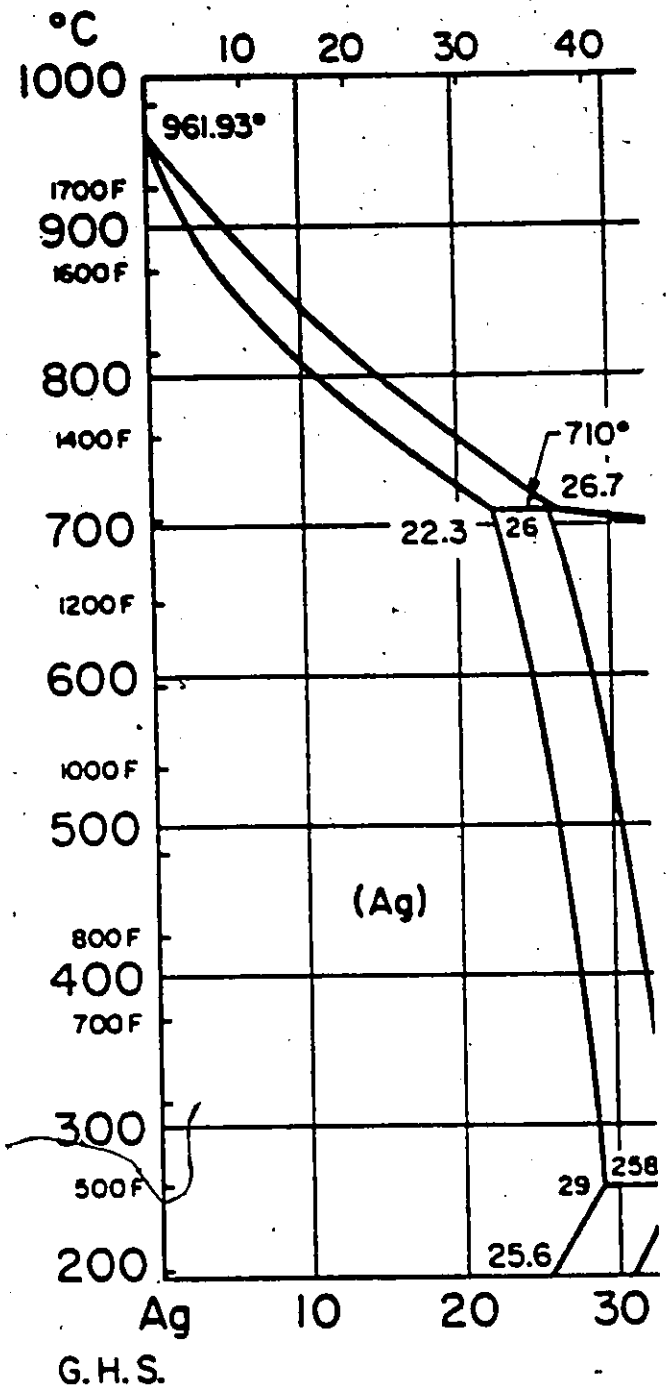

Figure 3.1 Ag-Zn phase diagram. (Ref. 48)

ingots were then placed in quartz tubing, filled with zero-oxygen-grade (< 0.5 ppm) argon to a pressure of 10 mm Hg and sealed. The alloys were then homogenized at 550°C for 7 days and subsequently machined to the dimensions of .9 cm in diameter and 4 cm long. Once machined, the ingots were cold rolled into sheets to a thickness of 1.5 mm. Rolling served to heal casting defects and bubbles formed from zinc boil.

Test specimens were produced by cutting the sheets into rectangular platelets of approximate dimensions 1.5 cm×1 cm×1.5 cm. A suspension hole 0.6 mm in diameter was drilled through each sample. The specimens were then ground on all sides from 220 to 600 grit SiC paper using water as a lubricant. Following this step, the samples were stress relieved at 550°C for 90 minutes in zero-oxygen grade argon flowing at 1 cc per minute in a mullite tube furnace. The grain size varied from 0.007 to 0.011 cm which corresponds to ASTM standard grain size No. 5 to No. 4 respectively.

Prior to oxidation the specimens were electro-etched[47,49] in 1N HNO_3 at a current density of 40-60 mA/cm^2 until a clean shiny surface was produced (Figure 3.2). For alloys of compositions greater than 11 wt. % Zn a non-oxidized surface was not possible to produce. For alloys greater than 11 wt % Zn electroetching was carried out for 30 seconds according to Rapp[47] and Pickering[49], pro-

Figure 3.2 a) Electroetched surface, grain size 0.01 mm 1.84 % Zn

b) S.E.M. electroetched surface, height of largest step 2 u, 1.84 % Zn

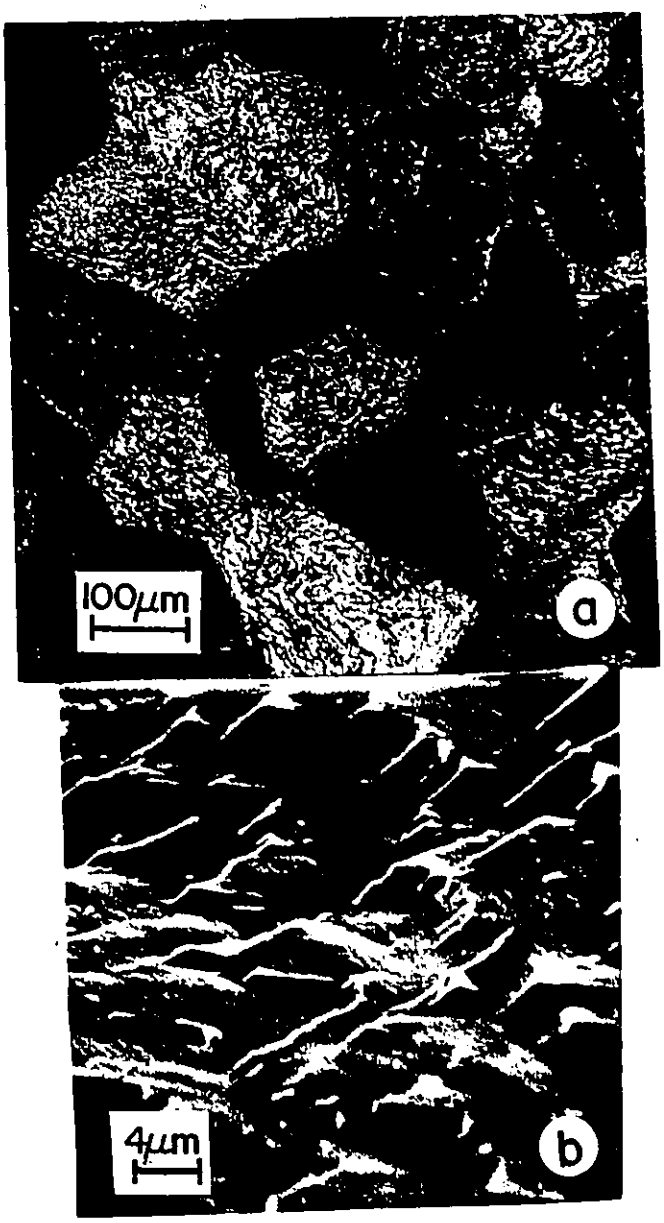
100μm
a
4μm
b

viding the smoothest surface with the least retained oxide film on the surface. Conventional metallographic polishing techniques lead to surface damage, pitting and embedding of diamond paste in these alloys.

3.2.2 Determination of Alloy Composition and Homogeneity

Representative samples from each of the alloy sheets were chemically analyzed for silver by the silver chloride (gravimetric) method[50]. The alloy compositions are given in Table 3-1.

Table 3-1

Alloy Compositions

Nominal Compositions	Actual Composition	
	wt % Zn	at % Zn
Ag - .1	0.02±0.005(2)	0.03
Ag - 2	1.8 ±0.02 (2)	2.9
Ag - 8	7.5 ±0.07 (3)	11.8
Ag - 11	10.9 ±0.09 (2)	16.8
Ag - 15	12.9 ±0.10 (3)	19.6
Ag - 20	18.7 ±0.40 (3)	27.5

Alloy homogeneity was insured by scanning across that specimen, from the center and exterior of each ingot, using electron microprobe analysis .

3.3 Oxidation Apparatus and Procedure

3.3.1 Oxidation Apparatus

The apparatus used for the oxidation of the alloys is given in Figure 3.3. Oxidation tests were performed in flowing oxygen (1 cc per minute) at 1 atm pressure. The oxidation temperature was 550°C. The pure oxygen was supplied by Matheson, and purified further by passage through ascarite, silica gel and drierite to remove any CO_2 and H_2O present. Before introducing oxygen into the furnace, pure zero-oxygen grade argon was used for flushing. The argon was also purified for O_2, CO_2 and H_2O by passage through Cu/Cu_2O chips at 300°C, silica gel and drierite respectively.

Samples were hung on a quartz rod by means of a Pt wire, the quartz rod was used to introduce the samples into the hot zone of the furnace. Leakage of oxygen during the introduction of the quartz rod and during the oxidation run was prevented by passage through a swagelock fitting containing two sealing O-rings. The reaction tube was a cylindrical mullite tube, 1 5/8" O.D. and 30" long to which were fastened pyrex glass connections. The reaction tube was heated by a heavy-duty Lindeburg furnace, and the temperature was controlled by a proportional controller to within ± 2°C. The temperature profile of the reaction tube was determined by a chromel-alumel thermocouple. The flow of argon and oxygen were controlled by calibrated flowmeters.

Figure 3.3 Oxidation Apparatus

1 Oxygen purifier containing ascarite, silica gel and drierite 2 Argon purifier containing Cu/Cu_2O chips, silica gel and drierite 3 oxygen flowmeter 4 Argon flowmeter 5 mixing chamber 6 reaction tube 7 furnace 8 hot zone of furnace 9 controller 10 quartz rod 11 swage lock containing two sealing O-rings 12 quartz rod and sample 13 valve 14 oil bubbler.

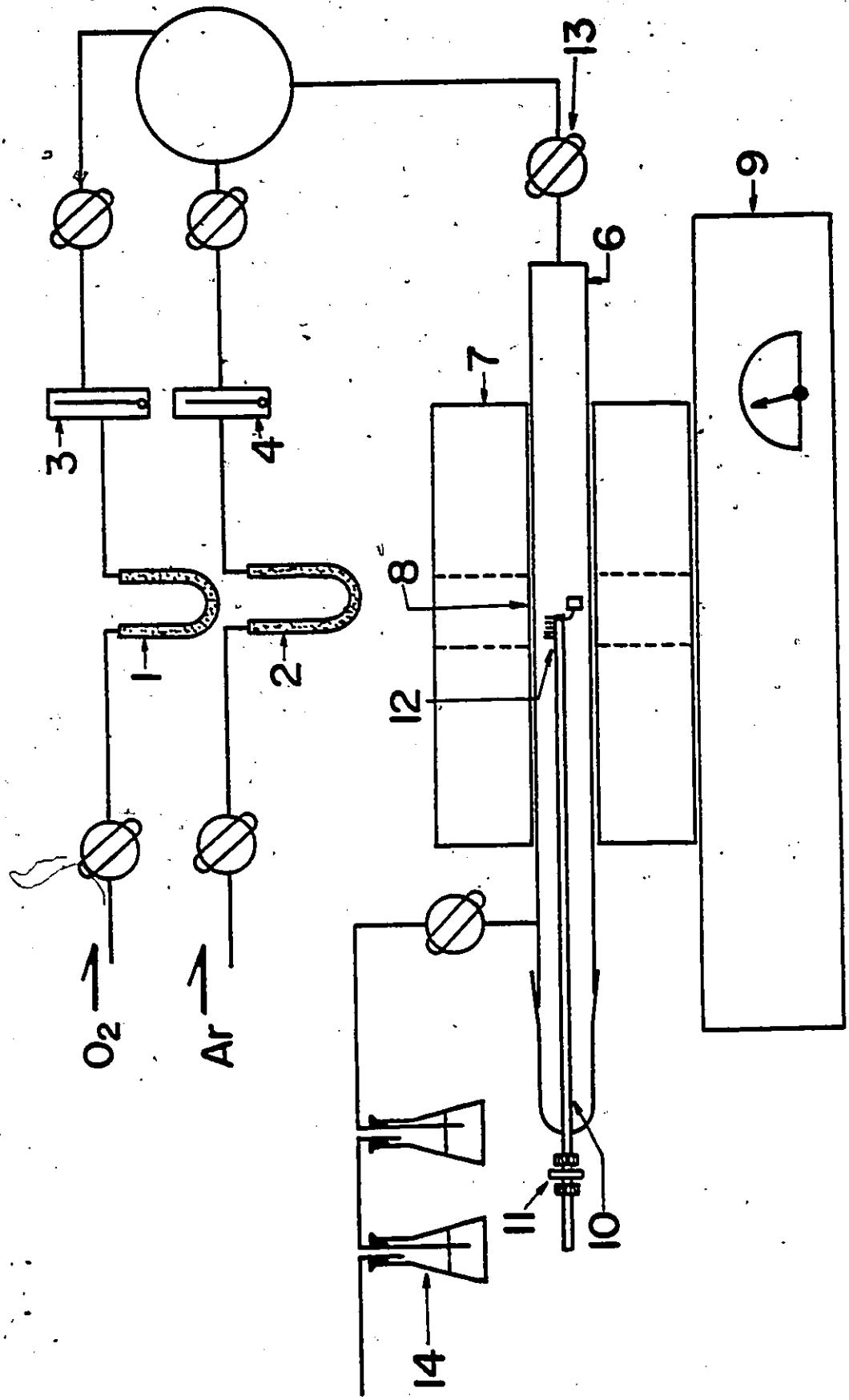
13
9
6
7
3
4
8
1
2
12
O_2
Ar
11
10
14

3.3.2 Oxidation Procedure

After electroetching, the samples were attached to the quartz rod and placed in the cold end of the reaction tube. The system was then flushed for 30 minutes with argon and finally oxygen was introduced. After 30 minutes the samples were moved into the hot zone for the desired length of time. Upon completion of the run, the sample was removed from the hot zone, cooled to room temperature, and stored under vacuum in a desiccator.

3.4 Techniques Used for Analysis of Oxidation Products

3.4.1 Optical Metallography

Oxidized specimens were vertically (for cross-section observation) and some horizontally (for transverse section observation) mounted in room-setting epoxy resin. The specimens were then metallographically prepared to a finish of 1 micron. In order to distinguish the internal oxide phase, a chemical polish and chemical etchants were used to remove the oxide from the matrix.

The chemical polish consisted of 7 grams of CrO_3 in 100 ml of distilled water mixed with 5 ml of 5% HCl solution. The surface of the samples were scrubbed with a cotton ball soaked in the solution for a few minutes. Upon completion, any Cr_2O_3 formed was removed by further scrubbing with a cotton ball soaked in orthophosphoric acid until a clean shiny surface appeared. After this step the samples were etched in a 0.5 N NH_4OH for 30 minutes.

Optical examination and photography were carried out using a Zeiss optical microscope. The rates of growth of the internal oxide phase were determined by measuring the depth of the zone. The results obtained were obtained using a calibrated filar eyepiece with a Reichert metallograph. The internal oxidation zone/matrix interface was poorly defined in the 1.8 wt % Zn alloy, and thus the results to be reported are averages for a large number of observations.

3.4.2 Scanning Electron Microscopy and Energy Dispersive X-ray Analysis

A Cambridge scanning electron microscope was used to study the morphology of internal and external oxides. The epoxy mounted samples were coated with C by vapour deposition to prevent electrical charge build-up while examining the samples in the SEM and EPMA. The samples containing an external scale (12.9 wt %, 18.7 wt % Zn) were covered with vapour deposited Cr because it provided better protection against charge build-up. The topography of the oxidized surface of all alloys was studied by using SEM.

An X-ray energy dispersive analyzer attached to the SEM permitted identification of the elements and their distribution within the internal and external oxide zones. The results obtained by this technique are only qualitative in nature.

3.4.3 Electron Probe Microanalysis

A Cameca MS-64 electron microprobe was used to determine the Ag and Zn proviles in 7.5 wt % and 10.9 wt % Zn alloys. The profile of Ag-Zn at the alloy/internal oxidation zone interface was determined by scanning across the internal oxidation zone perpendicular and parallel to the external surface. The profiles of the two alloys give an indication of Zn depletion at the alloy/internal oxidation zone front. And also, inside the internal oxidation zone.

3.4.4 X-Ray Diffraction

The identification of the external oxide was carried out by the Debye-Scherrer[51] powder method. The oxide on the oxidized surface of the Ag - 18.7 wt % Zn was removed mechanically and ground in a mortar to produce a fine powder. The oxide powder was then coated on a fine glass fibre using petroleum jelly and irradiated with Cu-K_α radiation.

CHAPTER 4

EXPERIMENTAL RESULTS

4.1 Introduction

The results obtained from the different alloys are divided into three major sections, according to the oxidation products produced. The oxidation classifications are internal oxidation, internal oxidation in combination with external oxidation, and exclusive external oxidation. In each section the results will be presented in the usual form of graphs, tables and photomicrographs.

4.2 Internal Precipitation of ZnO in Ag 1.8, 7.5 and 10.9 Weight Percent Zn Alloys

4.2.1 Internal Oxidation Kinetics

The kinetic curve for the growth of internal ZnO in Ag-1.8 wt % Zn alloy is given in Figure 4.1. The curve was obtained by measuring the penetration of internal oxidation zone in a given length of time. The internal oxidation front was not uniform but rather banded (Figure 4.4). The two groups were composed of internal oxides growing at a faster and slower rate (thus the two solid lines). A least square analysis was used to fit the points to the best straight line. Appendix 3 contains additional statistical results for this curve and others. The dashed line represents the best fit over all points. The individual points are presented without error bars because the spread of the points is much greater than individual error bars.

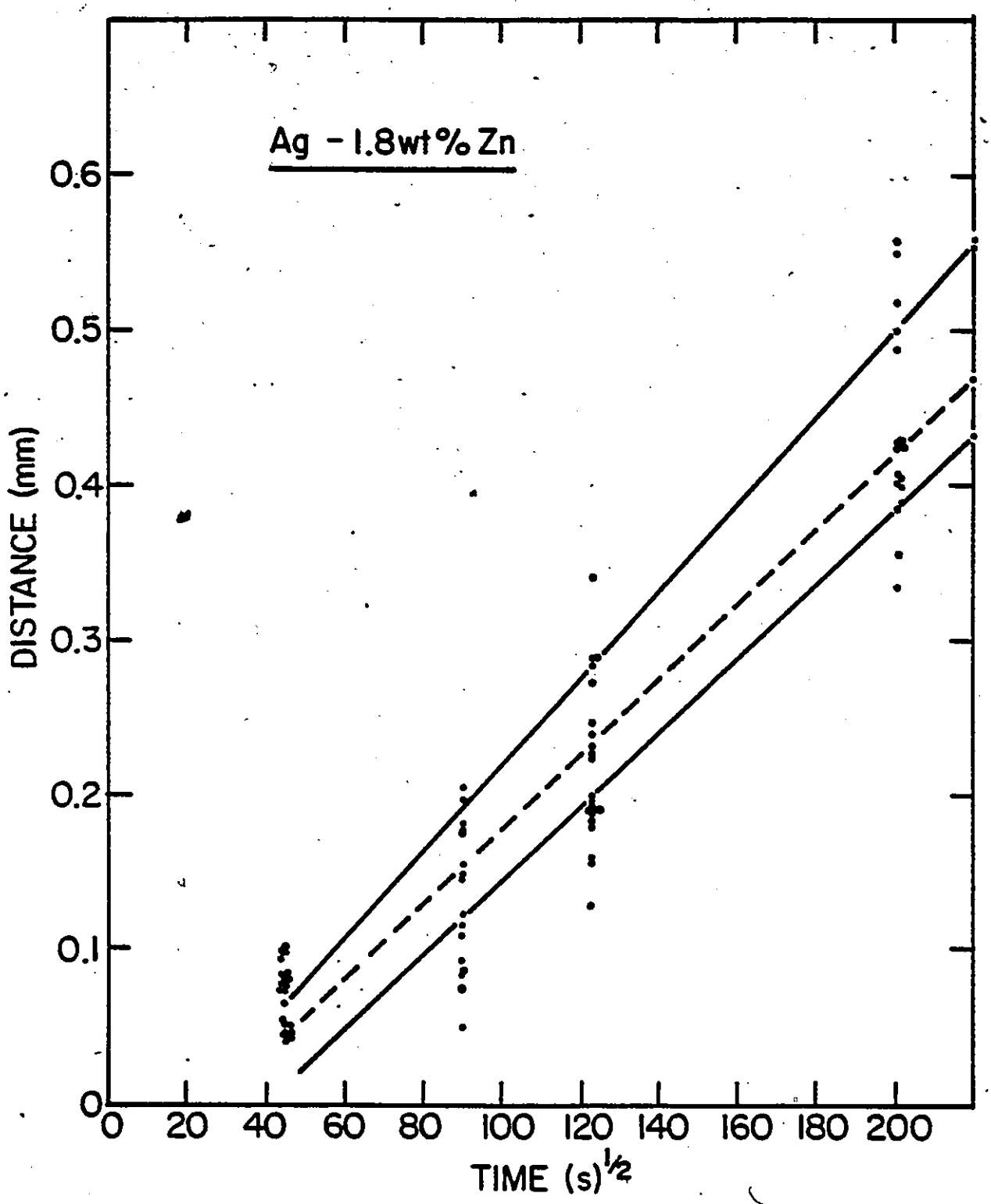

Figure 4.1 x vs $(t)^{1/2}$, Ag-1.8 wt % Zn

Figure 4.2 gives the kinetic curve for the Ag-7.5 wt % Zn alloy. The internal oxidation front was more uniform (Figure 4.7(a), (b)) and the points were also fitted to a straight line by least squares method.

Finally, Figure 4.3 contains the kinetic results for the Ag-10.9 wt % Zn alloy. The internal oxidation front was found to be uniform once again (Figure 4.10(a)). From the three curves it can be concluded that the internal oxidation zone thickened according to the parabolic rate law. As one increases the zinc in the silver the penetration of the internal oxides decreases significantly. The parabolic rate constants are given in Table 4-1. The kinetic results obtained here are in agreement with those obtained by

Table 4-1

Parabolic Rate Constants for 1.8, 7.5 and 10.9 wt % Zn

Alloy	K mm/(sec)$^{1/2}$
1.8	2.73×10^{-3}, 2.48×10^{-3}, 2.41×10^{-3}
7.5	6.61×10^{-4}
10.9	4.23×10^{-4}

Pickering[49] for 5, 9, 15 and 21 atomic percent alloys under the same oxidizing conditions.

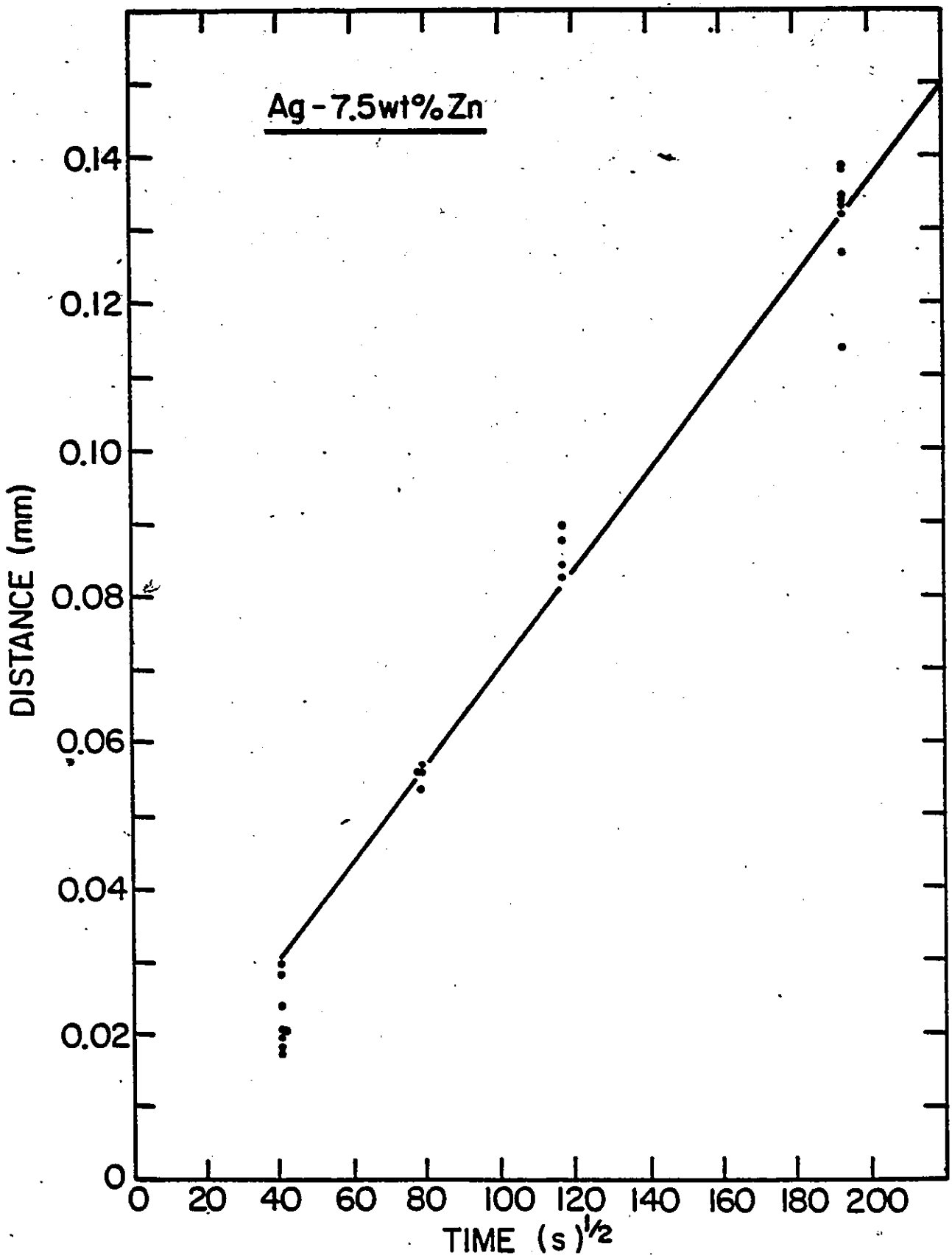

Figure 4.2 x vs $(t)^{1/2}$, Ag-7.5 wt % Zn

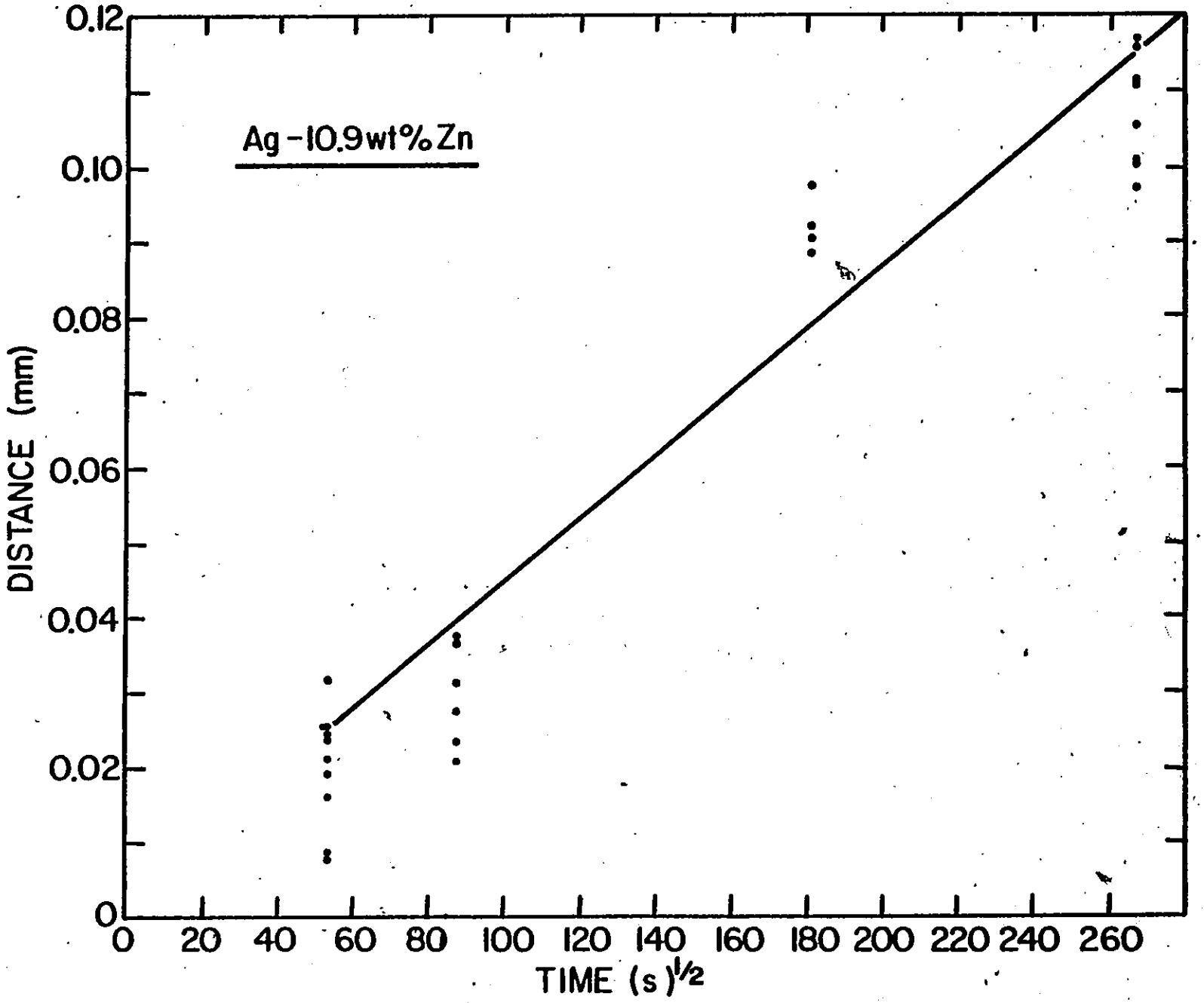

Figure 4.3 x vs $(t)^{1/2}$. Ag-10.9 wt % Zn

4.2.2 Morphology and Structure of Internal Oxides

4.2.2.i) Ag-1.8 Weight Percent Zn Alloy

Figures 4.4 are optical photomicrographs taken in cross sections of the alloy. Contrast of the internal oxides is achieved by removal of the oxides, as mentioned previously. From the micrographs it is evident that growth occurs on certain crystallographic planes (Figure 4.4(a)). The oxides grow in colonies inward from the surface, either perpendicular, horizontal or at some inclination to the surface. The horizontal growth with respect to the surface will be referred to as a growth of lateral plates (Figure 4.4(b)). It has been found to occur in Cu[52] alloys containing Al, Zn and Si. Figure 4.4(c) shows that some colonies can grow through others or be stopped. The oxide families grow in certain specific directions in a single grain. Upon meeting a grain boundary, they are stopped. Growth in the new grain will occur on the same crystallographic planes, but its direction relative to the surface may change (Figure 4.4). Figure 4-5(a) SEM photomicrograph shows one colony being stopped by a grain boundary, while Figure 4.5(b) shows the intersection of the two colonies at a grain boundary.

From the optical and SEM photographs of cross-sections a platelet or rod nature cannot be determined for the oxides. To overcome this problem a transverse section was examined. Figure 4.6 gives optical and SEM micrographs of this section.

Figure 4.4

Optical Micrographs of Ag-1.8 wt % Zn in cross-section

(a) Sample showing crystallographic dependence of internal oxides, oxidation time 4 hr, 72×

(b) Note lateral growth, oxidation time 2 hr, 200×

(c) Change of growth direction, intersections, oxidation time 4 hr, 288×

(d) The non-uniformity of internal oxidation front, oxidation time 4 hr, 176×

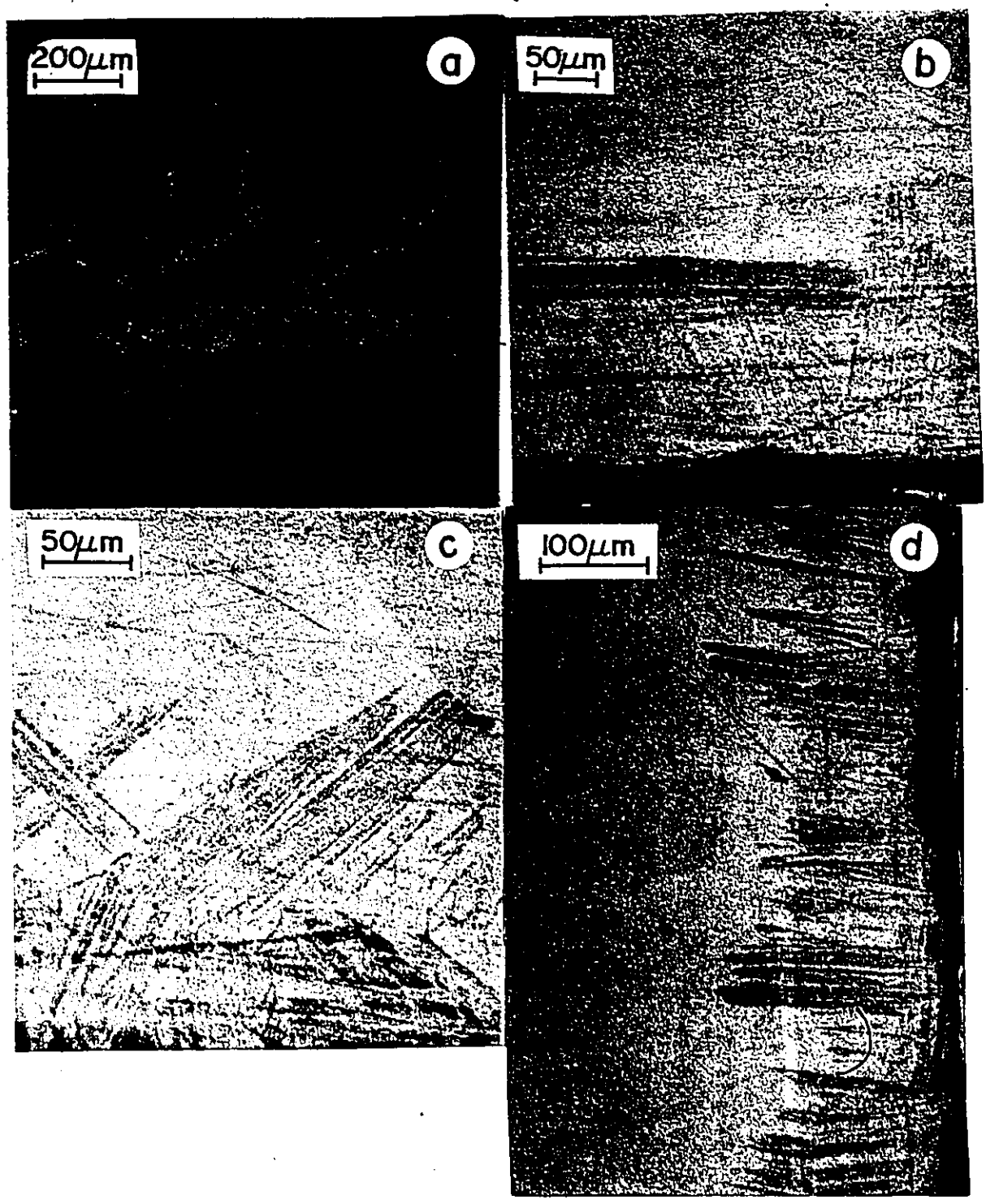
200μm
a
50μm
b
50μm
c
100μm
d

Figure 4.5

SEM micrographs of Ag-1.8 wt % Zn in cross-section

(a) Colony stopping at grain boundary and a new colony growing in a different direction, oxidation time 0.5 hr, 2K

(b) Colony growing perpendicular to surface on certain planes, oxidation time 10 hr, 560×

(c) Close-up of (b), 3.25K

(d) Intersection of two colonies, one horizontal the other perpendicular to the surface, oxidation time 10 hr, 560×

(e) Close-up of (d), 5.6K

(f) Close-up of (e), 11.2K

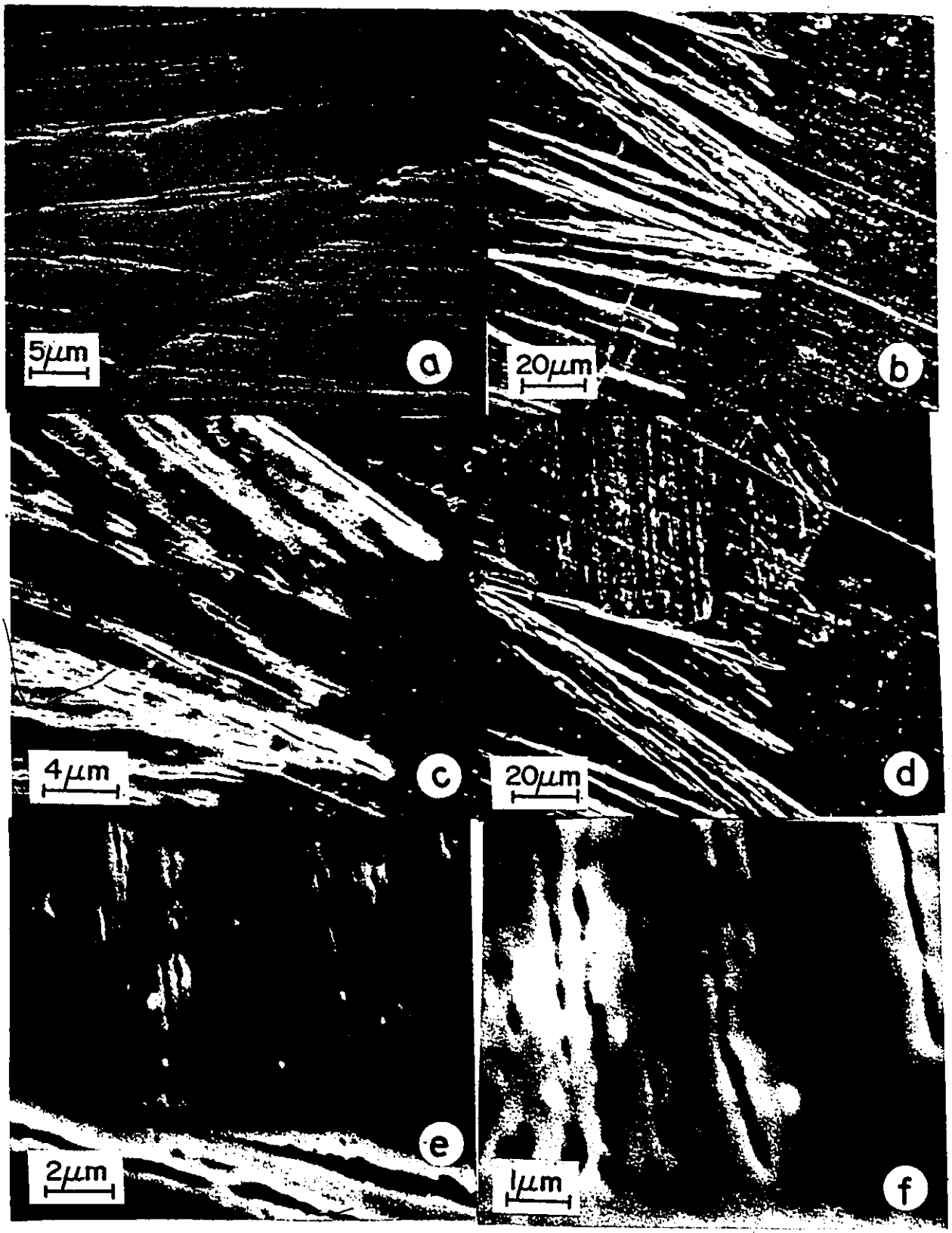
5μm
a
20μm
b
4μm
c
20μm
d
2μm
e
1μm
f

Figure 4.6

Transverse section of Ag-1.8 wt % Zn

(a) Optical micrograph, showing growth of ZnO platelet colonies, oxidation time 14 hr, 64×

(b) Colony of internal ZnO platelets inside one grain, 256×

(c) SEM micrograph of an oxide colony at the edge of a grain, depth 0.09 mm under surface. Oxidation time 14 hr, 1.53K

(d) SEM micrograph, close up of a colony, 3.825K

(e) SEM micrograph, platelets 0.22 mm below the surface, 5.4K

(f) SEM micrograph, platelets 0.344 mm below the surface, 10K

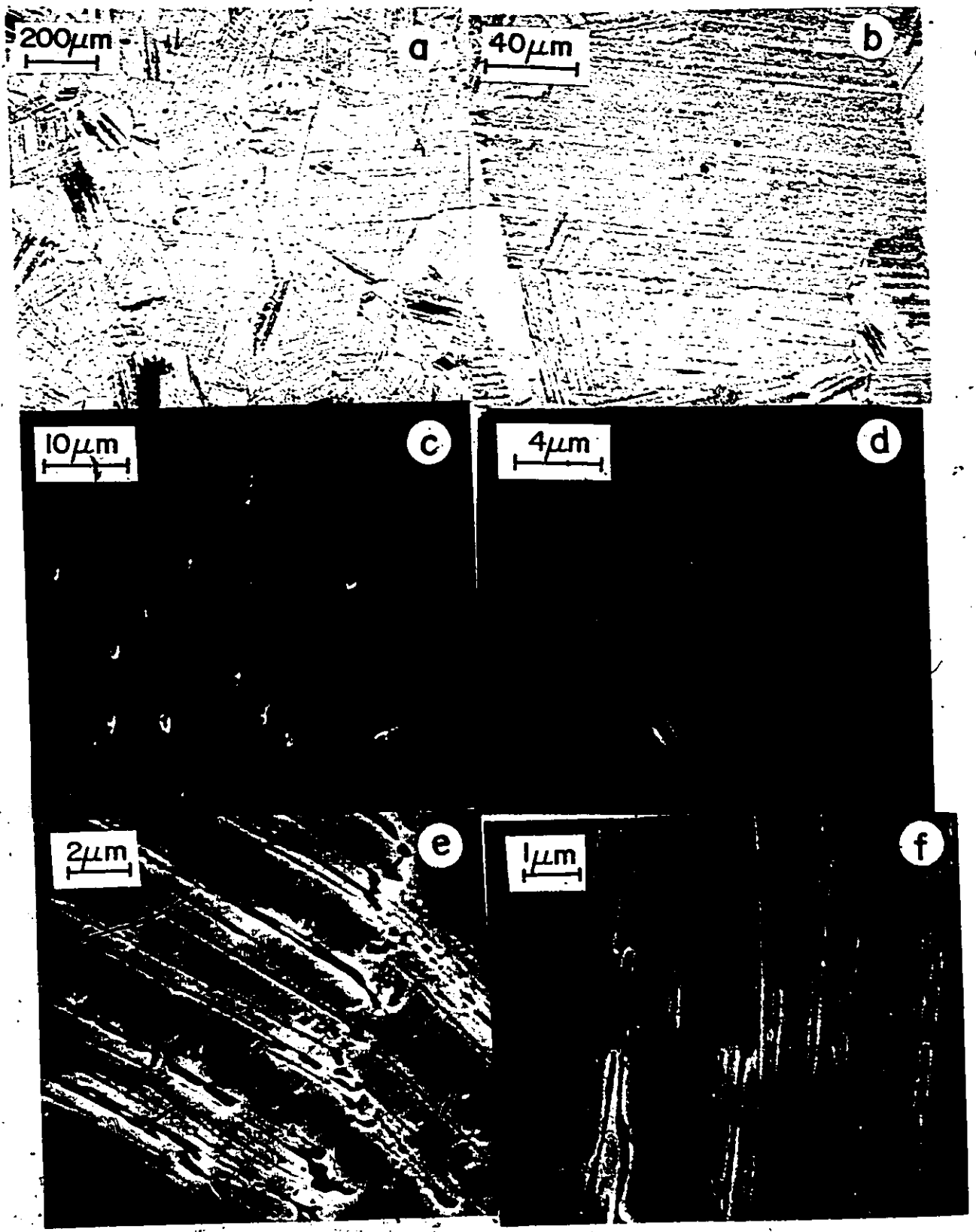
200μm
a
40μm
b
10μm
c
4μm
d
2μm
e
1μm
f

Thus the oxides are definitely platelet in nature and grow in colonies in 1 or 2 specific orientations within a given grain.

The distance between the internal oxides and their thickness in the transverse sample were determined as a function of depth. And thus by the use of Figure 4.1 as a function of time. It was hoped from these results a simple model could be put forth. As one can see from Table 4-2 the spacing decreased with increasing time while the thickness measurements decreased. The error due to measurement of the spacing the thickness of oxide platelets is approximately 20 percent.

Table 4-2

Oxide Spacing, Thickness in Ag-1.8 wt % Zn Versus Depth and Time

Depth mm	Time sec	Spacing mm	Thickness mm
0.09	4[illegible]6	2.2×10^{-3}	5×10^{-4}
0.22	10,000	4.7×10^{-4}	3×10^{-5}
0.34	27,555	4.5×10^{-4}	5×10^{-5}

4.2.2. ii) Ag-7.5 Weight Percent Zn Alloy

Figure 4.7(a),(b) contains two optical micrographs of the internal oxidation zone. The zone penetration into the alloy has decreased and is more uniform, while thickening of the oxide layer has occurred. Again two types of colony

Figure 4.7

Morphology and Structure of Internal oxides in Ag-7.5 wt % Zn

(a) Optical cross-section of internal oxides, smaller penetration, more uniform, oxidation time 4 hr, 160×

(b) Optical cross-section, lateral and arrowhead growth, oxidation time 4 hr, 240x

(c) SEM, intersection arrowhead and lateral, oxidation time 2 hr, 10.5K

(d) SEM, internal oxide colony, oxidation time 4 hr, 2.25K

(e) Close-up of the colony in (d) at the edge, 10.5K

(f) Close-up of (c), showing the edge of platelet, 21K

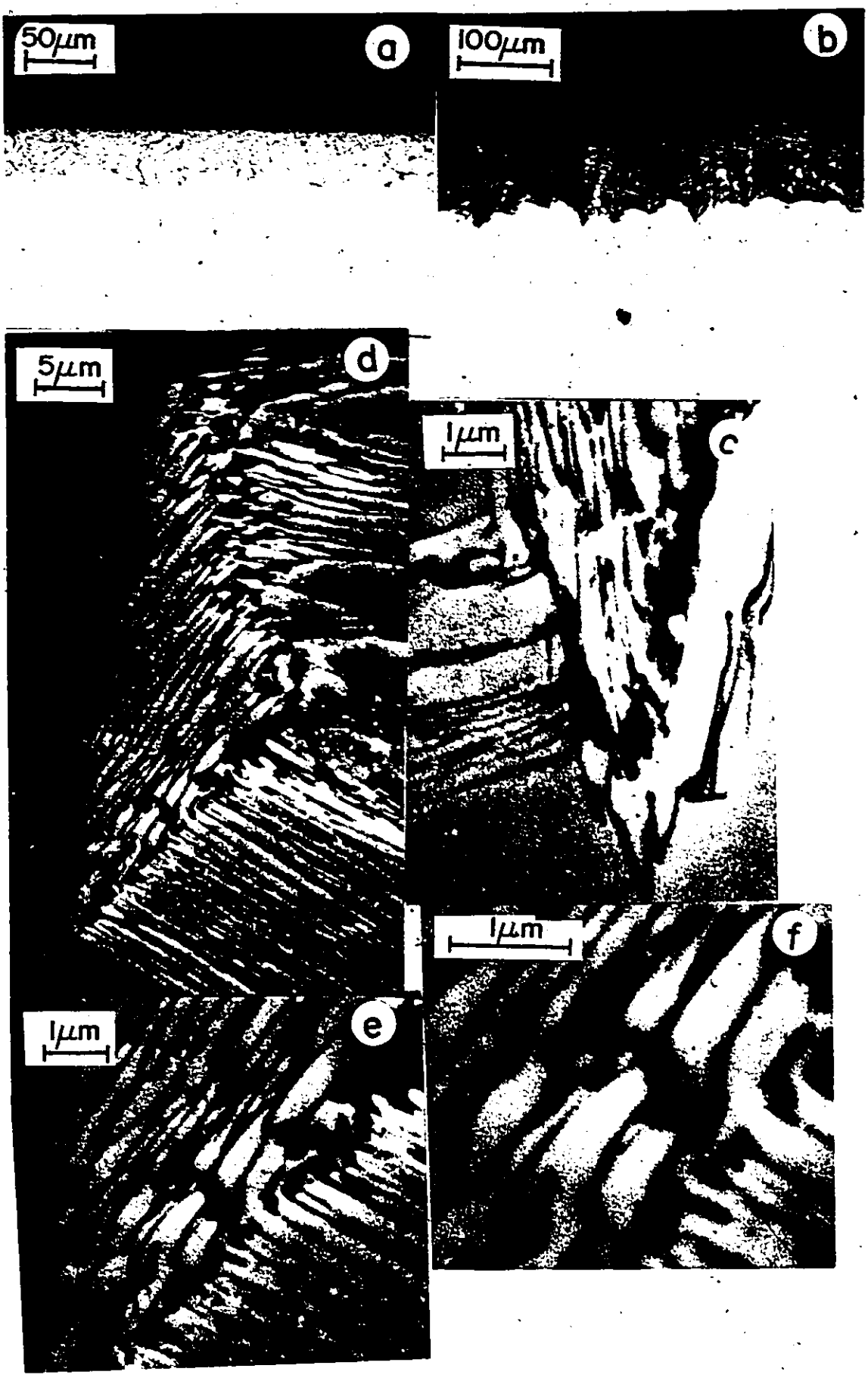
50μm
a
100μm
b
5μm
d
1μm
c
1μm
e
1μm
f

growth are exhibited, one growing perpendicular to the surface with a sharp needle-like appearance, which will be referred to as "arrow-head". The second growing parallel (lateral growth of plates) to the surface in colonies.

Figure 4.7 (c),(d),(e) contain SEM micrographs of the internal oxidation zone in cross-section. The spacing between the oxides has decreased significantly as expected due to the increase in supersaturation (zinc content). From the photographs it is not possible to tell whether the internal oxides are rods or platelets or a combination of both. The two types of growth are shown much clearer than under optical conditions. The lateral colonies are stopped at arrow-head colonies. The lateral families grow at a much slower rate than the arrow-head families. The lateral families seem to slow the arrow-head families down by impinging on them at the intersection (Figure 4.8). The crystallographic dependence of the internal oxide growth is becoming less significant in this alloy.

To determine the exact nature of the oxides a transverse section was made. Figure 4.9 gives these results at a depth of 0.06 mm below the surface. From the optical micrographs one can see the oxide density has greatly increased, some crystallographic dependence is still exhibited, the cross-hatching of colonies. The SEM pictures show quite a difference in the morphology of the internal oxides here. The morphological change is occurring along the platelets.

Figure 4.8

SEM of the Internal Oxidation Front

(a) General view, oxidation time 4 hr, 525×

(b) Lateral and arrowhead growth, 4 hr, 1050×

(c) Arrowhead growth, 4 hr, 2.5K

(d) Arrowhead and lateral intersection, 4 hr, 5.25K

(e) Lateral growth, 4 hr, 10.75K

f) Intersection, 4 hr, 21K

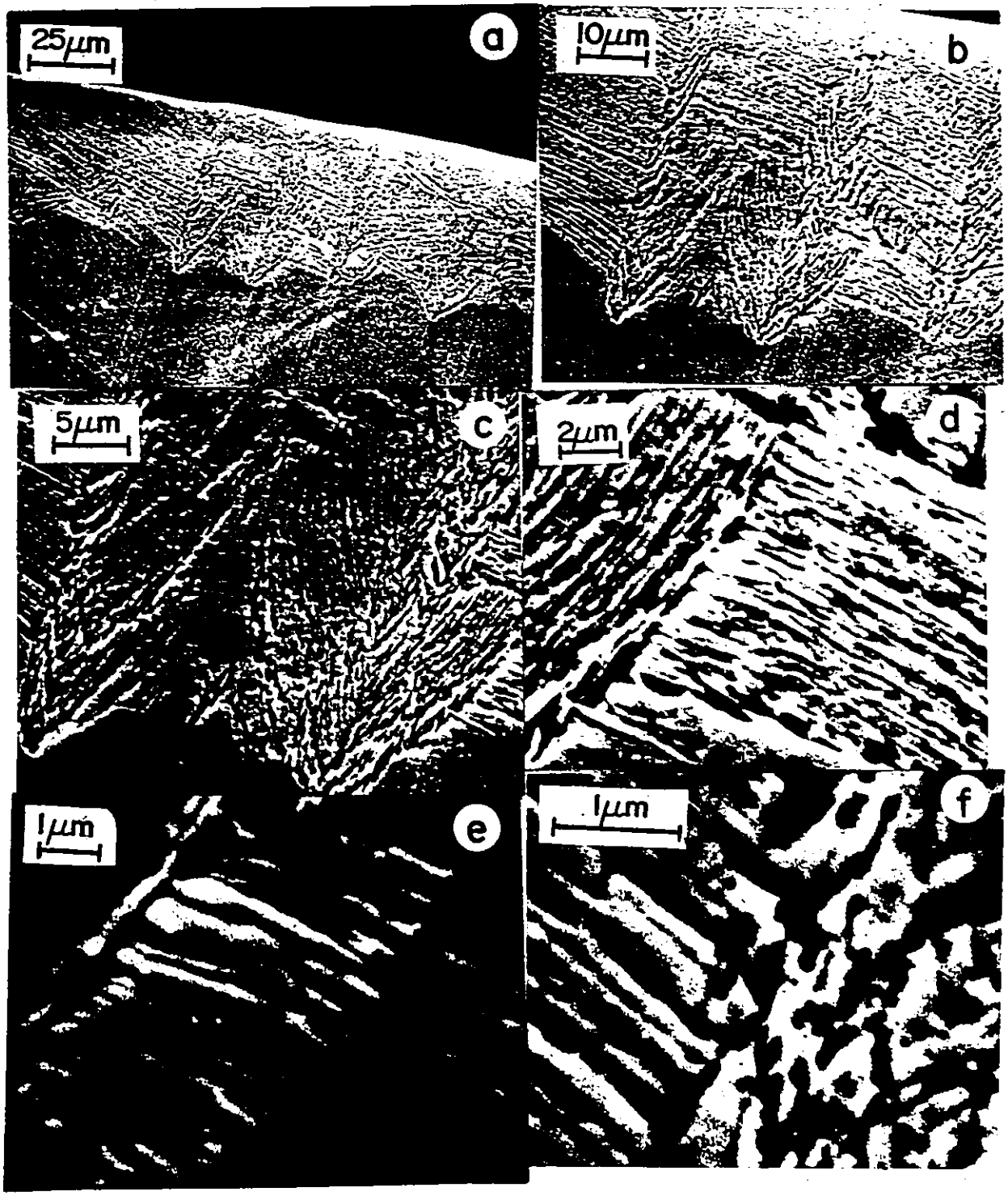
25μm
a
10μm
b
5μm
c
2μm
d
1μm
e
1μm
f

Figure 4.9

Transverse section of Ag-7.5 wt % Zn

(a) Optical micrograph, note thickening, oxide at grain boundary, oxidation time 58 hrs, 80×

(b) Optical micrograph, note crystallographic dependence, cross-hatching of oxides, 350×

(c) SEM, platelet-rod transition, dendritic structure, 3.87K

(d) SEM, rods, 7.92K

(e) SEM, platelet thickening becoming incoherent - general precipitation, 3.87K

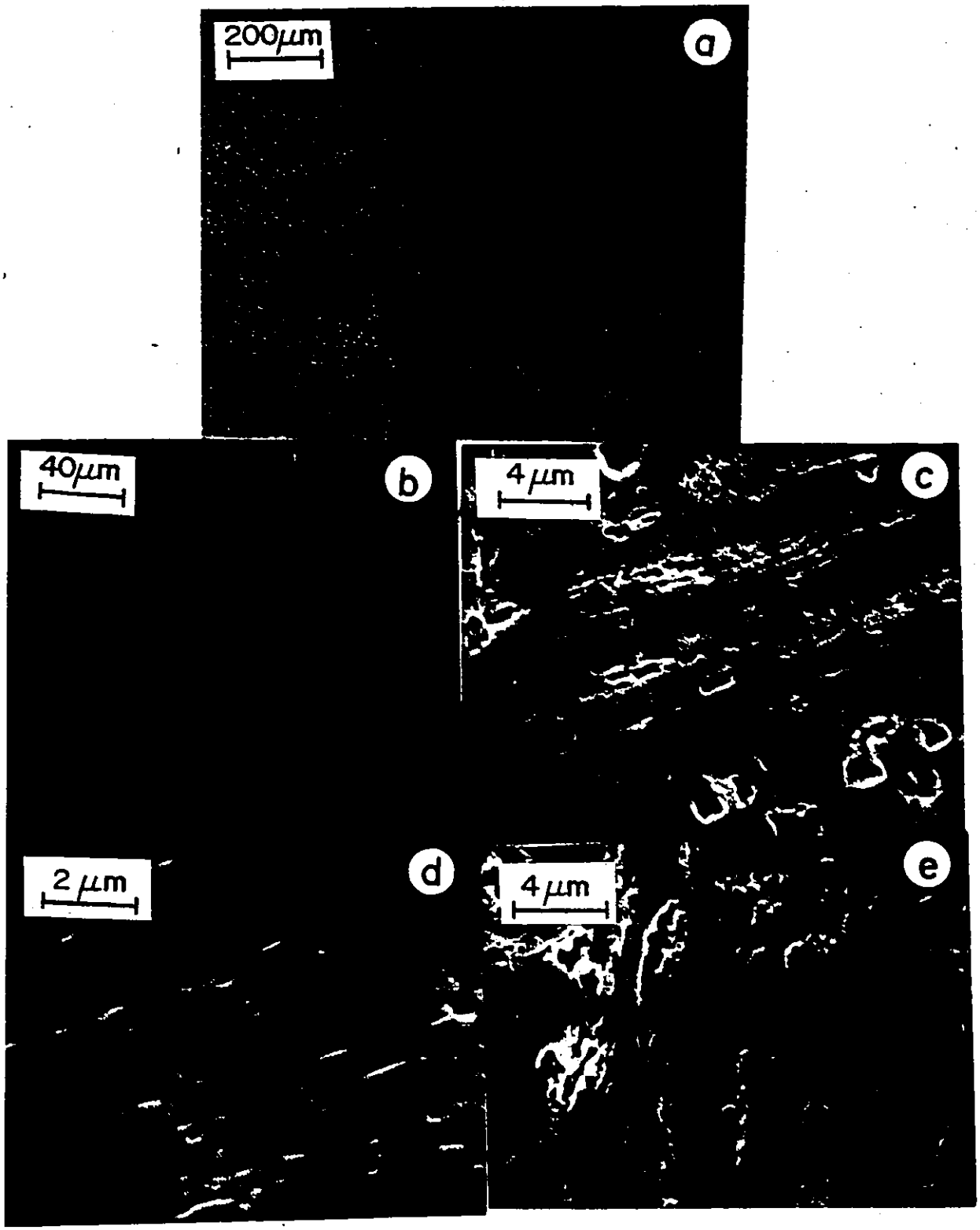
200μm
a
40μm
b
4 μm
c
2 μm
d
4 μm
e

They are transforming into rods, general type of precipitation and what looks like some sort of dendritic morphology. The oxide thickness has definitely increased resulting in a decrease in spacing between the oxide platelets.

4.2.2 iii) Ag-10.9 Weight Percent Zn Alloy

Figure 4.10 (a),(b) show optical micrographs of the internal oxidation zone and oxides respectively. The internal oxidation zone and internal oxides for this alloy do not look much different than those of Ag-7.5 wt % Zn. Again two types of growth are exhibited: arrow-head (clearly) and lateral (not so clear). The penetration of the internal oxide is slower as one can see from Figure 4.3.

Figure 4.10 (c),(d),(e) shows SEM photomicrographs of the arrow-head colonies, while Figure 4.10(f) shows lateral and arrow-head. Figure 4.11 (a) is a composite SEM photograph and (b), (c), (d), (e) are close-ups of the internal oxidation front. The photograph shows that lateral growth is dominating and the internal oxidation front is now becoming less sharp. The intersection of the lateral colonies and arrow-head come together, with one turning into the other. This effect could again slow down the growth of the arrow-head colonies.

Transverse sections were again made up to determine the internal oxide structure, spacing and thickness. Figure 4.12 shows micrographs of the transverse sections at a depth

Figure 4.10

Internal oxidation zone Ag-10.9 wt % Zn

(a) Optical photograph, internal oxidation scale, oxidation time 4 hr, 160×

(b) Optical photograph, internal oxides, arrowhead, oxidation time 10 hr, 1K

(c) SEM - arrowhead colonies, 4 hr, 665×

(d) SEM - arrowhead colonies, 1.33K

(e) SEM - between arrowhead colonies, 3.36K

(f) Lateral and arrowhead colonies, oxidation time 10 hr, 1.4K

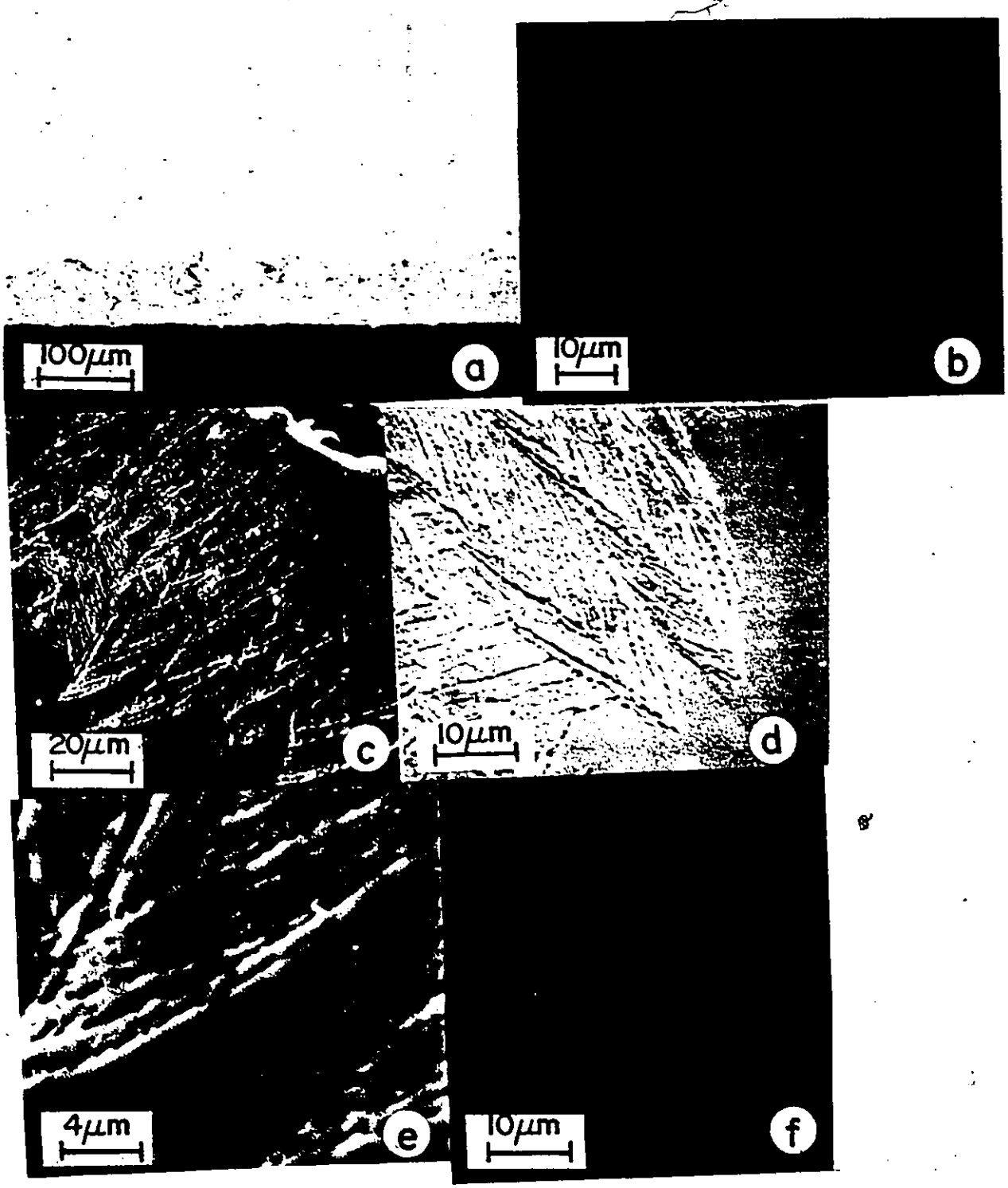
100μm
a
10μm
b
20μm
c
10μm
d
4μm
e
10μm
f

Figure 4.11

SEM of internal oxidation front

(a) SEM composite of internal oxidation front, oxidation time 10 hr, 700×

(b) Arrowhead from composite, 1.3K

(c) Intersection of arrowhead and lateral 2.45K

(d) Close-up of (c) 4.9K

(e) Close-up of (d), note how platelet goes from one colony to the other, 9.8K

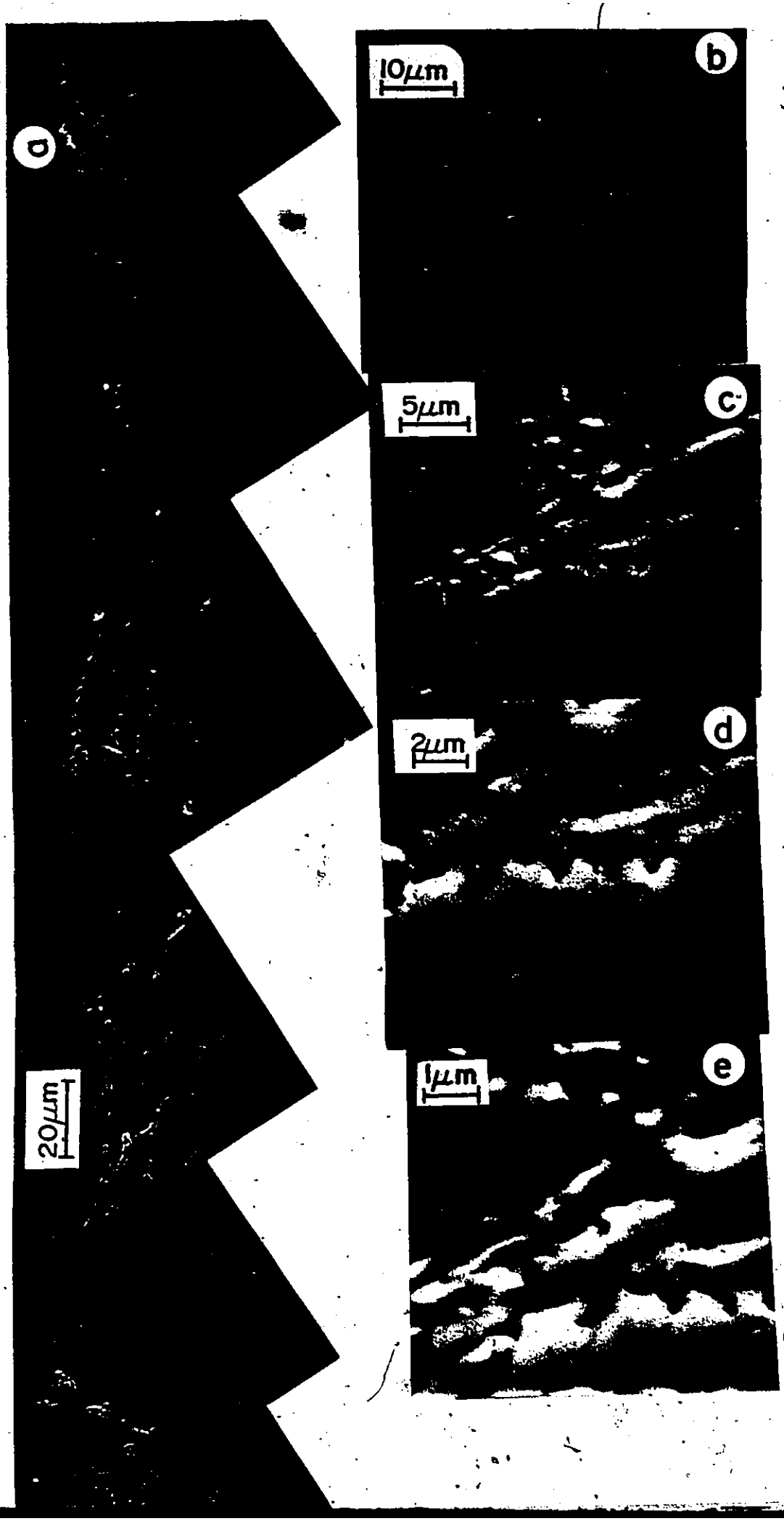
a
20μm
b
10μm
c
5μm
d
2μm
e
1μm

Figure 4.12

Transverse sections of Ag-10.9 wt % Zn

(a) Optical photograph, greater oxide density, oxidation time 78 hrs, 80×

(b) Optical photograph, internal oxide colonies becoming less distinctive, 350×

(c) SEM photograph showing platelets coarsening, 3.87K

(d) Oxide platelets transforming to general precipitates and dendrites, 7.92K

(f) Oxide platelets transforming to general precipitates and dendrites, 3.87K

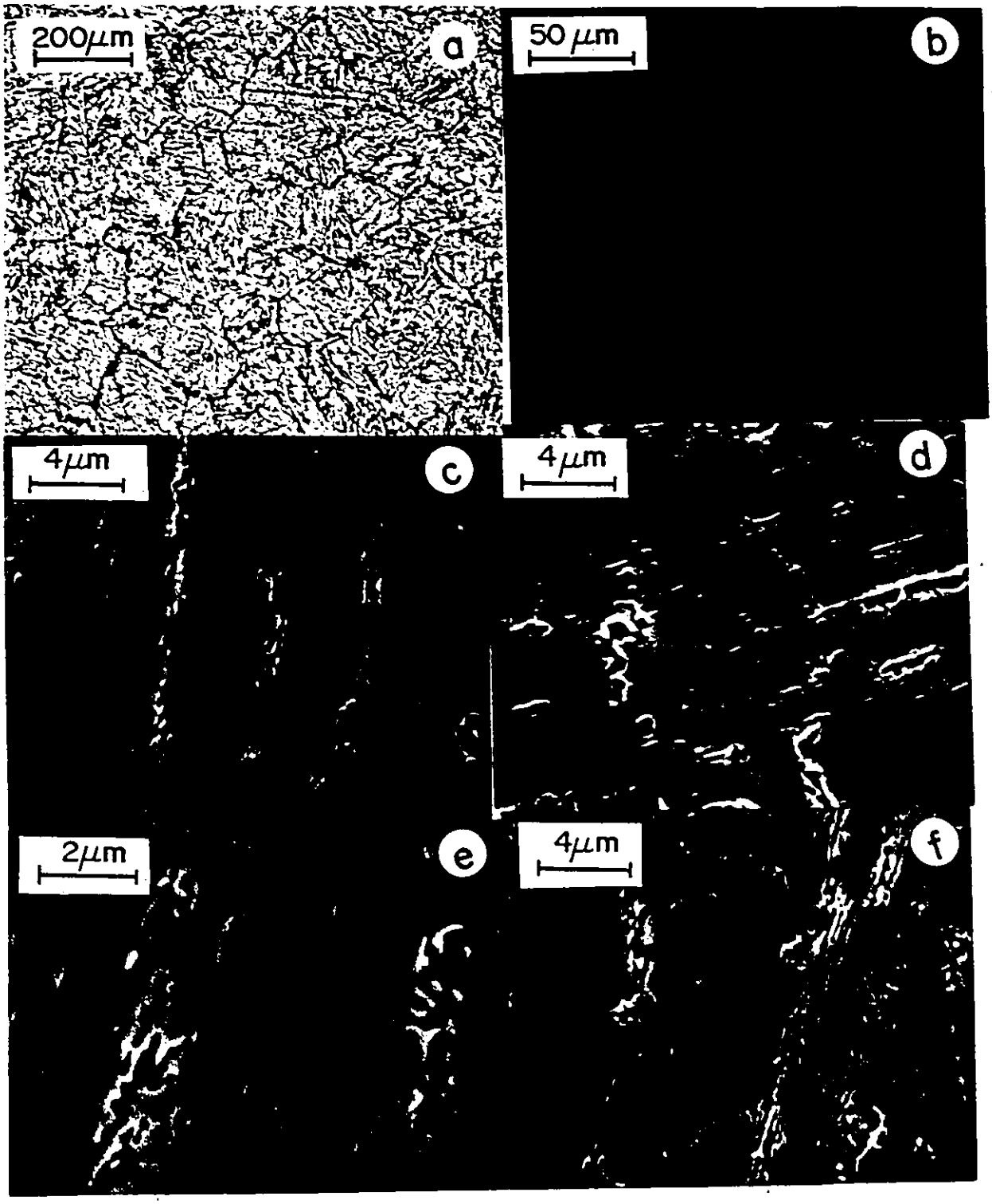
200μm
a
50 μm
b
4μm
c
4μm
d
2μm
e
4μm
f

0.11 mm below the surface. From the optical photographs one can see that the oxide region has become much denser and is showing a lesser crystallographic dependence. One can still see cross-hatching of the internal oxides. The SEM micrographs show the platelets growing thicker, some transforming to rods, others to irregular shapes (general precipitation), still others into dendrites. Some platelet character still remains.

Appendix 3 contains two colour photographs of the internal oxidation front in Ag-7.5 and 10.9 weight percent zinc alloys. The morphology, structure and growth characteristics of the internal oxidation zone and oxides found in all three alloys is comparable to the results obtained by Pickering[49] in his study considering the alloy differences.

4.2.3 Energy Dispersive X-ray Results for the Oxide Surfaces

The surfaces of samples of all three alloys, Ag-1.8, 7.5, and 10.9 wt % Zn have been examined by the optical and SEM microscopes. The surfaces of the samples prior to oxidation were similar to those given in Figure 3.2. Figure 4.13 (a), (b) show the surface of Ag-1.8 wt % Zn after .5 hr and 10 hr oxidizing respectively. X-ray dispersive analysis was used to determine the presence of zinc and silver on the surface. The point count technique was used with teletype print outs. The shiny areas are hills in Figure 4.13 (a) and gave only silver peaks Table 4-3 (a). The greyish

Figure 4.13

SEM micrographs of Ag-1.8 wt % Zn oxidized surface

(a) Oxidized time .5 hr, 1950×

(b) Oxidized time 10 hr, 850×

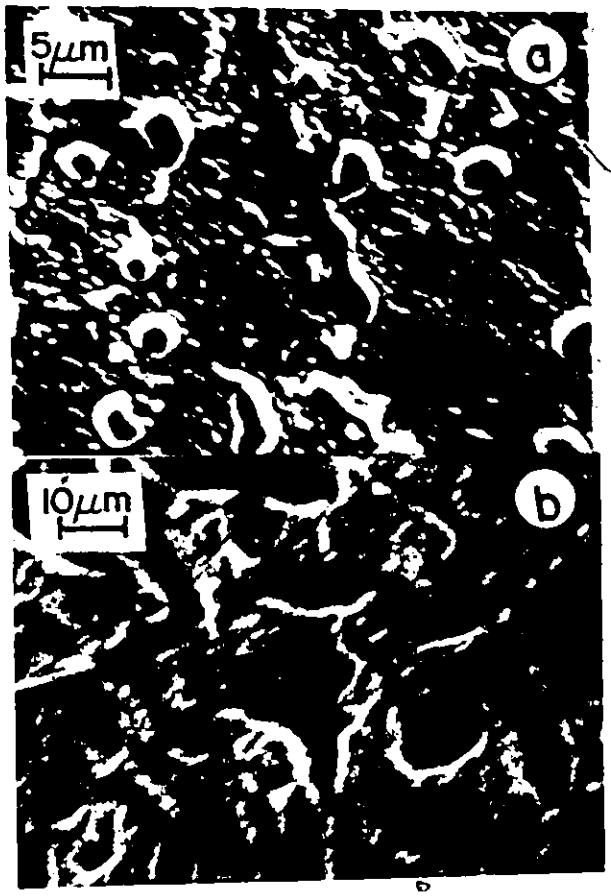
5μm
a
10μm
b

Table 4-3

X-ray Dispersive Analysis Point Count Output
for Ag-1.8 wt % Zn

(a) For Figure 4.13 (a), on a hill

No.	ECL	Centroid	FWHM	Area	Left	Right	Element
1	1	2.89	0.12	14698	142	163	Ag
2	1	3.09	0.08	1675	162	175	Ag

(b) For Figure 4.13 (a), in a valley

No.	ECL	Centroid	FWHM	Area	Left	Right	Element
1	1	2.89	0.12	13684	142	163	Ag
2	1	3.09	0.09	1325	162	174	Ag

(c) For Figure 4.13 (b), on a hill

No.	ECL	Centroid	FWHM	Area	Left	Right	Element
1	1	2.92	0.12	14769	145	165	Ag
2	1	3.13	0.01	3537	160	181	Ag

(d) For Figure 4.13 (b), in a valley

No.	ECL	Centroid	FWHM	Area	Left	Right	Element
1	1	2.91	0.11	5744	145	163	Ag
2	1	3.11	0.09	1396	163	176	Ag
3	1	8.55	0.15	1937	564	584	Zn

valley region also gave only silver peaks, Table 4-3 (b). The hills for the 10 hr sample indicate only silver while the valleys show silver and zinc, Table 4-3 (c), (a).

Figures 4.14, 4.15 contain optical, SEM and X-ray dot maps of the oxidized surfaces of 7.5 and 10.9 wt % Zn alloys respectively. In the optical photographs (a) and (b) for both alloys, the grey regions grow at the expense of the clear white areas. After 10 hours of oxidation the whole surface was not covered with the grey region. Point count analysis of the shiny white regions of 7.5 wt % Zn indicated only the presence of silver (Table 4-4(a)). While the white regions for 10.9 wt % Zn showed only the presence of silver for the .5 hr sample and both silver and zinc for the 10 hr sample (Tables 4-4,4-5).

The grey regions in the optical photographs are grey porous areas under the SEM, Figures 4.14 (c), (d), 4.15 (c), (d). Point count analysis of the grey region indicated both zinc and silver present (Tables 4-4, 4-5). X-ray dot maps for Figures 4.14 (c), (d), 4.15 (c), (d) exhibit the distribution of zinc across the surface. The surface topography, especially the porous oxide region, will lead to an error in the X-ray maps. Before each map was taken, the number of counts per second entering the counter was checked. The count rate was then adjusted to give a constant reading across the surface. This was accomplished by either tilting the sample or adjustment of one of the condensers.

Figure 4.14

Optical, SEM, and X-ray mapping for oxidized surface of Ag-7.5 wt % Zn

(a) Optical micrograph, oxidized time, .5 hr, 400×

(b) Optical micrograph, oxidized time 10 hr, 400×

(c) SEM micrograph, .5 hr, 8.5K

(d) SEM micrograph, 10 hr, 8.5K

(e) X-ray map of Zn for (c)

(f) X-ray map of Zn for (d)


40μm
a
40μm
b
2μm
c
2μm
d
e
f

Table 4-4

X-ray Dispersive Analysis Point Count Output
For Ag-7.5 wt % Zn

(a) For Figure 4-14 (d), on a hill-shiny area

No.	ECL	Centroid	FWHM	Area	Left	Right	Element
1	1	3.01	0.13	7810	152	173	Ag
2	1	3.20	0.01	294	167	187	Ag

(b) For Figure 4-14 (d), in the grey porous region

No.	ECL	Centroid	FWHM	Area	Left	Right	Element
1	1	3.01	0.12	3471	152	172	Ag
2	1	3.29	0.07	104	167	188	Ag
3	1	8.63	0.16	6392	573	594	Zn
4	1	9.57	0.18	867	644	665	Zn

Figure 4.15

Optical, SEM, and X-ray mapping for surface of Ag-10.9 wt % Zn

(a) Optical micrograph, oxidized time .5 hr, 1K

(b) Optical micrograph, oxidized time 10 hr, 800×

(c) SEM micrograph, .5 hr, 8.5K

(d) SEM micrograph, 10 hr, 8.5K

(e) X-ray map of Zn for (c)

(f) X-ray map of Zn for (d)

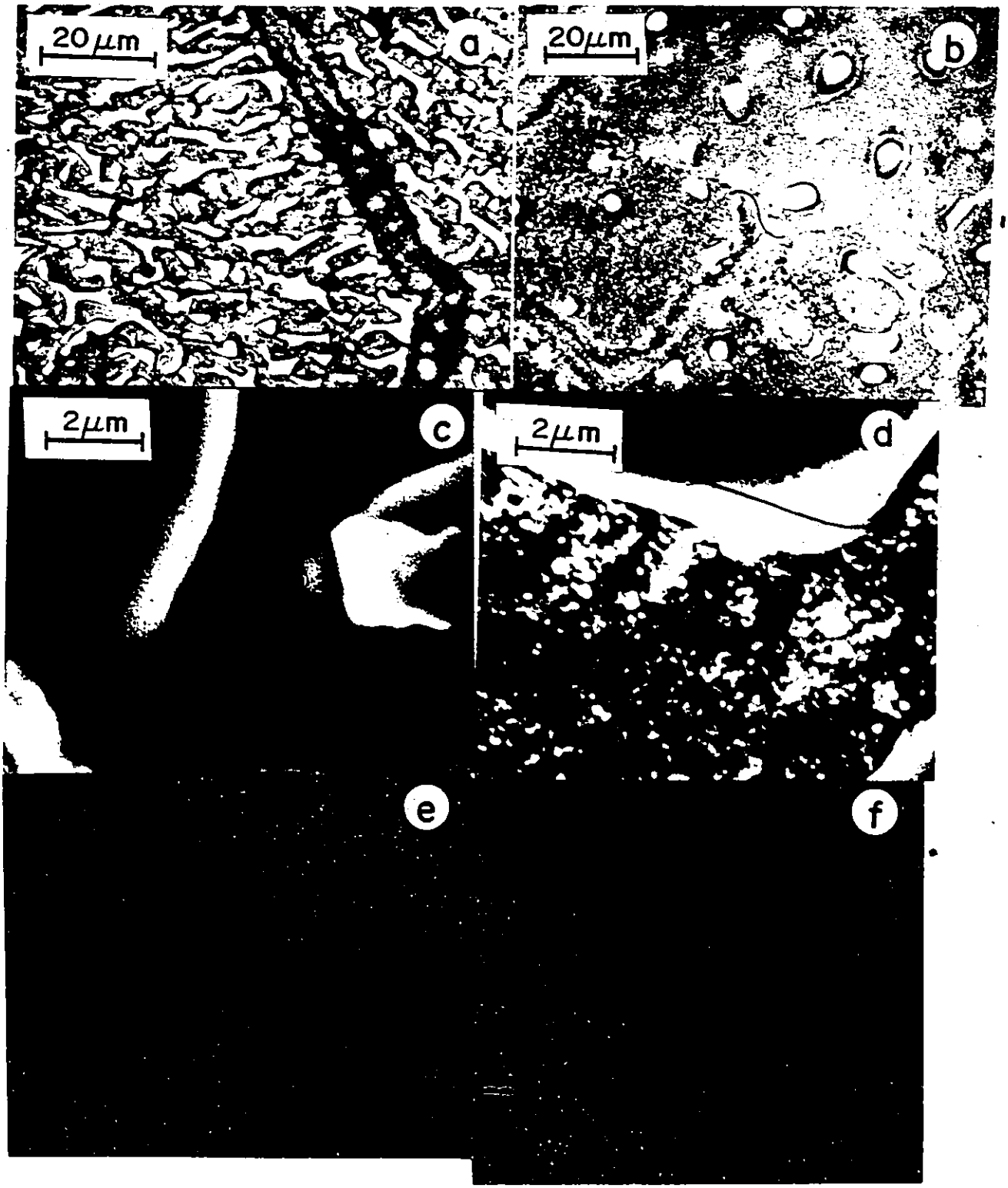
20 μm
a
20μm
b
2μm
c
2μm
d
e
f

Table 4-5

X-ray Dispersive Analysis Point Count Output
for Ag-10.9 wt % Zn

(a) For Figure 4.15 (c), on shiny region-hill

No.	ECL	Centroid	FWHM	Area	Left	Right	Element
1	1	3.00	0.12	1498	151	172	Ag
2	1	3.18	0.01	1726	166	187	Ag

(b) For Figure 4.13(c), in grey porous region

No.	ECL	Centroid	FWHM	Area	Left	Right	Element
1	1	2.99	0.12	2935	150	171	Ag
2	1	3.17	0.09	194	168	184	Ag
3	1	8.63	0.17	3212	573	594	Zn
4	1	9.55	0.10	475	644	660	Zn

(c) For Figure 4.13 (d), on shiny-region hill

No.	ECL	Centroid	FWHM	Area	Left	Right	Element
1	1	2.99	0.13	1877	131	171	Ag
2	1	3.22	0.10	140	166	186	Ag
3	1	8.62	0.14	2009	573	593	Zn
4	1	9.55	0.20	637	641	662	Zn

(d) For Figure 4.15 (d), in grey porous region

No.	ECL	Centroid	FWHM	Area	Left	Right	Element
1	1	2.97	0.13	9630	149	170	Ag
2	1	3.16	0.05	1324	164	185	Ag
3	1	8.61	0.16	4377	572	593	Zn

4.2.4 Electron Microprobe Analysis

The concentration profiles of Ag and Zn were determined across the internal oxidation zone of Ag-7.5, 10.9 wt % Zn alloys which were oxidized for 10 hours. Figures 4.16 (a), (b) give the profiles from within the alloy through the internal oxidation to the surface. A drop in the zinc concentration at the head of the internal oxidation front indicates enrichment of zinc in the zone of internal oxidation. This is also shown by the large increase in zinc at the start of the internal oxidation zone. As the electron beam passes over the internal oxidation zone, peaks of Zn are generated and valleys of silver where the internal ZnO resides.

Figures 4.17 (a), (b) are traces parallel to the surface across the internal oxidation zone for Ag-7.5, 10.9 wt % Zn alloys respectively. These traces show the alternating regions of high and low concentrations of Zn which one would expect if the internal ZnO formed as platelets normal to the surface. The blue valleys correspond to areas where Zn is depleted from the alloy. In some regions of the traces, the internal oxides were not resolved because the area analyzed by the beam is large relative to the oxide thickness. Consequently one gets Zn peaks of various sizes for the ZnO inside the internal oxidation zone. Not only can precipitate size cause this, but also the angle of inclination of the platelets with the surface.

Figure 4.16

Electron microprobe trace from the alloy across internal oxidation zone to the surface.

a) Ag-7.5 wt % Zn , Oxidation time 10 hr, Ag:red,Zn:blue.

b) Ag-10.9 wt % Zn, Oxidation time 10 hr, Ag:red,Zn:blue.

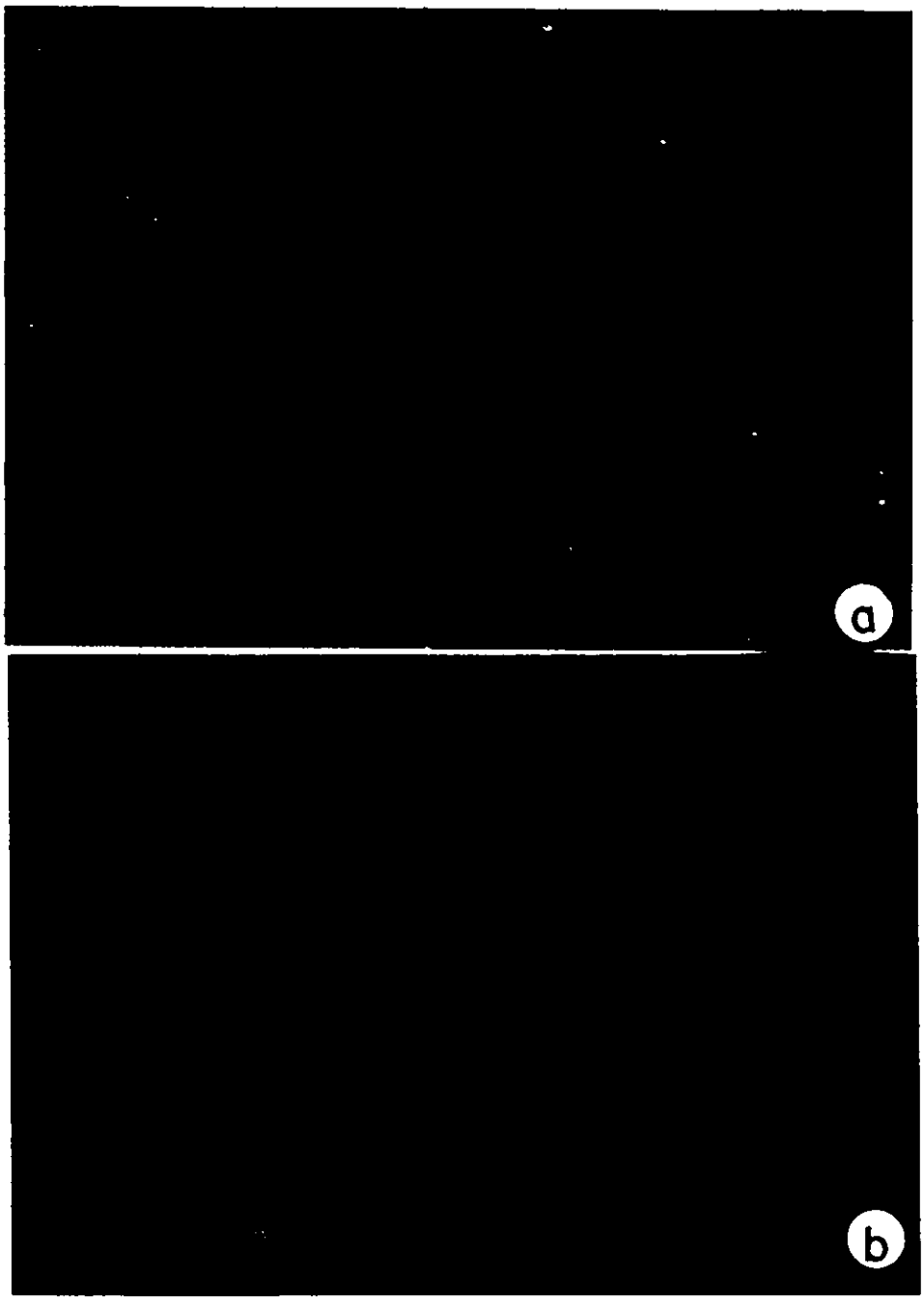
a
b

Figure 4.17

Electron microprobe trace across the internal oxidation zone parallel to the surface and perpendicular to a colony of oxides

a) Ag-7.5 wt % Zn, oxidation time 10 hr, Ag:red, Zn:blue.

b) Ag-10.9 wt % Zn, oxidation time 10 hr, Ag:red, Zn:blue.

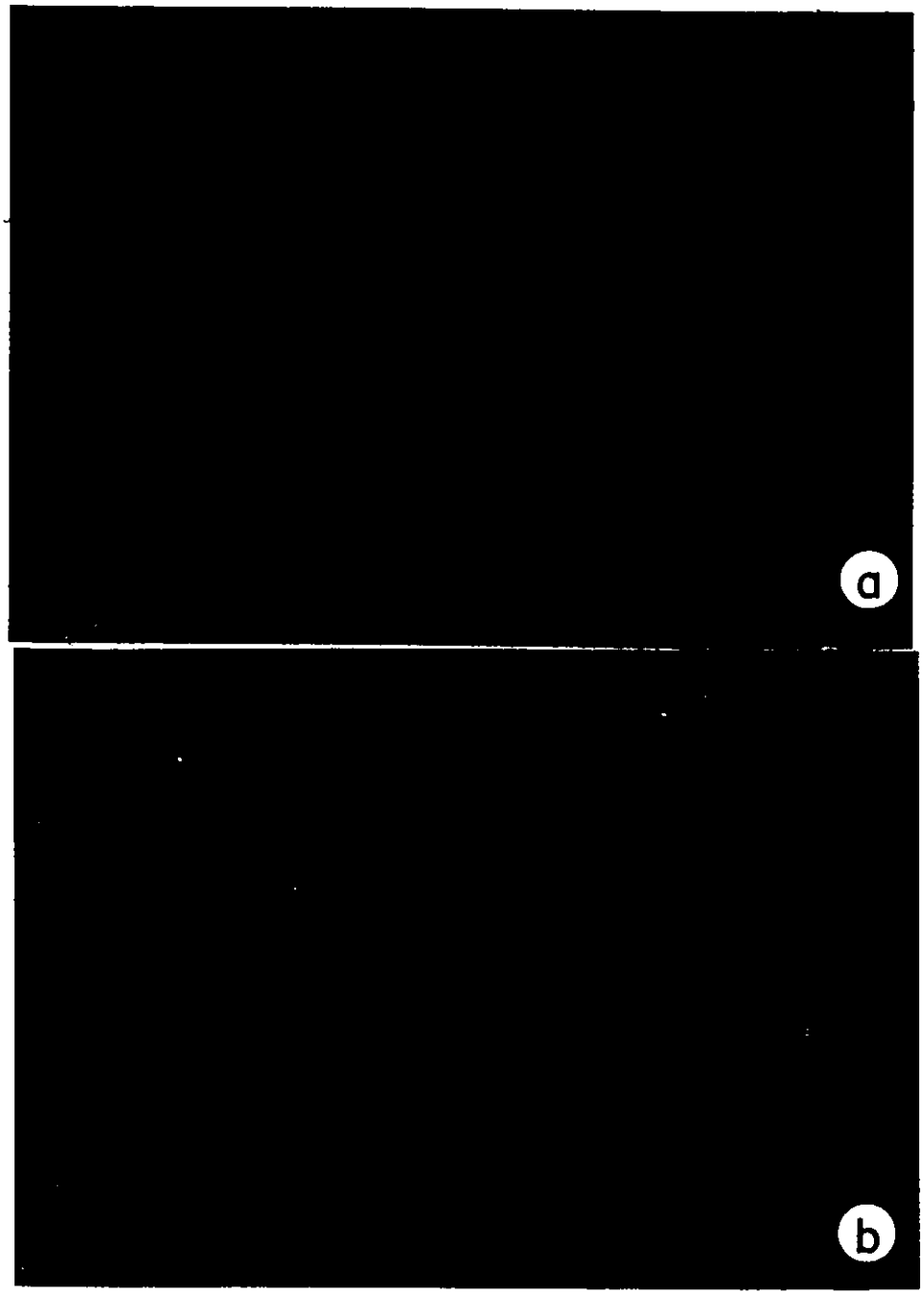
a
b

The traces were not determined for quantitative work but rather to show how close the profiles agreed with theory. The depletion region for zinc in Figures 4.16 (a), (b) is very narrow, 9 and 22 μ respectively. This corresponds to the model given in Figure 2.3.

4.3 Internal Oxidation in Combination with External Oxidation of ZnO in Ag-12.9 wt % Zn

4.3.1 Kinetics

Up to a time of 21 hours no predictable kinetic results could be produced for the growth of either the internal or external oxides. The experimental results obtained could not be fitted to the model given in Figure 2.2 for internal oxidation in combination with external oxidation. Nor was it possible to fit parabolic or linear models to either the internal or external scales.

A simple explanation for these results can be found from the microstructures. Initially a thin adherent external scale of ZnO forms on the surface, and any growth of internal oxide follows the model given by Figure 2.2 (oxygen being supplied at the dissociation pressure of the external oxide). But, as the external scale grew, it blistered, bubbled, sheared, cracked, and broke up due to the volume effect. Hence, paths are formed for rapid oxygen transfer to the surface of the alloy. Hence the internal oxide could grow with parabolic kinetics[52].

The average penetration for the internal oxides up to 21 hours was found to be 3.5×10^{-2} mm. The penetration

of the internal oxide as a function of time is given in Appendix 3.

4.3.2 Morphology and Structure of Internal Oxidation in Combination with External Oxidation

Figures 4.18 (a), (b) contain two optical micrographs in cross-section of internal oxidation in combination with external oxidation. Figure 4.18 (a) shows the external oxide has blistered and cracked, and depth of the internal oxide is greater here. The penetration of the internal oxidation zone was uniform over short distances but not across entire samples. Figure 4.18 (b) illustrates a region where the external oxide has lifted off slightly. Underneath there is an internal oxidation zone. Figure 4.18 (c) is a SEM micrograph of where the external oxide has cracked. Figure 4.18 (d) is an SEM micrograph of where the external oxide was very adherent to the external surface; no internal oxidation was observed here in the alloy.

Figure 4.18 indicates the external oxide is composed of two layers, one compact close to the surface, the other growing from within the compact layer outward as needles or whiskers. The morphology and structure of the external scale will be expanded upon in 4.4. No transverse sections are presented to show the structure of the internal oxides because the internal ozidation zone crumbled away on grinding, due to its thickness. The internal oxides have probably lost even more platelet character to rod, general and

Figure 4.18

Internal oxidation in combination with External oxidation of Ag-12.9 wt % Zn

(a) Optical micrograph, external and internal oxidation, oxidation time 21 hr, 800×

(b) Optical micrograph, blistering external oxide with internal oxidation, oxidation time 10 hr, 350×

(c) SEM micrograph, cracked external oxide, oxidation time 10 hr, 2K

(d) SEM micrograph, compact and adherent external oxide with no internal oxidation, note the whiskers, oxidation time 10 hr, 2K

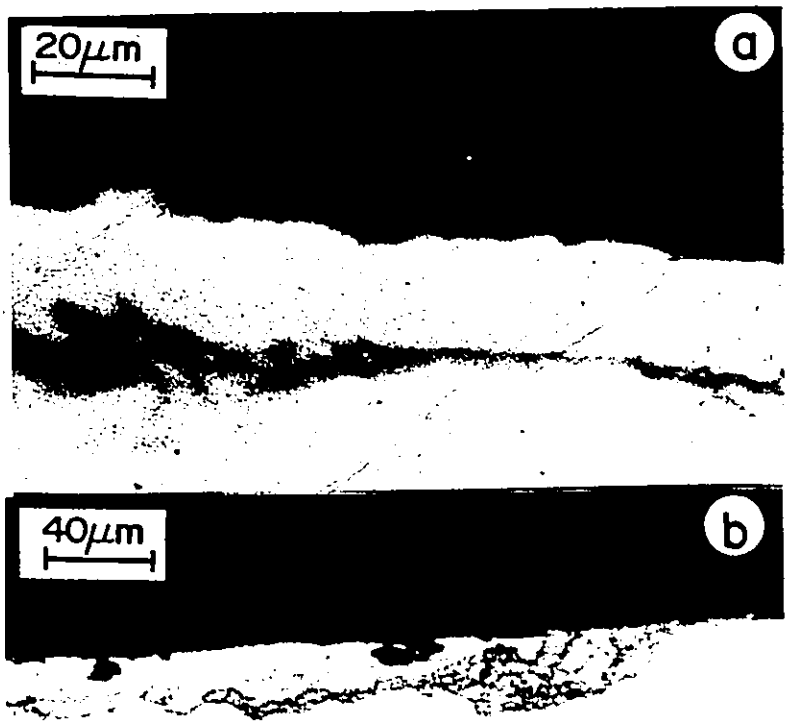
20μm
a
40μm
b

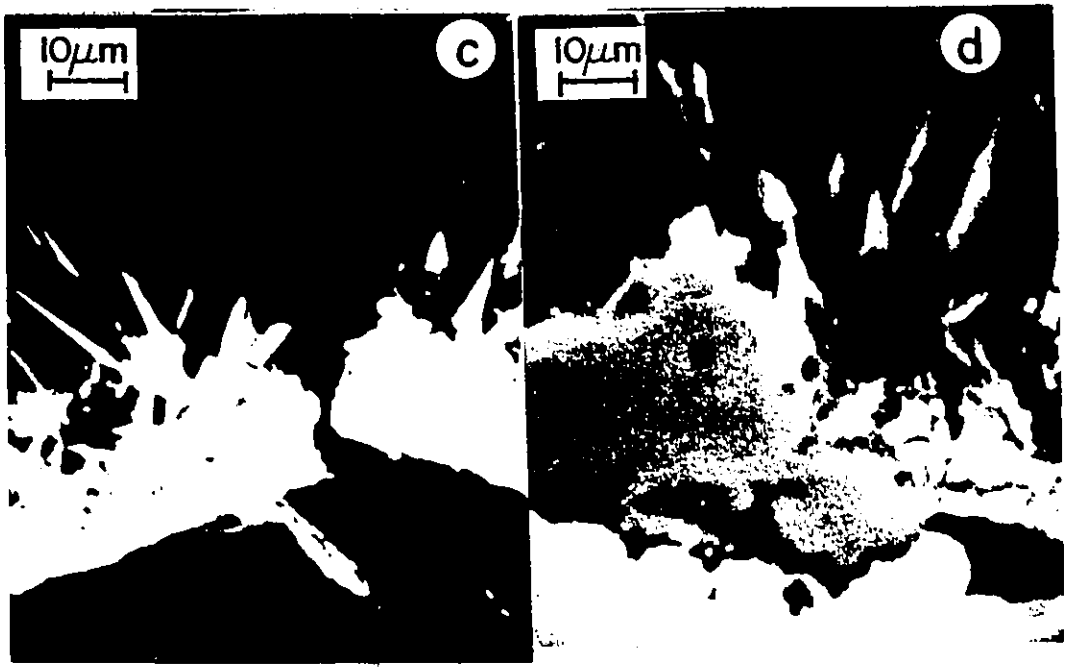
10μm
c
10μm
d

dendritic forms.

Figures 4.19 (a), (c) show an SEM micrograph and the corresponding X-ray dispersive map of zinc in the internal and external scales. The X-ray map indicates a large quantity of zinc in the external scale and at the head of the internal oxidation front. The point count analysis was used to supplement the X-ray map results and is given in Appendix 3, Figure A.3.3 and Table A-3-2. These results show the presence of zinc only in the external scale, silver and a small amount of zinc in internal oxidation zone, and finally both silver and zinc in the alloy.

Figure 4.19 (b) shows an edge where the external scale is very adherent and no internal oxidation occurred. The X-ray map (4.19 (d) indicates a large quantity of zinc in the external scale. The point count analysis discloses only the presence of zinc in the external scale (Appendix 3, Figure A.3.3 (b) and Table A-3-3).

4.4 External Oxidation of ZnO in Ag-18.7 Weight Percent Zn Alloy

4.4.1 Kinetics

Figure 4.20 gives the kinetic curve for the Ag-18.7 wt % Zn alloy. The curve was obtained by measuring the thickness of the external scale along the compact regions. The external scales were adherent to the surface except where they were damaged from preparation and lifted off due

Figure 4.19

SEM and X-ray mapping of Zn in the internal and external scales of Ag-12.9 wt % Zn

(a) Internal oxidation in combination with external oxidation, oxidation time 21 hr, 1.15K

(b) Exclusive external oxiation, oxidation time 21 hr, 980×

(c) X-ray map of Zn in (a)

(d) X-ray map of Zn in (b)

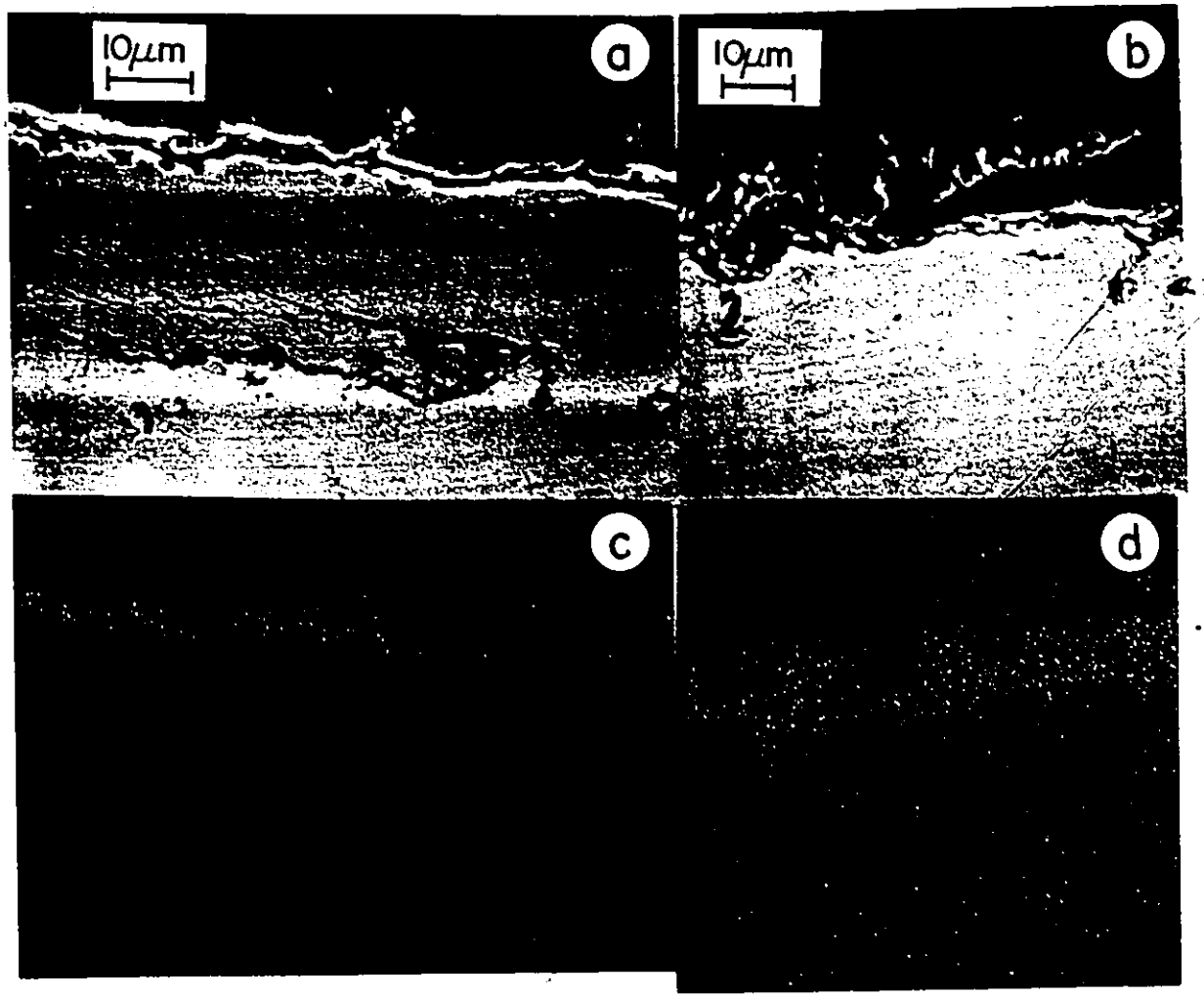
10μm
a
10μm
b
c
d

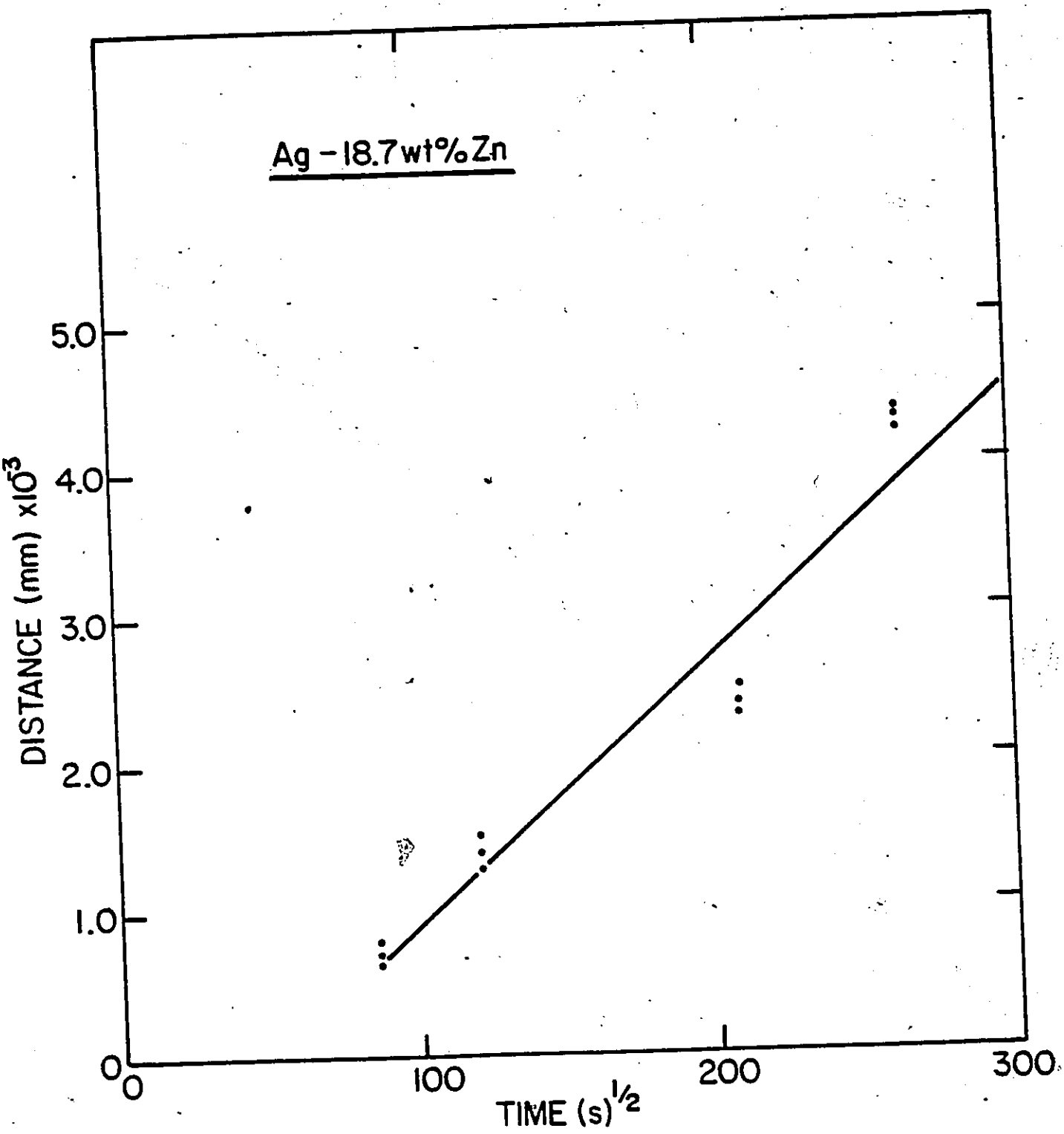

Figure 4.20 x vs $(t)^{1/2}$, Ag-18.7 wt % Zn

to differential thermal expansion. The external scales were found to be uniform along the lengths of all samples. The points were shown to obey a parabolic curve by means of the least squares method (and statistical results are given in Appendix 3, Table A-3-1).

Since parabolic kinetics are obeyed, volume diffusion of zinc through the external scale is controlling the growth of the oxide. These results are in agreement with those obtained by Rhines[53] and Dunn[54] for the growth of a protective adherent ZnO scale on Cu-Zn alloys. Raether[55] and Lucas[56] also found parabolic kinetics for the oxidation of pure Zn at 400°C.

4.4.2 Morphology and Structure of the External ZnO

Figure 4.21 contains optical, SEM and an X-ray map micrograph in cross-section of the external scale. The external scale is composed of a continuous layer with whiskers growing from within this layer outward. Lucas[56] found ZnO to form similarly on pure single crystals of zinc between 300°-400°C. The external oxide has lifted off the alloy slightly, probably due to differential expansion. No internal oxidation was found in any of the samples in this alloy. Figure 4.21 (e) is an X-ray dispersive map of Zn in Figure 4.21 (d). It indicates a large quantity of Zn in the external scale. The point count technique was used to analyze the content of the external scale and matrix.

Figure 4.21

External scale of ZnO on Ag-18.7 wt % Zn in cross-section

(a) Optical micrograph, showing external scale oxidation time, 21 hr, 800×

(b) SEM micrograph, external scale, oxidation time, 2 hr, 2.05K

(c) SEM micrograph, external scale, oxidation time 21 hr, 2.15K

(d) Same as (c)

(e) X-ray map of Zn in (d), 2.15K

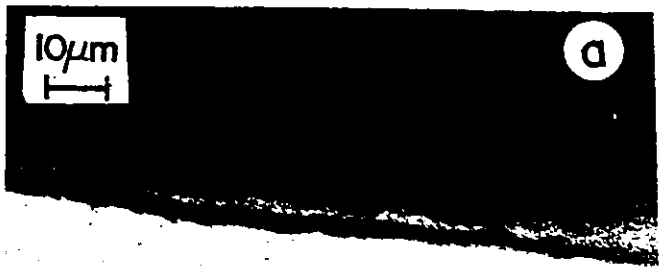
10μm
a

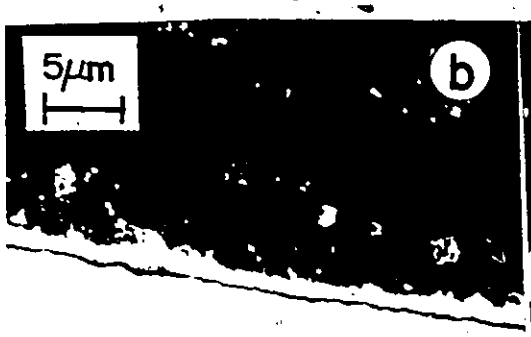
5μm
b


5μm
c

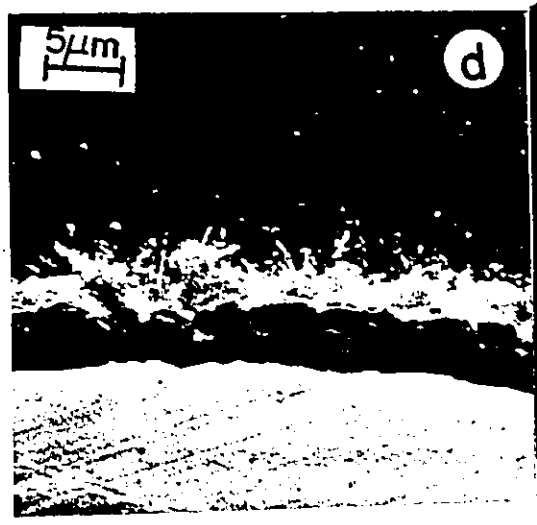
5μm
d

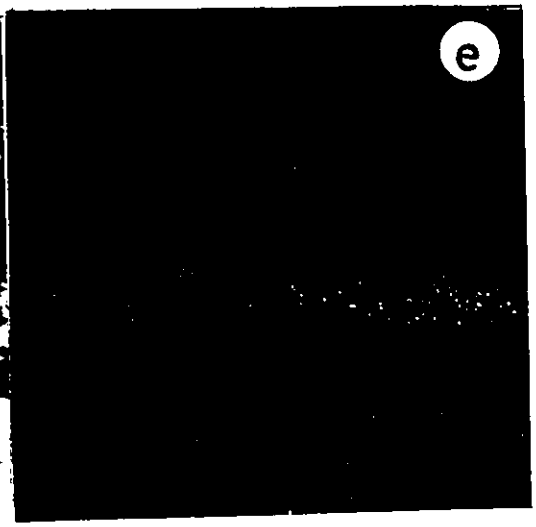
e

Table 4-6

Point Count Analysis for Figure 4.21 (d)

(a) External Oxide

No.	ECL	Centroid	FWHM	Area	Left	Right	Element
1	1	1.02	0.12	3382	11	31	Zn
2	1	8.64	0.13	4275	609	630	Zn
3	1	9.56	0.13	673	682	702	Zn

(b) Matrix

No.	ECL	Centroid	FWHM	Area	Left	Right	Element
1	1	2.98	0.12	4412	165	185	Ag
2	1	8.63	0.14	694	609	630	Zn

The results are shown in Table 4-6, which shows only the presence of zinc in the external scale and both silver and zinc in the matrix.

4.4.3 Energy Dispersive X-ray Results for the External Scale

In order to study the nucleation of ZnO on the surface two samples were especially prepared. They were polished down to 1 micron with diamond paste, very slowly by hand, using one drop of lapping oil on a selvyt cloth. A very minimal amount of pressure was used to prevent surface damage. It was found that many 600 and 6 μ scratches remained. Pitting and diamond imbedding was common due to the softness of the alloy.

Figure 4.22 (a), (b) are optical micrographs of the oxidized surface after 21 hours of oxidation. Figure 4.22 (c) is an SEM micrograph of the oxidized surface after 1 hour of oxidation. Point count analysis of the surface revealed the matrix and the little white nodules to be made up of a mixture of silver and zinc. Figure 4.22 (d) is the oxidized surface (SEM) after 21 hours. Analysis of the matrix (greyish area) gave both silver and zinc, while analysis of the white nodules revealed a large amount of zinc and a lesser amount of silver. These results are given in Table 4-7. The nodules size and density on the surface increased with oxidation time. The nodules are the

Figure 4.22

Topography of the External Scale

(a) Optical micrograph, oxidized surface, 1μ finish, oxidized 21 hours, 100×

(b) Optical micrograph, oxidized surface, 1μ finish, oxidized 21 hours, 1000×

(c) SEM micrograph, oxidized surface, 1μ finish, greyish compact layer, white nodules, oxidized 1 hour, 5.1K

(d) SEM micrograph, oxidized surface, 1μ finish, greyish compact layer, white nodules growing into whiskers, oxidized 21 hours, 9.7K

(e) SEM micrograph, oxidized surface, electroetched surface, whiskers growing out of compact layer, oxidized 24 hours, 792×

(f) Close-up of (e), 1.58K

(g) SEM micrograph, used for X-ray point count analysis of the whiskers, 8.5K

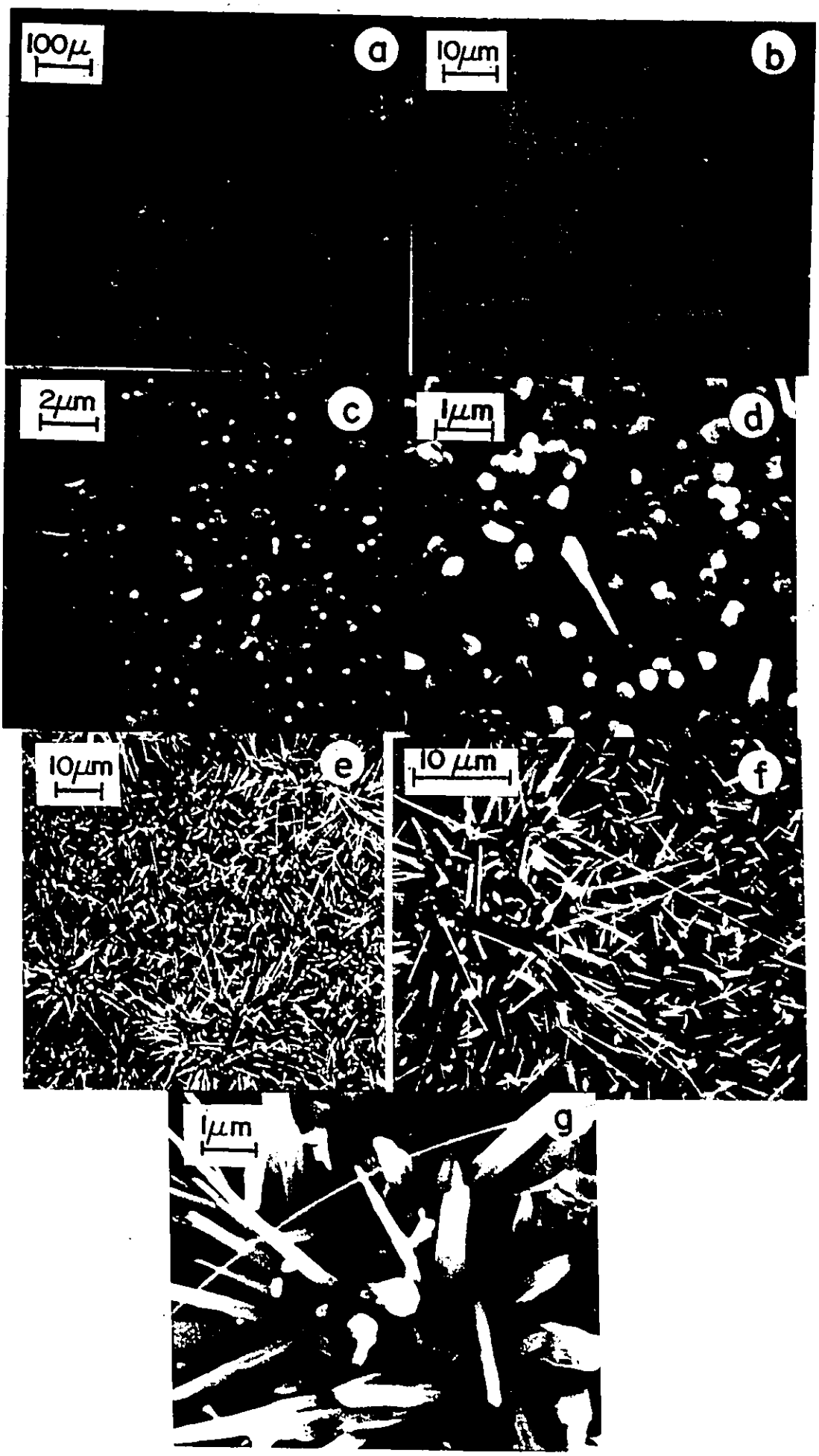
100μ
a
10μm
b
2μm
c
1μm
d
10μm
e
10 μm
f
1μm
g

Table 4-7

Point Count Results for Figure 4.22 (c), (d)

a) Figure 4.22 (c), matrix

No.	ECL	Centroid	FWHM	Area	Left	Right	Element
1	1	2.99	0.12	2804	173	193	Ag
2	1	8.62	0.16	404	614	635	Zn

b) Figure 4.22 (c), nodule

No.	ECL	Centroid	FWHM	Area	Left	Right	Element
1	1	1.03	0.12	1184	18	39	Zn
2	1	2.99	0.13	2446	172	193	Ag
3	1	3.20	0.04	371	193	205	Ag
4	1	8.64	0.16	1798	615	636	Zn

c) Figure 4.22 (d), matrix

No.	ECL	Centroid	FWHM	Area	Left	Right	Element
1	1	1.02	0.12	840	18	38	Zn
2	1	2.99	0.12	1607	172	193	Ag
3	1	8.63	0.15	791	615	635	Zn

d) Figure 4.22 (e), nodule

No.	ECL	Centroid	FWHM	Area	Left	Right	Element
1	1	1.01	0.11	2462	17	38	Zn
2	1	2.98	0.13	804	172	192	Ag
3	1	8.62	0.14	256	614	635	Zn
4	1	9.58	0.08	256	689	709	Zn

long whiskers in their early stages of growth. The grey region is the compact zinc oxide layer seen in cross-section. Counts of silver are obtained in these results because the electron beam penetrates 1-2 microns into the surface, hence X-rays are emitted from these regions.

Figures 4.22 (e), (f), (g) are SEM micrographs of the oxidized surface 24 hours which have undergone electro-etching. The whiskers are much larger here. Table 4-8 lists the results for point count analysis of the whiskers in Figure 4.22 (g), and indicates only Zn present.

4.4.4 X-ray Diffraction Results for the External Oxide on a Ag-18.7 wt % Zn Alloy

The pattern on the film strip from the Debye-Scherrer camera has been analyzed using the film-measuring device to locate the position of the lines. The calculated experimental values for the "d" spacings and the relative line intensities as well as those for ZnO (zincite) from the ATSM[57] Microfiche Index are given in Table 4-9. Only the first nine d spacings are given because the others were too weak to read properly. There is almost an exact match between the experimental results and those given for ZnO (zincite), thus the oxide formed on the Ag-18.7 wt % Zn alloy is hexagonal-ZnO (zincite).

Table 4-8

Point Count Results for Whiskers, Figure 4.22 (g)

No.	ECL	Centroid	FWHM	Area	Left	Right	Element
1	1	1.10	0.12	3438	18	38	Zn
2	1	8.71	0.15	4782	615	635	Zn
3	1	9.64	0.15	739	688	708	Zn
1	1	1.11	0.12	648	18	38	Zn
2	1	8.71	0.14	5236	615	636	Zn
3	1	9.64	0.16	643	688	709	Zn
1	1	1.10	0.11	1177	17	38	Zn
2	1	8.71	0.15	4539	615	635	Zn
3	1	9.65	0.14	285	689	710	Zn

Table 4-9

Comparison of X-ray Patterns

Experimental Pattern; Cu-K_α, λ=1542 Å		Pattern of ZnO (zincite), Hexagonal system; Cu-K_α, λ=1.542 Å		
d(Å)	I/I_1	ASTM Suggested	d(Å)	I/I_1
2.777	Strong	70 - 80	2.816	71
2.583	Medium	50 - 60	2.602	56
2.466	Very, very, strong	100	2.476	100
1.887	Weak	30 - 40	1.911	29
1.610	Medium	50 - 60	1.626	40
1.466	Weak	30 - 40	1.477	35
1.394	Very faint	10	1.407	6
1.366	Weak	20 - 40	1.379	28
1.344	Faint	20	1.359	14

CHAPTER 5

DISCUSSION OF EXPERIMENTAL RESULTS

5.1 Introduction

In Chapter 4 the results have been presented in three sections according to the oxidation products produced. A similar format will be used in this chapter.

When a Ag-Zn alloy is exposed to oxygen at 550°C, ZnO may form internally, externally, or in a combination of both, according to the following reactions:

$$2Zn(\text{alloy}) + O_{2(g)} = 2ZnO(\text{internal}) \qquad (5\text{-}1)$$

$$2Zn(\text{alloy}) + O_{2(g)} = 2ZnO(\text{external}) \qquad (5\text{-}2)$$

$$2Zn(\text{alloy}) + O_{2(g)} = Zn(\text{internal}) + Zn(\text{external}) \qquad (5\text{-}3)$$

The driving force for the above reaction is the free energy of formation of ZnO. The standard free energy of formation of ZnO at 550°C from the pure components is:

$$2Zn(s) + O_2(g) = 2ZnO(s) \quad \Delta G^\circ = -95,170 \text{ cal/mole}^{(58)} \qquad (5\text{-}4)$$

Initially the zinc oxides may not be in equilibrium with the alloy in view of their rapid formation. This stage of oxidation is referred to as "transient oxidation"[59]

and is sensitive to surface preparation and the partial pressure of oxygen. Once equilibrium is reached, the dominant reaction (5-1), (5-2), (5-3) will be determined by the zinc content in the alloy, the oxygen pressure in the oxidizing atmosphere and on the surface preparation.

Construction of the Ag-Zn-O ternary isotherm at 550°C is required for the application of the ternary diffusion formalism. No Ag-Zn-O ternary isotherm has been determined thus far. Some simple assumptions will be made to generate part of the diagram. The equilibrium in (5-4) between ZnO, Zn and O_2 allows an equilibrium constant to be defined:

$$\ell nK = \ell n\, a_{ZnO} - \frac{1}{2}\,\ell n\, P_{O_2} - \ell n\, a_{Zn} \,. \qquad (5\text{-}5)$$

Using the standard free energy change for (5-4) a value for K can be obtained:

$$K = \exp(\Delta G^{\circ}/RT) = 1.88\times10^{25} \,. \qquad (5\text{-}6)$$

For simplicity a solubility product based on activities instead of concentration because the activity coefficient for oxygen is unknown.

$$a_O \cdot a_{Zn} = K' = 1/K = 5.3\times10^{-26} \quad (a_O = P_{O_2}) \,. \qquad (5\text{-}7)$$

Also one assumes that no ternary oxide nor silver oxides are stable, and no silver is soluble in the zinc oxide. Equation (5-7) may be used to generate an oxygen solubility

curve based on the activity of oxygen in the alloy. Table 5-1 gives the corresponding activities of oxygen for each alloy composition. The oxygen solubility in pure silver is

Table 5-1

Alloy Composition and Oxygen Activity

Alloy Composition	Activity Zinc	Oxygen Activity atm
Ag-1 wt % Zn	0.002	2.7×10^{-23}
Ag-10 wt % Zn	0.022	2.4×10^{-24}
Ag-25 wt % Zn	0.09	5.9×10^{-25}
Ag-30 wt % Zn	0.2	2.7×10^{-25}
Ag-50 wt % Zn	0.34	1.6×10^{-25}
100 wt % Zn	1	5.3×10^{-26}

4.7×10^{-5} [20] oxygen atom fraction at 550°C. The above data have been transferred onto Figure 5.1. The complex region of the diagram at alloy concentrations greater than 25 wt % Zn have been omitted because the equilibrium lines have not been determined. In Figure 5.1 (b) a more complete isotherm is given as one does not know the exact position of point F, but the general shape and approximate position of F in the region is given. The approximate position of F is based on an alloy of .02 wt % Zn which did not show any internal oxidation under SEM. The dissolved oxygen concentration of the

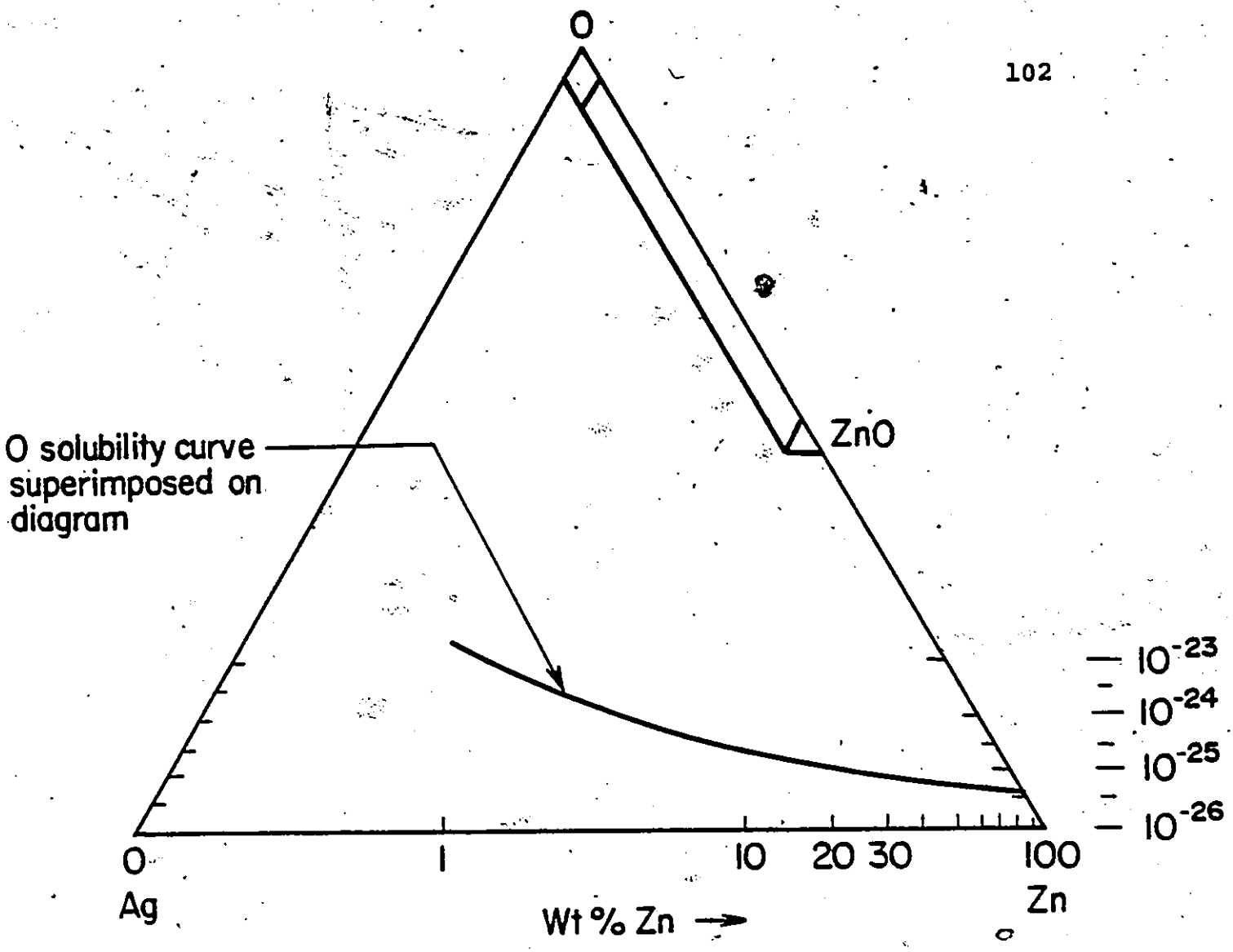

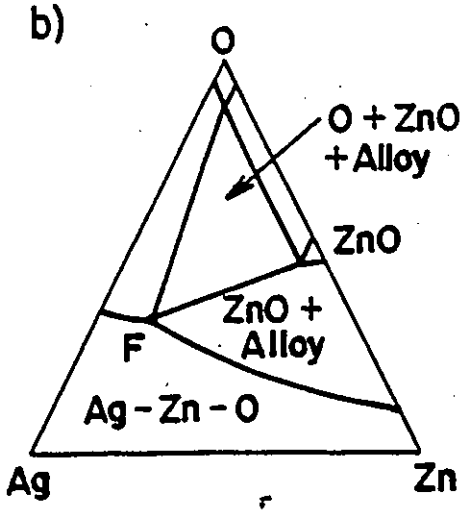

Figure 5.1 Ag-Zn-O Ternary Isotherm at 550°C.

alloy was not determined, which would fix the position of F.

5.2 Internal Precipitation and Growth of ZnO in Ag-Zn Alloys

5.2.1 Internal ZnO Structure and Morphological Development

This section deals with the internal ZnO precipitate structure in Ag-1.8, 7.5 and 10.9 wt % alloys and the structural changes which occur to the internal ZnO and to the internal oxidation zone in these alloys. The internal ZnO in the Ag-1.8 wt % Zn alloys grows in the form of rectangular plates with a rounded tip (Figures 4.5, 4.6). The plates in the Ag-1.8 wt % Zn alloy grow as weakly coupled colonies inward from the external surface[60]. The plates grow on specific crystallographic planes within the alloy (Figures 4.4, 4.6) and are sometimes found to align themselves with twin boundaries. Within a given grain all the plates grow in one or two favoured crystallographic directions. These observations are in agreement with the results obtained by Pickering[49]. The angles of intersection of the growth planes with the external surface and the polished surface determine the growth direction of the plates seen. Figure 5.2 gives a schematic diagram of the intersection effect. The diagram and explanation provide a reasonable description for the different types of morphological observations obtained in Figure 4.4, especially with regard to colonies growing parallel to the external surface.

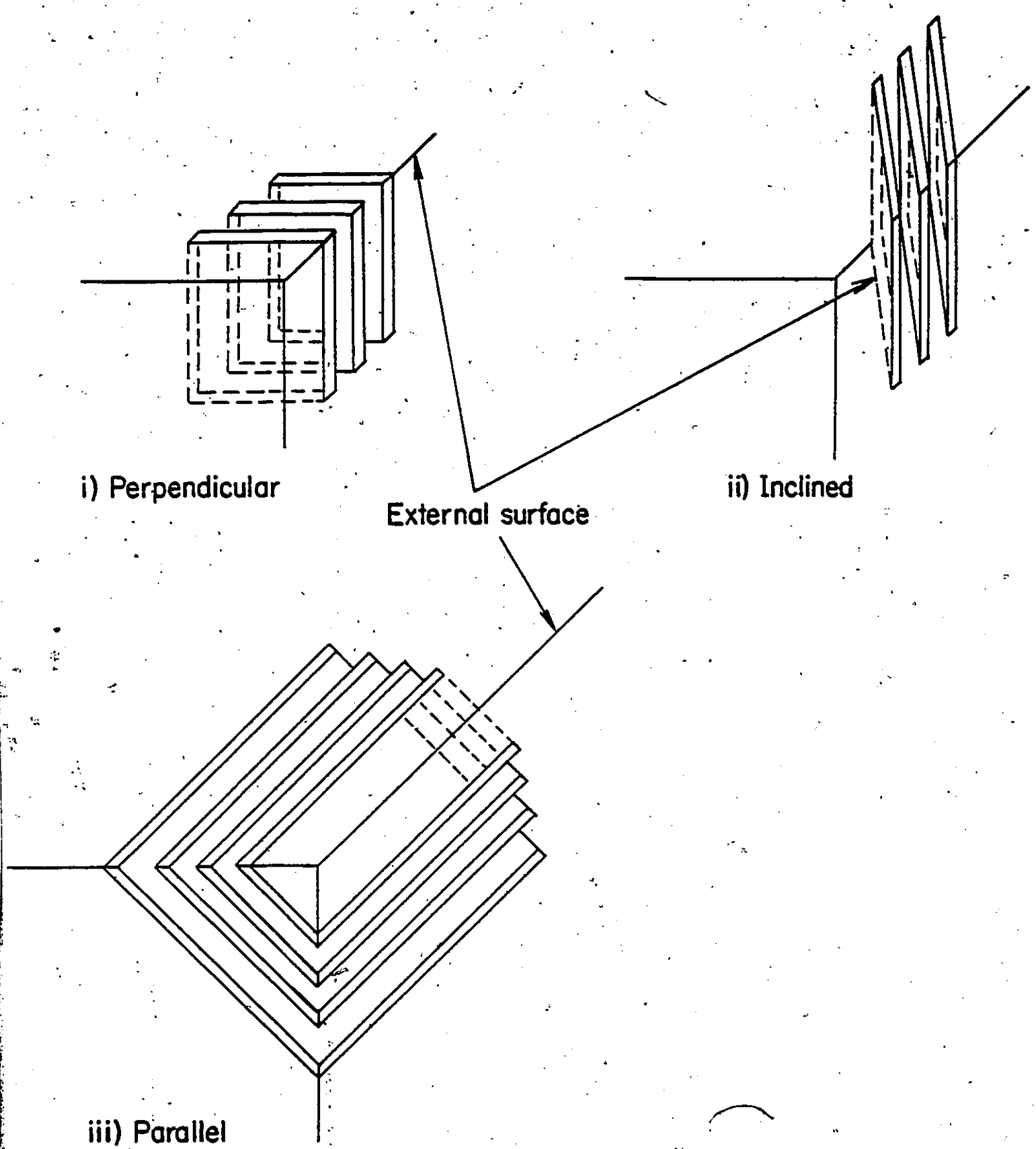

Figure 5.2 Intersection Effect on the Growth Internal ZnO Plates.

The Ag-7.5 and 10.9 wt % Zn alloys show considerable change in the morphology of the internal ZnO precipitates as well as the internal oxidation zone. The penetration depth of the internal oxidation zone into these alloys has decreased by 1/4 and the density of internal oxides in the internal oxidation zone has increased significantly. The internal ZnO in these two alloys grows as strongly coupled colonies of parallel plates[60]. The internal oxide still shows a crystallographic growth dependence in both Ag-Zn alloys (Figures 4.9, 4.12). The spacing between the plates has increased by a factor of 2.5 (Table 5-3) compared to the Ag-1.8 wt % Zn alloy and the thickness of the internal oxides has increased by a factor of 6. The plates in the Ag-7.5 and 10.9 wt % Zn alloy have thickened by a local process which can lead to a general (spherical) precipitate forming (Figures 4.9 (c), (e); 4.12 (d), (f)). Also, side branching from the main plate can lead to the formation of dendrites or rods.

For the Ag-7.5 and 10.9 wt % Zn alloy two different types of morphology were discovered, "arrow-head" and a lateral growth of plates parallel to the external surface. These two types of colonies are of the same origin, but appear to be different because of their angles of inclination with the polished surface. This point is schematically shown in Figures 5.2 and 5.3. The lateral growth of plates might,

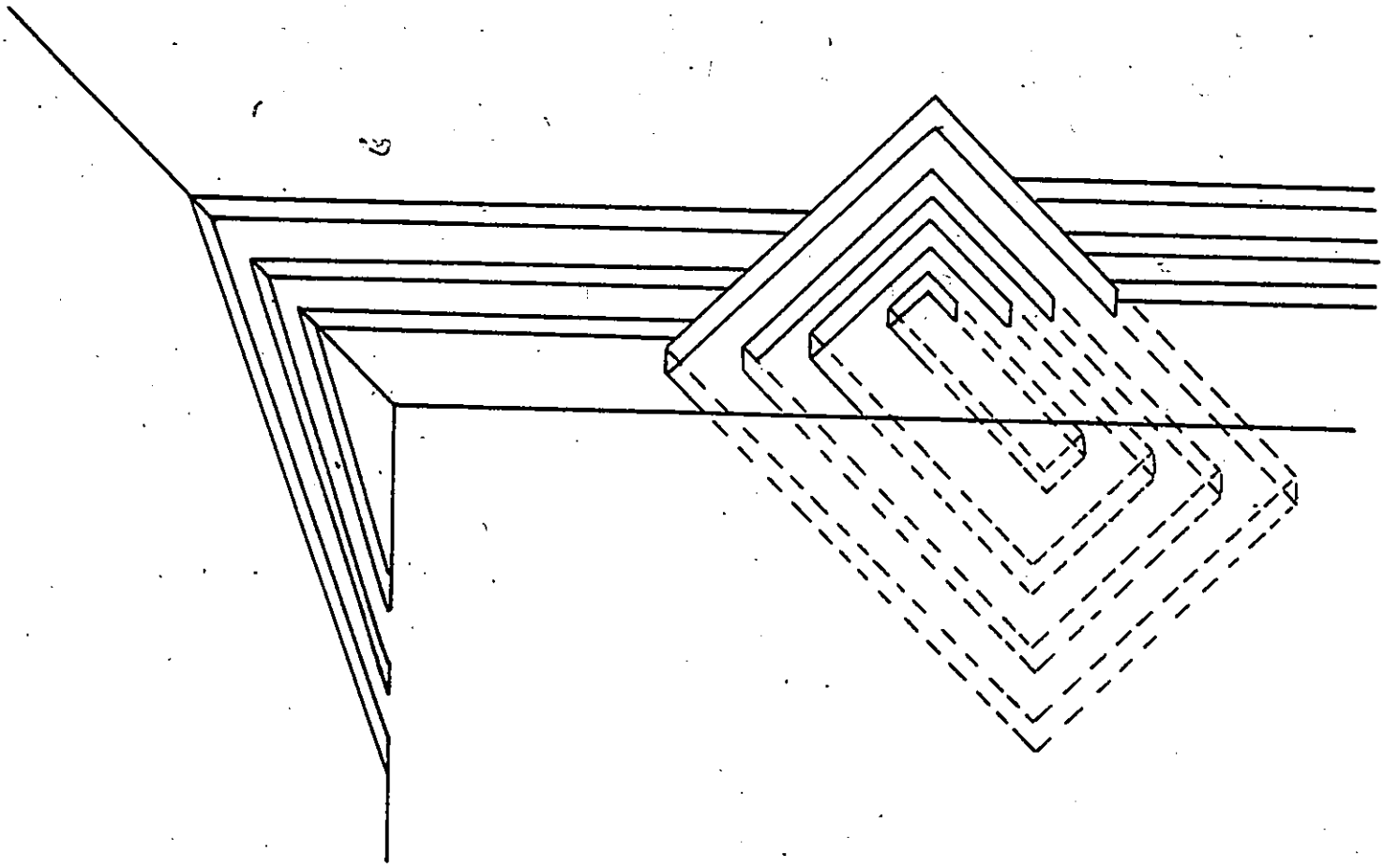

Figure 5.3 Arrowhead and Lateral Growth of Plates.

on the basis of sectioning effects, be classified as a type of Liesegang[62,63] phenomenon. This would not however be in accord with the classical definition, discussed next.

5.2.2 Liesegang Phenomena Versus Lateral Growth of Plates

Liesegang phenomena was discovered 85 years ago by R. E. Liesegang[62,63] in the study of periodic precipitation in gelatin-electrolyte systems. "Liesegang rings or bands are formed when a substance usually a salt, is allowed to diffuse into a non-convective solution containing a dissolved salt which upon reacting with the diffusing material forms an insoluble precipitate. Under the proper conditions the precipitate does not form continuously along the direction of diffusion, but rather it forms in bands perpendicular to the direction of diffusion"[64].

There is only a handful of publications in the literature which mention Liesegang bands formed by internal oxides in solids. F.N. Rhines[21,52,53] found Liesegang bands in Cu and Ag alloys. Kleuth[65] and Mullins and Kirkaldy[71] have modified the Wagner[66] mathematical model for periodic precipitation in gelatin-electrolyte systems for precipitation of internal oxides in solids. Klueth and Mullins model is somewhat similar to that given in Chapter 2.4.3 for the number of primary oxide particles per unit volume.

If the internal ZnO plates in Ag-7.5 and 10.9 wt %

Zn alloy were precipitated periodically parallel to the external surface, the plates themselves would act as barriers to the diffusion of oxygen. This is because oxygen diffusion through the internal ZnO would be extremely small and set by the dissociation pressure of ZnO. Supplying oxygen by diffusion around the plates at the boundary between the matrix-oxide seems unlikely because of the distance involved for oxygen diffusion. Porous regions and holes in the plates exist where oxygen may penetrate (Figure 4.12 (e)) but this still would not provide enough oxygen for a new plate. For the formation of true Liesegang[62,63,64] phenomena the internal oxide must precipitate and grow in a morphology (spherical, rods or lathes) which allows the passage of oxygen through the channels between the precipitates.

This argument puts some of the conclusions of F. N. Rhines[21,52,53] in Cu alloys in doubt, i.e. whether the alloys containing the continuous internal oxide bands parallel to the external surface are true Liesegang phenomena or not. The observations obtained by F. N. Rhines have been made on only one cross-section view of the internal oxides and without the use of deep-etching. If a reference is required for observation of true Liesegang phenomena in solids the work by R. L. Kleuh[64,65] and W.W. Mullins should be referred to. The lateral growth of plates in this study may be referred to as an "apparent orientational Liesegang" phonemon because it has been created by an orientation effect.

5.2.3 Model for the Growth of Internal ZnO in Ag-Zn Alloys

When a Ag-Zn alloy containing less than 11 wt % Zn is exposed to oxygen (1 atm) at 550°C, internal precipitation of ZnO occurs. The internal oxidation front proceeds by parabolic kinetics into the alloy as shown in Figure 4.1, 4.2 and 4.3. The internal ZnO precipitates as parallel lamallae of ZnO on specific crystallographic orientations within a given grain (refer to Figures 4.4 through 4.12).

A simple volume diffusion controlled model for the growth of internal oxides in Ag-1.8, 7.5 and 10.9 wt % Zn will now be given. Since parabolic kinetics have been found, the use of equation (2-8) allows the determination that oxygen diffusion is controlling the growth of the front. This is accomplished by determining the products of $N_O^{(S)}$. D_O from Figures 4.1, 4.2, 4.3 and equation (2-8). One then compares these products with those calculated from selected literature values of $N_O^{(S)}$ and D_O. The calculated products for all three alloys and the product from the literature values are given in Table 5-2. The exact details of the calculations and references are given in Appendix 4. Good agreement between the results means oxygen control over the growth of the internal oxides.

Table 5-2

A Comparison of $N_o^{(S)} \cdot D_o$ products for Ag-1.8, 7.5, and 10.9 wt % Zn

Alloy	$N_o^{(S)} \cdot D_o$ eqn. (2-8)	$N_o^{(S)} \cdot D_o$ literature
	(atom.fraction)(cm^2/sec)	(atom fraction)(cm^2/sec)
1.8	5.6×10^{-10}	2.1×10^{-10}
7.5	2.8×10^{-10}	2.1×10^{-10}
10.9	1.6×10^{-10}	2.1×10^{-10}

Figure 5.4 contains a schematic representation of the model to be presented for the growth of the internal oxide platelets. The diagram depicts the internal oxides as parallel rectangular plates growing inward perpendicular to the external surface. The ends of the internal oxide plates have been assumed to be flat. Capillarity acting on the ends of the plates has been neglected; thus the absence of a Gibbs-Thompson equation in the model. The growth of the plates occurs by sweeping out a ribbon-volume of $dL \cdot Y \cdot t$ in an increment of time dt. One assumes no change in thickness of the plates "t" or spacing between the plates "s".

Oxygen is absorbed at the external surface with its concentration here being $N_o^{(S)}$ ($=4.7 \times 10^{-5}$ oxygen atom fraction)[20] and diffuses inward between the ZnO plates (interstitially) through the alloy to the reaction front. At the

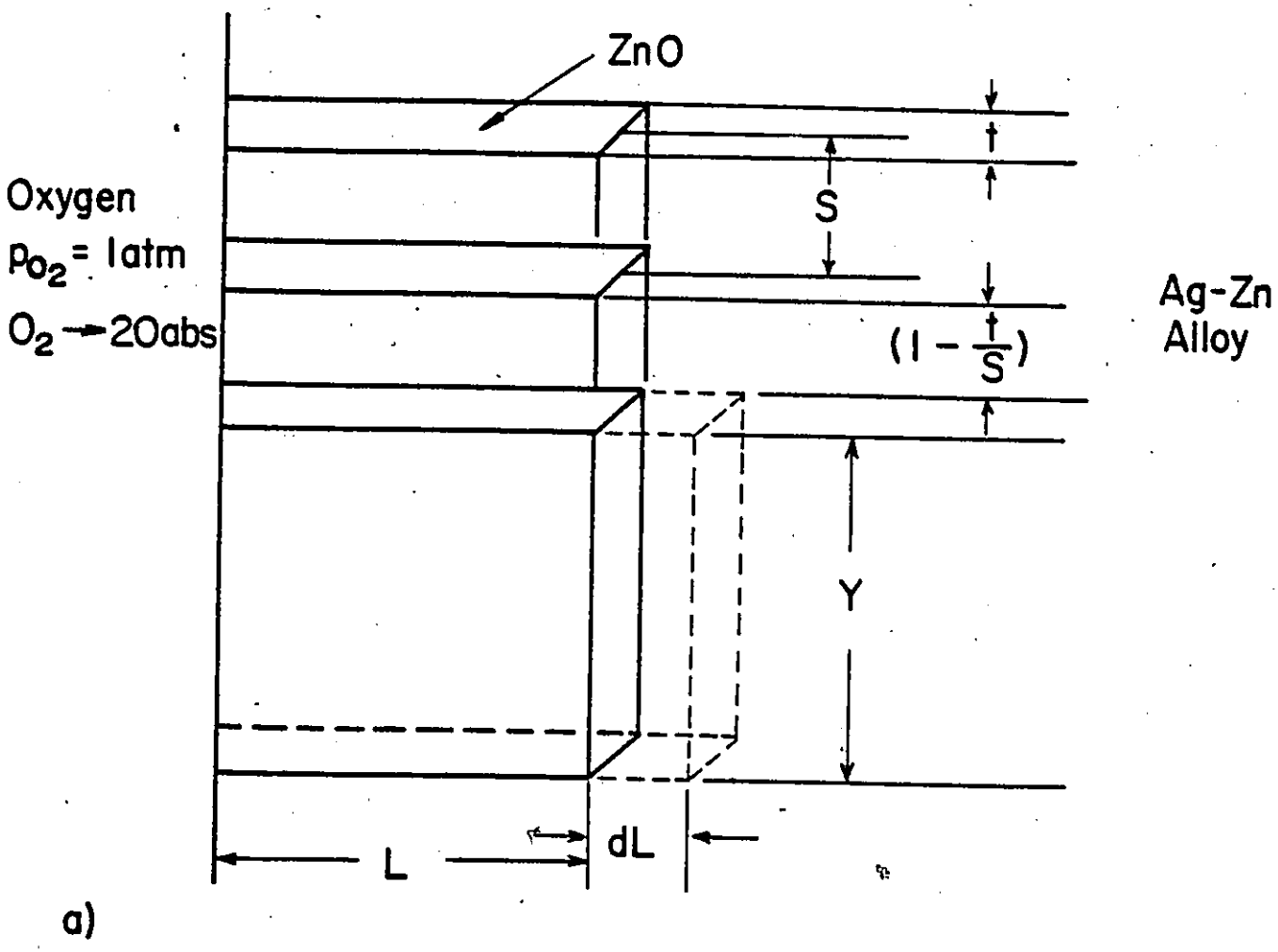

Figure 5.4 Model for Growth of Internal ZnO.

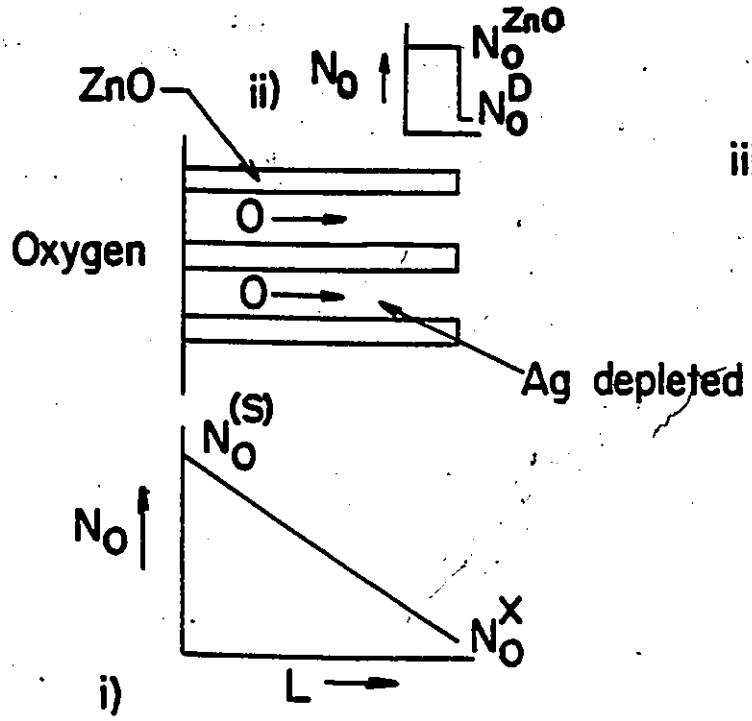

b) Oxygen concentrations

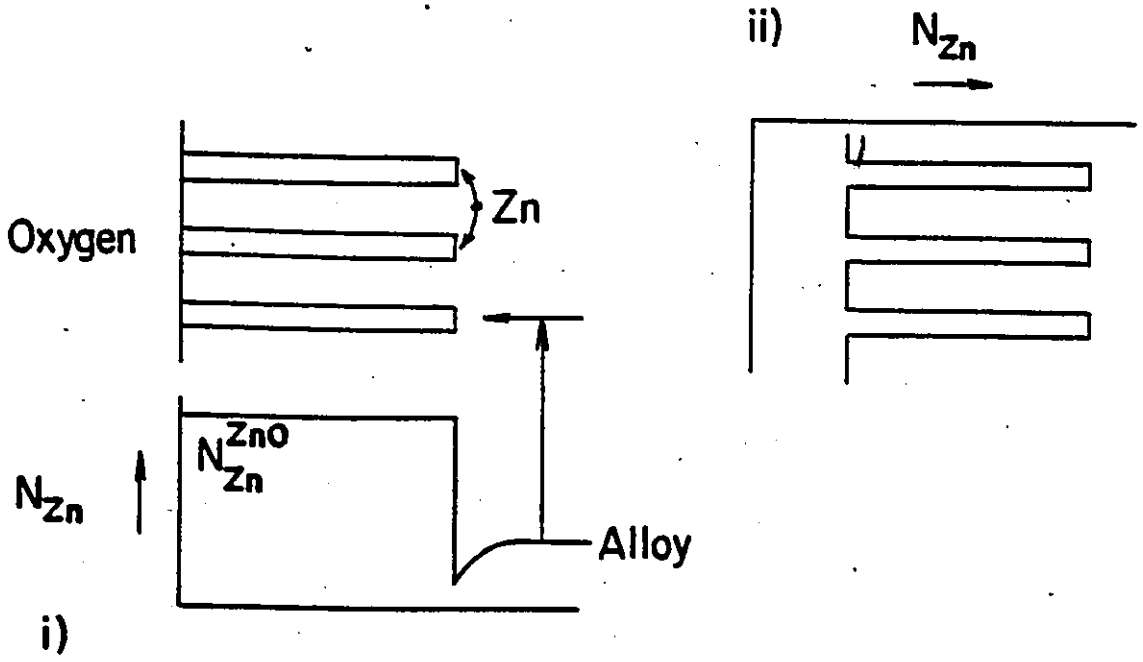

c) Zinc concentrations

Figure 5.4 (continued)

reaction front the oxygen concentration is some unknown value of N_o^x, next to the internal ZnO the oxygen concentration set by the ZnO dissociation pressure N_o^D ($=5.3\times10^{-26}$ atm, eqn. (5-4)). N_o^{ZnO} is the concentration of oxygen in ZnO which is .2 oxygen atom fraction. The concentration profiles for oxygen are given in Figure 5.4 (b) and are assumed to be linear. The concentration profiles for zinc are illustrated in Figure 5.4 (c). Here at the front the zinc diffuses sideways to form the platelets. The spacing of the platelets to a first approximation is determined by the time taken for zinc to diffuse sidewise from the alloy to the tip of the platelet for a given velocity of the internal oxidation front.

The internal precipitate plates formed in the 1.8 wt % Zn alloy grow independently from one another; thus the diffusion fields between the plates are weakly coupled. This is schematically shown in Figure 5.5 (a). While the plates formed in the Ag-7.5, 10.9 wt % Zn alloy are strongly coupled (see micrographs of plates in experimental results chapter) and is illustrated in Figure 5.5 (b)[60].

Since the growth of the plates is controlled by oxygen diffusion a flux balance for oxygen at the internal oxidation front may be written:

$$V\cdot(N_o^{ZnO} - N_o^x) = -D_o^{Ag}(N_o^x - N_o^{(S)}) \qquad (5\text{-}7)$$

corrections must be made to each side for the appropriate volume fractions for each phase.

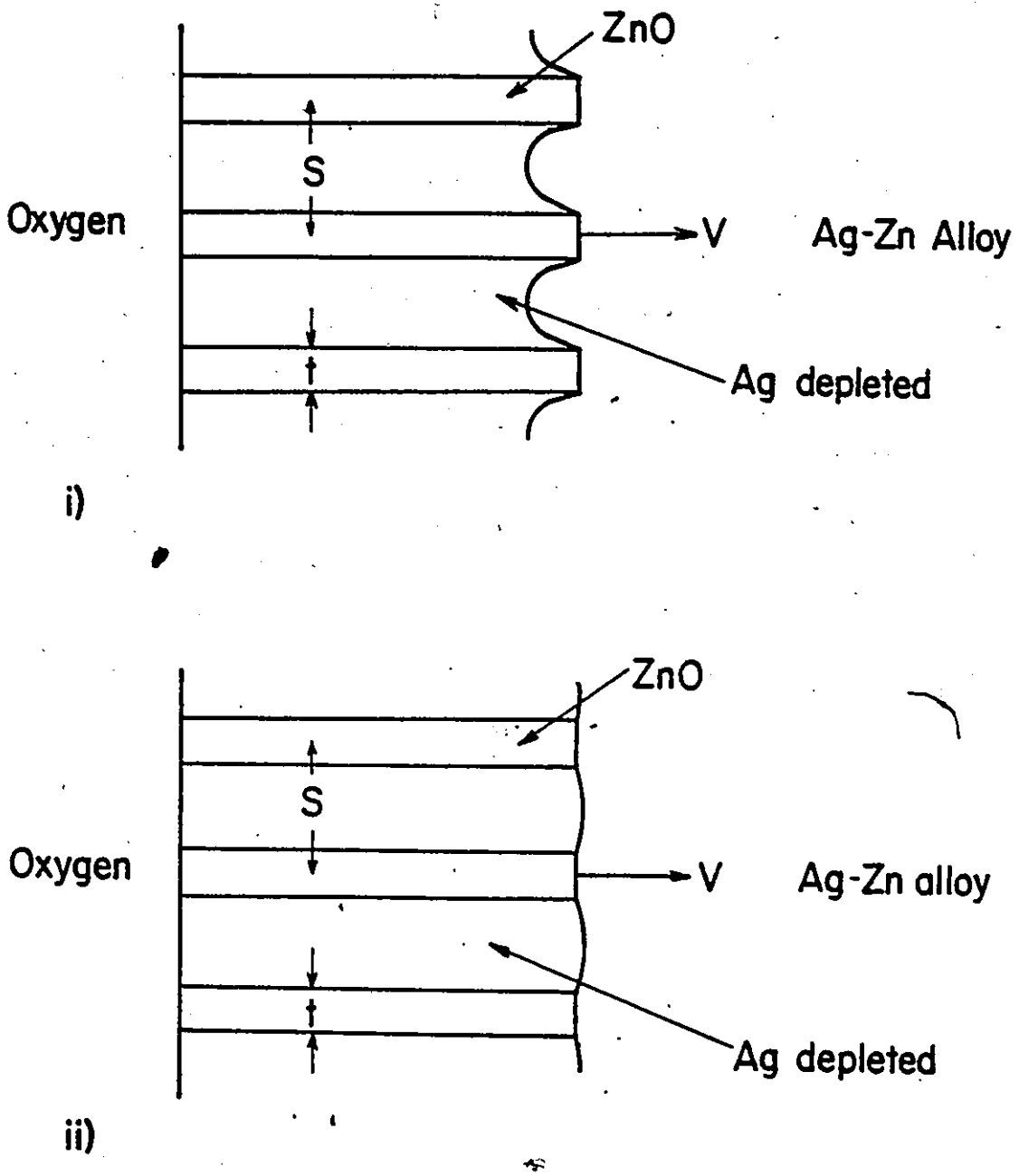

Figure 5.5 Diffusion Coupling

i) Ag-1.8 wt % Zn - Weak Diffusive Coupling.

ii) Ag-7.5, 10.9 wt % Zn - Strong Diffusive Coupling.

$$V \cdot (N_o^{ZnO} - N_o^x)\frac{t}{s} = D_o^{Ag} \frac{(N_o^{(S)} - N_o^x)}{L} (1 - \frac{t}{s}) \quad (61)$$

$$(5\text{-}8)$$

If $N_o^x << N_o^{ZnO}$ and $N_o^x << N_o^{(S)}$, then (5-8) may be simplified to:

$$V = \frac{D_o^{Ag} \cdot (N_o^S)}{L \; N_o^{ZnO}} (\frac{s}{t} - 1) \; . \quad (5\text{-}9)$$

Substitution of D_o^{Ag}, $N_o^{(S)}$ and N_o^{ZnO} one arrives at:

$$V = \frac{1.03 \times 10^{-9}}{L} (\frac{s}{t} - 1) \; cm^2/sec \; . \quad (5\text{-}10)$$

To test equation (5-10) for the velocity of the internal oxide plates a few assumptions must be made in order to use experimental results. The growth of the internal oxide colonies is assumed to be perpendicular and continuous from the external surface to the internal oxidation front. In reality the internal oxidation zone is made up of a series of colonies growing inward in a zig-zag fashion to the front. This allows L to be equated to the penetration of the internal oxidation zone. The above assumption is reasonable because oxygen diffusion at boundaries (where colonies meet) is greater (due to defects) by one or two orders of magnitude than in the alloy matrix. A comparison of velocities obtained from the kinetic curves, Figures 4.1, 4.2, 4.3 and those from equation (5-10) can be made, if one assumes the velocity of the internal oxidation front is approximately equal to the velocity of the plates at the same depth within the alloy. Substitution of the results from the experimental section, Table 4-2 and sections 4.2.2. ii), iii) into equation

(5-10) one arrives at Table 5-3.

The experimental error for the depth was determined from the error in making two micrometer measurements. The spacing and thickness errors are estimated from the error in actual measurement of these two parameters from the transverse photographs by a mm ruler and 10× lens. No error for surface inclination of the platelets has been taken into account. The error in the velocity obtained from the kinetic curves is based on the error in construction of X versus time curves and determining point velocities on these curves. From Table 5-3 one sees there is good agreement between the experimental velocity and that obtained by the model. As mentioned previously one can compare the spacing of the plates with the zinc diffusion distance as predicted from $(D_{Zn}^{Ag} \cdot t)^{1/2}$. Once again good agreement has been obtained and illustrates the zinc would have sufficient time to diffuse sidewise to the tip of the platelets. Thus, the proposed oxygen volume diffusion model, may be used to predict velocities of internal oxide platelets for Ag alloys containing less than 11 wt % Zn, undergoing oxidation in pure oxygen at 550°C.

Table 5-3

Comparison of Velocities Obtained from Experimental Kinetic Curves and the Oxygen Volume Diffusion Model

Alloy	Depth* cm	S** cm	t** cm	V_{graph}*** cm/sec	$V_{equation}$**** (cm/sec)
Ag-1.8 wt % Zn	.009	2.2×10^{-4}	5×10^{-5}	10×10^{-7}	4×10^{-7}
Ag-1.8 wt % Zn	.022	4.7×10^{-5}	3×10^{-6}	10×10^{-7}	7×10^{-7}
Ag-1.8 wt % Zn	.034	4.5×10^{-5}	5×10^{-6}	8×10^{-7}	2×10^{-7}
Ag-7.5 wt % Zn	.006	9.8×10^{-5}	2×10^{-5}	2×10^{-7}	7×10^{-7}
Ag-10.9 wt % Zn	.011	1.3×10^{-4}	3×10^{-5}	$.9\times10^{-7}$	3×10^{-7}

*error ±.002, **error ±20%, ***error ±10%, ****error ±1000%.

Table 5-4

Comparison of Platelet Spacing with that Predicted from Zinc Diffusion

Alloy	Depth cm	S/2 cm	$(D_{Zn}^{Ag} \cdot time)^{1/2}$ cm
Ag-1.8 wt % Zn	.009	1×10^{-4}	3×10^{-4}
Ag-1.8 wt % Zn	.022	2×10^{-5}	5×10^{-4}
Ag-1.8 wt % Zn	.034	2×10^{-5}	8×10^{-4}
Ag-7.5 wt % Zn	.006	5×10^{-5}	8×10^{-4}
Ag-10.9 wt % Zn	.011	1×10^{-4}	4×10^{-3}

5.3 Transition from Internal Oxidation to Continuous External Scale Formation

5.3.1 Introduction

The transition from internal oxidation to external scale formation in Ag-Zn alloys will be given from a phenomenological basis as well as a fundamental one. The phenomenological section is based on the observable morphological development of the internal ZnO and how this development affects the formation of continuous external ZnO. The fundamental argument is based on the Wagner[26] thermodynamic criteria given in 2.3.1, where the alloy content necessary for external oxidation is determined by equation (2-37). The Wagner criteria can also be placed into a ternary thermodynamic and diffusion formalism using Ag-Zn-O ternary isotherm. The placement of the diffusion paths on the Ag-Zn-O isotherm for the oxidation products produced in each alloy studied will also be given.

5.3.2 Morphological Development of Internal ZnO Leading to Continuous External ZnO

As the zinc content is increased in the alloys studied, Ag-1.8, 7.5, 10.9 and 12.9 wt % Zn, one obtains drastic changes in the morphology of the internal ZnO and the internal oxidation zone itself. The penetration depth of the internal oxidation zone decreases by a factor of 13 in these alloys for the same given time. The density of the internal ZnO in the internal oxidation zone has increased significantly from the Ag-1.8 to the 10.9 wt % Zn alloy (Figures 4.6, 4.12).

The thickness of the internal ZnO increased (Table 5-3), but more significant is the filling of the space between the plates from side branching and local thickening (Figures 4.6, 4.12). Thus less volume exists for oxygen to diffuse down to the internal oxidation front.

At the intersection of two colonies, for example, an inclined colony (Figure 5.2 ii)) contacting a colony growing perpendicular to the external surface (Figure (5.2 i)), the inclined colony is prevented from growing any further. The inclined colony sees ahead of it a wall of continuous ZnO. As one increases the Zn content the density and the thickness of internal ZnO in the internal oxidation zone increases greatly and thus an ever greater tendency for intersections to occur. The greater the intersections, the more the growth of the plates inward is impeded: The intersection areas provide local barriers to oxygen diffusion; hence upon reaching the barriers oxygen must find a new path to the front. As the number of intersections increase one begins to form regions of continuous ZnO inside the internal oxidation zone and these regions will spread laterally by joining each other.

Similar types of mechanisms for the transition from internal to external scale formation have been observed in Ni-Cr[67] and Ni-Al[68,69] alloys. Recently, Hindam has observed partially continuous internal Al_2O_3 film formed by impingements of favourably oriented Al_2O_3 rods[59].

In the 12.9 wt % Zn alloy one obtains both internal and external oxidation (Figure 4.18), where only external oxidation is present and adherent to the alloy, no internal oxidation is present. Where the scale is adherent to the alloy, oxygen is supplied to the alloy at the dissociation pressure of ZnO. Where the external oxide has blistered and cracked, oxygen is supplied at the oxidizing pressure of 1 atm and internal ZnO is formed in the alloy. But, the penetration of the internal ZnO formed here is much less than in Ag-10.9 wt % Zn (Figure A.3.2) because of the intersection effect. Finally, in the Ag-18.7 wt % Zn alloy only an adherent external ZnO layer is formed, with no internal oxidation.

5.3.3 The Wagner Criteria for the Transition from Internal to External Oxidation

If one assumes the model given in Figure 2.3 (a) is valid for the oxidation case here, then equation (2-37) may be used to predict the concentration of zinc necessary to form a continuous external ZnO scale on a Ag-Zn alloy.

$$N_{Zn}^{o} \geq \frac{F(\mu) + \frac{1}{\nu}\left(\frac{D_o^{Ag}}{D_{AgZn}}\right)^{1/2} \mu\pi^{1/2}}{1 + \frac{1}{\nu}\left(\frac{D_o^{Ag}}{D_{AgZn}}\right)^{1/2} u\pi^{1/2}} \qquad (5\text{-}11)$$

$$F(\mu) = (\pi)^{1/2} u \exp(u)^2 \operatorname{erfc}(u) \qquad (2\text{-}30)$$

$$\mu = \left(\frac{k}{2D_{Ag\cdot Zn}}\right)^{1/2} \qquad (5\text{-}12)$$

where k is corrosion constant for Ag-18.7 wt % Zn from Figure 4.20 and $D_{Ag\cdot Zn}$ [70] is the interdiffusion coefficient for the alloy.

$$\mu = \left(\frac{1.62\times10^{-12}}{2\times4\times10^{-10}}\right)^{1/2} = 4.5\times10^{-2} \qquad (5\text{-}13)$$

$$F(\mu) = (1.77)(4.5\times10^{-2})\exp(4.5\times10^{-2})\operatorname{erfc}(4.5\times10^{-2}) = 7.6\times10^{-2} .$$

Upon substitution of the paramaters, we arrive at:

$$N^{o}_{Zn} \geq \frac{7.6\times10^{-2} + \frac{1}{1}\left(\frac{4.39\times10^{-6}}{4\times10^{-10}}\right)^{1/2}(4.5\times10^{-2})(1.77)}{1 + \frac{1}{1}\left(\frac{4.39\times10^{-6}}{4\times10^{-10}}\right)^{1/2}(4.5\times10^{-2})(1.77)}$$

$$\geq \frac{7.6\ 10^{-2} + 8.34}{1 + 8.34}$$

$$\geq .90 \text{ atom fraction} .$$

The calculated result of .90 atom fraction for the critical concentration of zinc required to form a protective scale of ZnO differs greatly from the experimental result of .28 atom fraction. The Wagner criterion is based on a simple ideal model where no ternary interactions were assumed to exist. But if ternary interactions did exist they would affect the critical concentration of zinc required to maintain a protective external ZnO scale. This point is illustrated

in Figures 5.6 (a), (b), where it is shown that a large negative Wagner interaction parameter of oxygen for the alloying element decreases the critical alloy content necessary for exclusive external oxidation. To get an estimation of the interaction parameter of oxygen for zinc, assume the experimental critical concentration .28 is correct, and substitute it and the other parameters required into equation (2-65).

$$\varepsilon_o^{Zn}(N_{Zn}^{o*})^2 + \{\frac{1-F(\mu)}{F(\mu)}\left[1+\frac{u}{\nu}\left(\frac{\pi D_{oo}}{D_{ZnZn}}\right)^{1/2}\right] - \varepsilon_o^{Zn}[1+F(\mu)]\}(N_{Zn}^{o*})$$

$$+\{\varepsilon_{Zn}^{o}F(\mu) - [1-F(\mu)] - \frac{u}{\nu}\left(\frac{\pi D_{oo}}{D_{ZnZn}}\right)^{1/2}\frac{1-F(\mu)}{F(\mu)}\} = 0 \quad . \quad (5\text{-}14)$$

$N_{Zn}^{o*} = .28$ atom fraction, $F(\mu) = 7.6\times10^{-2}$, $u = 4.5\times10^{-2}$, $\nu=1$

$D_{oo} \cong D_o^{Ag} = 4.39\times10^{-6}$ cm^2/sec, $D_{ZnZn} \cong D_{AgZn} = 4\times10^{-10}$ cm^2/sec

$\varepsilon_o^{Zn} = \varepsilon_{Zn}^{o}$.

Substituting into (5-14), one obtains a value of -500 for ε_o^{Zn}. Figure 5.6 (b) is given for $D_o^{Ag}/D_{ZnZn} = 100$ but for this system $D_o^{Ag}/D_{ZnZn} = 10^4$. This has the effect of shifting k/D_{AA} curves upward as seen from Figure 5.6 (a). This shift upward for $k/D_{ZnZn} = 4\times10^{-3}$ would be from a critical atom fraction of .3 to .8 for no interaction and .07 to .3 for $\varepsilon_o^{Zn} = -500$. Thus an interaction parameter of $\varepsilon_o^{Zn} = -500$ plus values for $k/D_{ZnZn} = 4\times10^{-3}$ and $D_o^{Ag}/D_{ZnZn} = 10^4$ predict the critical atom fraction of zinc to be between .25 and .30

Figure 5.6

Effect of ε_o^{Zr} on the transition (where A=B, to keep terminology same as Ch. 2).

a) The critical atom fraction of A in the alloy, N_A^o, for exclusive external oxidation as a function of k/D_{AA} and D_{oo}/D_{AA}: no interaction.

b) The critical atom fraction of A in the alloy, N_A^{o*}, for exclusive external oxidation as a function of k/D_{AA} and the interaction parameter $\varepsilon_o^A \cdot D_{oo}/D_{AA} = 100$. (Ref. 26).

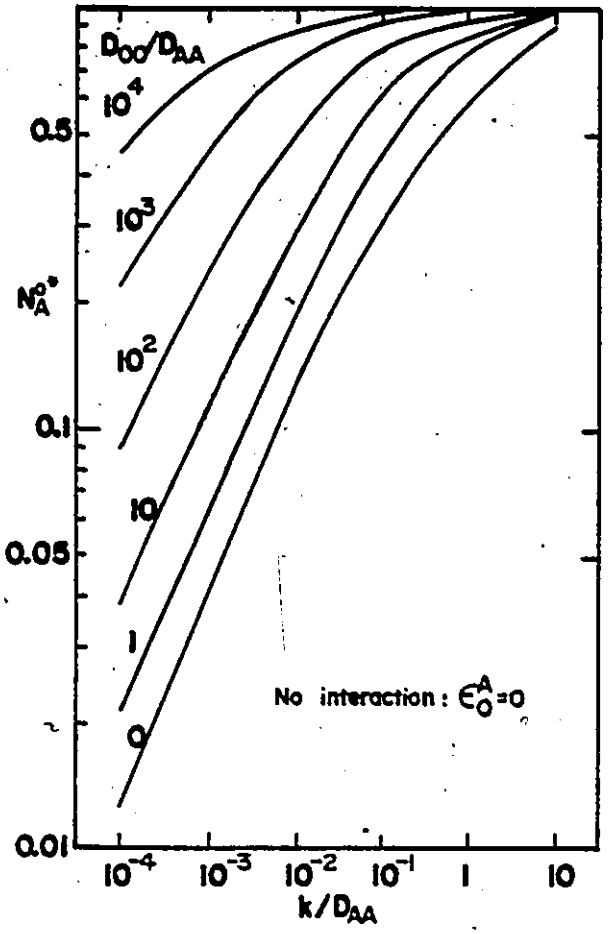
D_{00}/D_{AA}
10^4
10^3
10^2
10
1
0
No interaction : $\epsilon_0^A=0$
N_A^{0*}
0.5
0.1
0.05
0.01
10^{-4}
10^{-3}
10^{-2}
10^{-1}
1
10
k/D_{AA}

a)

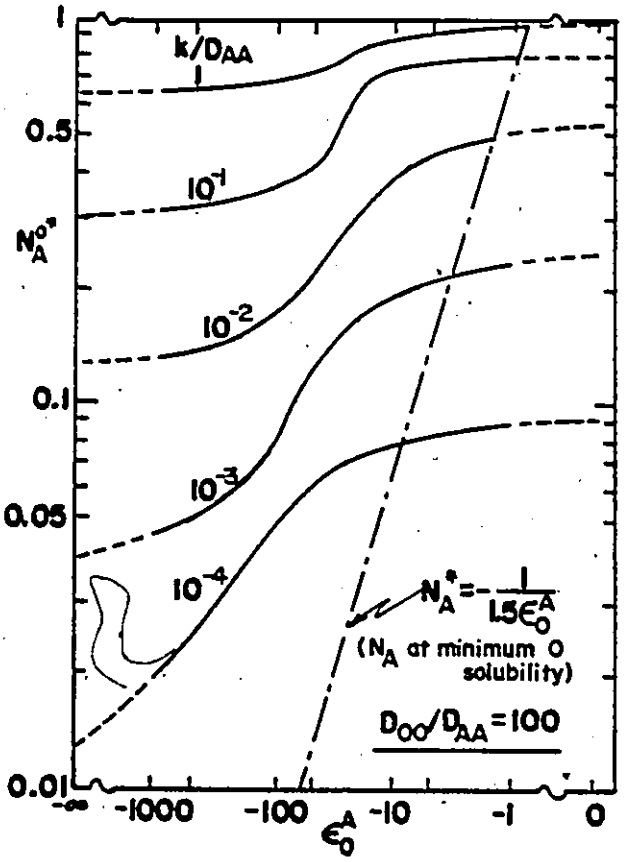
k/D_{AA}
1
10^{-1}
10^{-2}
10^{-3}
10^{-4}
$N_A^* = -\frac{1}{1.5\epsilon_0^A}$
(N_A at minimum 0 solubility)
$D_{00}/D_{AA}=100$
N_A^{0*}
1
0.5
0.1
0.05
0.01
$-\infty$
-1000
-100
-10
-1
0
ϵ_0^A

b)

which agrees well with the experimental results of .28.

5.3.4 Diffusion Paths for the Oxidation Products Produced

This short section deals with the "diffusion path concept"[71,72,73,74] which is used to interpret the steady state oxide scale morphologies formed on the different alloys (sec. 4.2.2 through 4.4.2). The proposed "virtual diffusion paths" have been placed on the Ag-Zn-O phase diagram (Figure 5.1) for the scale morphologies obtained in this study to give Figure 5.7. Point F has been placed in its approximate position on the ternary phase diagram by extrapolation of the oxygen activity curve, and the tie lines from the oxygen and ZnO phase fields. The extrapolation was necessary to propose a path for the Ag=1.8 wt % Zn alloy. The diffusion paths $a_1a_2a_3a_4$, $b_1b_2b_3b_4b_5b_6$, $c_1c_2c_3c_4c_5c_6$, $d_1d_2d_3d_4d_5d_6$, and $e_1e_2e_3e_4$, on Figure 5.7 correspond to the observed morphologies in Ag-1.8 wt % Zn, Ag-7.5 wt % Zn, Ag-10.9 wt % Zn, Ag-12.9 wt % Zn, and Ag-18.7 wt % Zn alloys respectively.

5.4 Growth of Protective ZnO Scale

5.4.1 Introduction

This final section deals with the development of the external ZnO scale on the Ag-1.8, 7.5, 10.9, 12.9 and 18.7 wt % Zn alloys. Where a thick adherent external scale is formed, discussion will concentrate on the mobilities of zinc by point defect transport in zinc oxide and application of Wagner[75] scaling theory to the growth of the protective

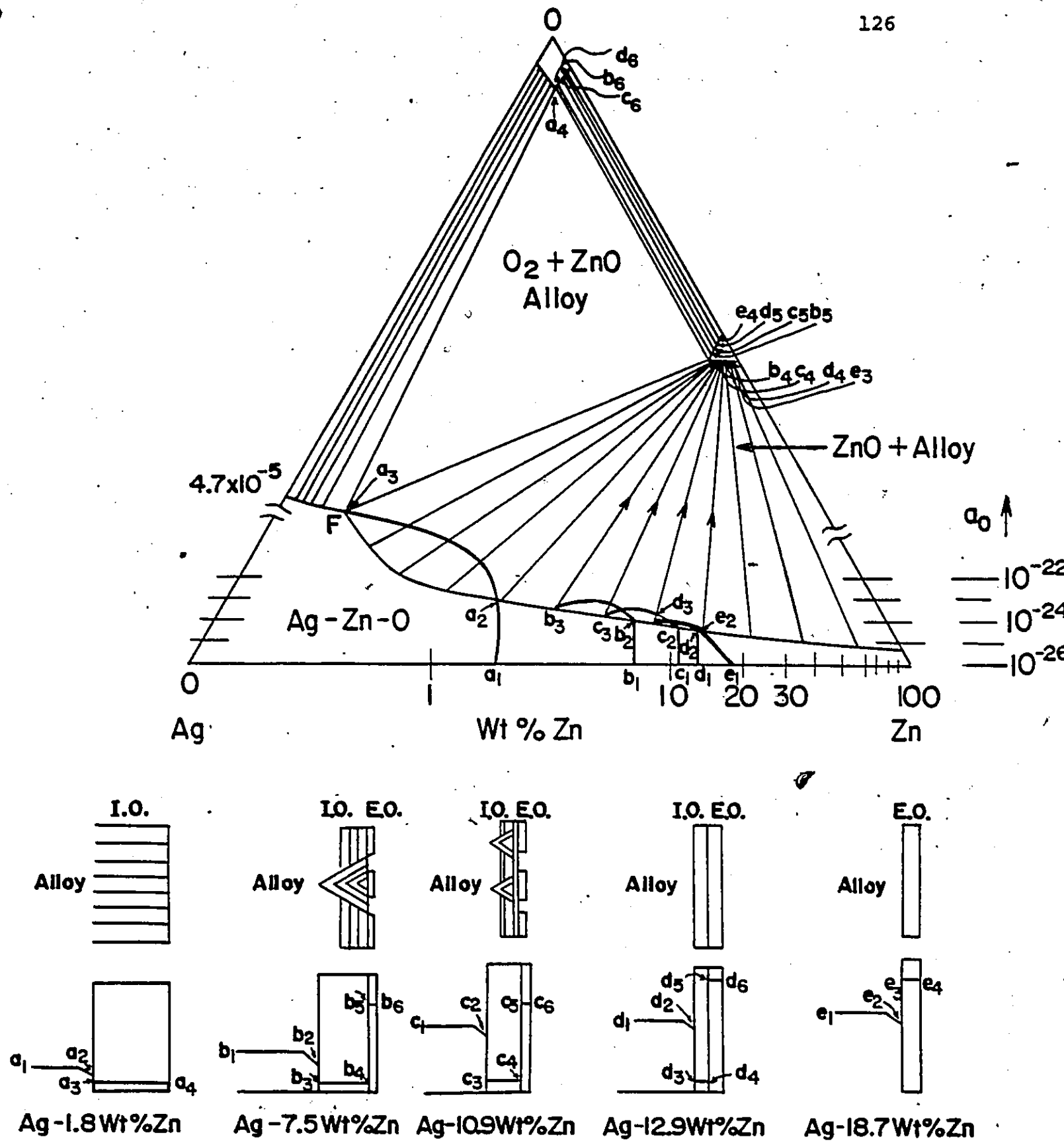

Figure 5.7 Diffusion Paths for the Oxidation Products Produced in the Alloys.

external ZnO in Ag-18.7 wt % Zn.

5.4.2 Development of the External Scale

5.4.2 i) Ag-1.8, 7.5 and 10.9 wt % Zn

When one of these alloys is introduced into the hot zone of the furnace (set at 550°C, P_{O_2} = 1 atm), oxygen is absorbed on the surface of the sample, and site exchange of oxygen and zinc occurs rapidly to form a few layers of oxide. In these alloys the site exchange[76] occurs in the valley regions of Figures 4.13, 4.14 and 4.15 until a critical size is reached, where upon nucleation of ZnO occurs. These nuclei should show some "Epitaxial"[77] relationship with the metal surface. At the present time no "epitaxial" relationship has been determined for hexagonal-ZnO growing on Ag-Zn alloys. Takahashi[78] and Mihama have determined that hexagonal-ZnO forms on α-brass metals according to:

(001) ZnO // (001) α-brass

[110] ZnO // [1$\bar{1}$0] or [110] α-brass .

The similarity between the Ag-Zn and Cu-Zn systems would probably mean a similar "epitaxial" relationship exists between hexagonal ZnO on Ag-Zn alloys.

The nuclei formed on the surface grow sidewise across the surface and outward from the surface as the time of oxidation increases up to 10 hours. The ZnO grows into

a very porous oxide layer (top-view) which surrounds the bare regions (hills) on the alloy surface (refer to Figures 4.13, 4.14 and 4.15 and Tables 4-3, 4-4 and 4-5). The porosity of the oxide and the bare (hills) alloy surface provide easy paths for oxygen to diffuse into the alloy. Complete coverage of the external surfaces by ZnO was not observed in any of the three alloys up to the 10 hour oxidation time studied.

5.4.2 ii) Ag-12.9 wt % Zn

For this alloy only cross-sections were examined under optical and scanning electron microscopes. The external oxide formed on this alloy, was observed to be non-uniform in thickness, non-adherent, non-protective and damaged. The external ZnO did not provide protection for the alloy due to the zinc content not being sufficient to cuase the transition to external oxidation and due to the exfoliation of the scale. The Pilling[79] and Bedworth rule predicts an external scale composed of ZnO would be protective because the ratio of the volume of ZnO to metal is 1.44[80]. This large volume difference would lead to the existence of interfacial strains which produce stresses in the oxide layer. These stresses lead to lifting and peeling of the external scale (4-18 (b), where the scale may rupture (Figure 4.18 (C)) or remain intact. The theoretical[81] treatment involves the elastic properties of the ZnO as well as the plastic properties of the Ag-Zn alloy.

Stresses may be relieved by primary slip, thus dislocations generated at the surface as slip steps. Volume changes also occur upon cooling the alloys because of the difference in thermal expansion coefficients of alloy and oxide. The external oxide itself is composed of a continuous thick layer, upon which grows needles outward. This topic will be expanded in the next section.

5.4.2 iii) Ag-18.7 wt.% Zn

Upon introducing samples of the above alloy into the reaction zone, oxygen is absorbed on the surface of the alloy, and again nucleation of ZnO occurs across the surface, and these nuclei should show some "epitaxial" relationship with the alloy surface, mentioned previously. These nuclei grow rapidly sidewise across the surface and outward from the surface to form a continuous film. The growth of the oxide film would follow the logarithmic law[82,83,84] up to 1000 Å in thickness. Upon reaching a thickness of 5000 Å and greater the Wagner[75] parabolic law will be valid.

The external scale was found to be composed of a continuous oxide layer with whiskers growing outward from within this layer. Figure 4.22 (a), (b) shows the surface covered by a continuous greyish oxide layer, and this oxide is observed to be rather porous and hilly as seen in Figures 4.22 (c), (d) from a top-view. But, in cross-section the continuous oxide layer (Figures 4.21 (a), (d)) is shown to be very compact and dense. Figures 4.22 (c), (d) show the

whiskers at their early stages of development, while Figures 4.22 (c), (f) and (g) illustrate the "crystal needle forests"[85] obtained after long periods of oxidation. The growth of whiskers on ZnO has been observed by R. W. Lucas[84] and G. Pfefferkorn[85]. No theoretical treatment for the mechanism by which the ZnO whiskers grow has been proposed yet, but models have been put forth for the growth of whiskers of other types of oxides, for example, Fe_2O_3[86,87,88,89,90,91] on iron alloys. The length distribution[92] of the growing oxide needles can be expressed by:

$$\frac{dN}{Nd\lambda} = K \exp(-K\lambda) \qquad (5\text{-}15)$$

where λ is the needle length and K decreases with increasing reaction time. The whiskers do not influence the oxidation rate of the oxide layer because the transport of matter through the compact oxide layer is rate determining.

Identification of the external scale has been made by two techniques, X-ray energy dispersive analysis and X-ray diffraction (Debye-Scherrer powder method). The X-ray energy dispersive results indicate large amounts of zinc present in the compact oxide layer as well as in the whiskers (Sec. 4.4.2-4.4.3). The Debye-Scherrer technique identified the crystalline structure of the whole external oxide as hexagonal-ZnO (zincite), (Sec. 4.4.4).

Exclusive external oxidation has also been observed to occur at 20 wt % Zn in Cu-Zn alloys[93,94].

5.4.3 Transport of Zinc in ZnO

Classically, ZnO is classified as a metal excess[95] (n-type) semiconductor and mass transport through the oxide is achieved by Zn ion interstitial movement. But in reality the details of the defect structure are complicated and as of yet not well understood. The excess cations and an equivalent number of electrons are located on interstitial lattice sites. When an alloy of Ag-Zn with a ZnO layer growing on the surface is exposed to oxygen, oxygen absorption at the surface effectively creates a negative component. Thus the absorbed oxygen would bring about a migration of divalent zinc ions and electrons from the original lattices, in order to form new zinc oxide at the surface according to:

$$2Zn_i^{++} + 4e^- + (O_2) = 2ZnO \qquad (5\text{-}16)$$

where the subscript i indicates interstitial ions and e^- is the excess electron. Mollwo[97] and Stoeckmann have also shown that a univalent zinc ion is possible as a means of transport:

$$2Zn_i^{+} + 2e^- + (O_2) = 2\ ZnO\ . \qquad (5\text{-}17)$$

If the ideal mass action law is applied, the following relationship for electrical conductives should apply:

$$K = \text{const.} \cdot [P(O_2)]^{-1.6} \text{ or } K = \text{const.} \cdot [P(O_2)]^{-1/4} \qquad (5\text{-}18\ a,b)$$

These relationships have been found to lie very close to those

obtained by various workers[97,98,99,100,101].

Thus the growth of the external ZnO on the Ag-Zn alloys occurs by the outward diffusion from the alloy of Zn_i^{++} or Zn_i^{+} through the oxide layer to its surface to meet oxygen where it reacts to form ZnO.

5.4.4 Continuous Scale Model for the External Scale

Figure 4.20 indicates parabolic kinetics for the growth of the external scale on the Ag-18.7 wt % Zn. Parabolic kinetics has been observed for the growth of external ZnO on Zn(s)[84], Zn(ℓ)[80,90], and Cu-Zn[93,94] alloys for similar oxidizing conditions.

Wagner has developed a theoretical treatment for the parabolic growth of scales, based on ambipolar diffusion of the reactants, describing the occurring reaction in terms of migration of point defects. The driving force for the diffusion of the reactants in this case Zn_i^{++} or Zn_i^{+} and electrons outward, $O^{=}$ inward is the electrochemical potential gradient existing across the oxide layer. The general form of the parabolic rate constant from the Wagner[75] theory is given by:

$$Kr = \bar{c}_2 \int_{a_o'}^{a_o''} \left(\frac{Z_1}{Z_2} D_M + D_O\right) d\ell n a_O \qquad (5\text{-}19)$$

where the integration refers to the oxygen chemical potential from the inner to outer external scale interfaces, $\bar{c}_2$ is the

average composition in equivalents, D_M and D_O are self-diffusion coefficients for metal and oxygen, and Z_1 and Z_2 are the number of equivalents of metal and oxygen. At the present time it is not possible to calculate the parabolic rate constant for ZnO, from equation (5-19) because of the lack of independent mass transport[83] measurements in ZnO, for example the zinc ion conductivity[102].

The parabolic rate constant determined from Figure 4.20 for the growth of ZnO on Ag-18.7 wt % Zn is 1.62×10^{-12} cm^2/sec. No parabolic rate constants are available in the literature for any Ag-Zn alloys. But, Cope[103] has determined the parabolic rate constants for the oxidation of liquid zinc, Kr = 5.4×10^{-12} cm^2/sec at 550°C and .25 atm. oxygen. These two results are similar, because transport[104] through ZnO is controlled by the diffusion of defects associated with excess zinc in both the liquid zinc and solid Ag-Zn alloy oxidation.

CHAPTER 6

CONCLUSIONS

1. When Ag-Zn alloys of less than 11 wt % Zn are exposed to oxygen at 550°C, internal precipitation of ZnO occurs.
2. The internal precipitates of ZnO grow inward, according to parabolic kinetics, in the form of platelike colonies perpendicular to the external surface.
3. The internal precipitates were found to form by two distinct types of morphology in cross-section, one "arrowhead" and the other "apparent orientational Liesegang".
4. The velocity of the internal zinc oxides may be predicted using the oxygen volume diffusion model proposed.
5. The transition to external scale formation in the Ag-Zn alloys occurs by means of thickening of the internal oxidation zone, thus providing less volume for oxygen to diffuse to the internal oxidation front.
6. The Wagner binary criteria fails to predict the correct concentration for the transition because

of the probable existence of a large negative Wagner interaction parameter.

7. An exclusive external scale of ZnO (zincite) is formed on an alloy of Ag-18.7 wt % Zn. The external scale obeys parabolic kinetics and is composed of a continuous compact layer from which whiskers grow outward from within the compact layer.

APPENDIX 1

(a) Solutions for concentration profiles of oxygen and alloying element B with a combination of external and internal scales (Chapter 2 (i)(c)):

$$\frac{\partial N_o}{\partial t} = D_o \frac{\partial^2 N_o}{\partial^2 x} \qquad \begin{matrix} bt \leq x \leq bt + \zeta - X \\ o \leq t' \leq \infty \end{matrix} \qquad \text{(A-1-1)}$$

where t = time, t' - time after steady-state established. The boundary conditions for A-1-1 are:

$$N_o(bt,t') = N_o^D \qquad \text{(A-1-2)}$$

$$N_o(bt+\zeta-x,t') = 0 \qquad \text{(A-1-3)}$$

changing variables such that

$$\omega = x - bt \qquad \text{(A-1-4)}$$

$$t = t' \qquad \text{(A-1-5)}$$

Now $N_o(x,t)$ becomes $N_o(\omega,t')$ and equation (A-1-1) is transformed to:

$$\frac{\partial \bar{N}_o}{\partial t'} = D_o \frac{\partial^2 N_o}{\partial^2 w} + b \frac{\partial \bar{N}_o}{\partial \omega} \qquad \text{(A-1-6)}$$

valid for $0 \leq \omega \leq \zeta - X$, $0 < t' < \infty$.

The boundary conditions for (A-1-1) are:

$$\bar{N}_o(o,t') = N_o^D \qquad \text{(A-1-7)}$$

$$\bar{N}_o(\zeta-X,t') = 0 \ . \qquad \text{(A-1-8)}$$

Solving (A-1-6), (A-1-7) and (A-1-8):

$$N_o(x,t) = N_o^D\{\frac{\exp[-\frac{b}{D_o}(x-bt)]-\exp(-\frac{b}{D_o}(\zeta-X)]}{1-\exp[-\frac{b}{D_o}(\zeta-X)]}\}. \qquad \text{(A-1-9)}$$

Now for solute in internal oxidation zone:

$$\frac{\partial N_B}{\partial t} = D_B \frac{\partial^2 N_B}{\partial^2 x} \ , \quad \begin{array}{l} bt+\zeta-X \leq x \leq \infty \\ o \leq t' \leq \infty \\ D_B \neq D_B(x). \end{array}$$

where the boundary conditions are:

$$N_B(bt+\zeta-X,t') = 0 \qquad \text{(A-1-11)}$$

$$N_B(\infty,t') = N_B^o \ . \qquad \text{(A-1-12)}$$

Proceeding as with oxygen one can deduce:

$$N_B(x,t') = N_B^o[1-\exp[-\frac{b}{D_B}(x-bt-(\zeta-X))] \qquad \text{(A-1-13)}$$

(23)

(b) Solutions for evaluated unknown parameters N_o, N_B, N_o^* and N_B^* for Kahlweit's[45] model. We commence with:

$$Z(x) \approx (\Delta x)^{-3} = \left(\frac{x}{\Delta x}\right)^3 \left(\frac{1}{x^3}\right) . \qquad \text{(A-1-1)}$$

In Figure 2.9 at x, the concentration product reaches a maximum $N_o(x) \cdot N_b(x)$. Thus:

$$\frac{\partial}{\partial x} (N_o \cdot N_B)_x = 0 = \left.\frac{\partial N_o}{\partial x}\right|_x N_B(x) + N_o(x) \left.\frac{\partial N_B}{\partial x}\right|_x . \qquad \text{(A-1-2)}$$

At instant of nucleation, $N_o(x)$ and $N_B(x)$ are equal to N_o^* and N_B^* respectively. We find:

$$- N_o^* / \left(\frac{\partial N_o}{\partial x}\right)_x = N_B^* / \left(\frac{\partial N_B}{\partial x}\right)_x \qquad \text{(A-1-3)}$$

$$\left(\frac{\partial N_B}{\partial x}\right)_x = 2\theta\gamma^2 \frac{N_B^o - N_B^*}{x} \qquad \text{(A-1-4)}$$

$$\left(\frac{\partial N^o_o}{\partial x}\right)_{x'} = - N_o^o / x'$$

For $\partial N_o / \partial x$, one has to insert the gradient of oxygen which is formed at the right-hand side x', after $N_B(x')$ has decreased to saturation value N_B'. This gradient is built up by excess of oxygen at x', minus the amount of N_B diffusing to x' from the right-hand side:

$$-D_o \left.\frac{\partial N_o}{\partial x}\right|_{\lim_{\varepsilon=0} x'+\varepsilon} = -D_o \left.\frac{\partial N_o}{\partial x}\right|_{\lim_{\varepsilon=0} x'-\varepsilon} - D_B \left.\frac{\partial N_B}{\partial x}\right|_{\lim_{\varepsilon=0} x'+\varepsilon} \qquad \text{(A-1-6)}$$

$$N_B(x) = N_B^* + \left.\frac{\partial N_B}{\partial x}\right|_x (x-X) \text{ for } x' \leq x \leq X \qquad \text{(A-1-7)}$$

$$\frac{N_B^{*}-N_B'}{\Delta x} = \frac{\partial N_B}{\partial x}\bigg|_{\substack{\lim x'+\varepsilon \\ \varepsilon=0}} = \frac{\partial N_B}{\partial x}\bigg|_{x} = \frac{D_o}{D_B}\,\frac{N_B^{o}-N_B^{*}}{N_B^{o}-N_B'}\,\frac{N_o^{o}}{x} \quad . \qquad \text{(A-1-8)}$$

Put (A-1-5) and (A-1-8) into (A-1-6).

$$-D_o \frac{\partial N_o}{\partial x}\bigg|_{\substack{\lim x'+\varepsilon \\ \varepsilon=0}} = j_o = D_o\,\frac{N_B^{*}-N_B'}{N_B^{o}-N_B'}\,\frac{N_o^{o}}{x} \qquad \text{(A-1-9)}$$

For gradient of oxygen at x:

$$\frac{\partial j_o}{\partial t} = D_o\,\frac{\partial^2 j_o}{\partial^2 x} \qquad \text{(A-1-10)}$$

With the boundary conditions

$$t = t': \; j_o = 0 \quad \text{for } x > x' \qquad \text{(A-1-11)}$$

$$t \leq t': \; j_o = j_o^{o} \text{ for } x = x' \qquad \text{(A-1-12)}$$

of which the solution is:

$$j_o(x,t-t') = j_o^{o}\,\mathrm{erfc}\{\frac{\Delta x}{2D_o^{1/2}(t-t')^{1/2}}\} \quad . \qquad \text{(A-1-13)}$$

For t-t' one inserts between two subsequent precipitations:

$$t-t' = \frac{N_B^{o}-N_B'}{D_o N_o^{o}}\,\Delta x \cdot x \quad . \qquad \text{(A-1-14)}$$

Put (A-1-14) into (A-1-13)

$$\frac{\Delta x}{2D_o^{1/2}(t-t')^{1/2}} = \frac{1}{2}\cdot\left(\frac{N_o^{o}\,\Delta x}{(N_B^{o}-N_B')x}\right)^{1/2} \qquad \text{(A-1-15)}$$

If the argument of error function is small compared to unity, thus:

$$\left.\frac{\partial N_o}{\partial x}\right|_{\substack{\lim \\ \varepsilon=0}} x'+\varepsilon \approx \left.\frac{\partial N_o}{\partial x}\right|_x = -\frac{1}{D_o} j_o^o = -\frac{N_B^*-N_B'}{N_B^o-N_B'} \frac{N_o^o}{x} \quad . \qquad \text{(A-1-16)}$$

Inserting (A-1-8) and (A-1-16) into (A-1-13) find first equations

$$\frac{x}{x} = \frac{N_o^o}{N_o^*} \frac{N_B^*}{N_B^o-N_B'} \quad . \qquad \text{(A-1-17)}$$

Second equation from (A-1-8) yields:

$$\frac{x}{\Delta x} = \frac{D_o}{D_B} N_o^o \frac{N_B^o-N_B^*}{(N_B^o-N_B')(N_B^*-N_B')} \quad . \qquad \text{(A-1-18)}$$

Analogy to (A-1-7) for N_o:

$$N_o(x) = N_o' + \left.\frac{\partial N_o}{\partial x}\right|_{\substack{\lim \\ \varepsilon=0}} x'+\varepsilon (x-x') \quad \text{for } x' \leq x \leq X \quad . \qquad \text{(A-1-19)}$$

From (A-1-19), by use of (A-1-16) again, a third equation for $x/\Delta x$ is obtained:

$$\frac{x}{\Delta x} = \frac{N_o^o}{N_o'-N_o^*} \frac{N_B^*-N_B'}{N_B^o-N_B'} \qquad \text{(A-1-20)}$$

$$N_o' \cdot N_B' = Ksp \quad . \qquad \text{(A-1-21)}$$

Now four equations have been found, (A-1-17), (A-1-18), (A-1-20) and (A-1-21). Thus, the evaluation of the four unknown quantites N_o', N_B', N_o^*, and N_B^* from the experimentally determined number of particles per unit volume with known N_o^o, N_B^o, Ksp and D_o/D_B.

$$\frac{1}{N_o^o}\frac{x}{\Delta x} = \frac{1}{N_o^*}\frac{N_B^*}{N_B^o - N_B'} = \frac{1}{N_o' - N_o^*}\frac{N_B^* - N_B'}{N_o^o - N_B'} =$$

$$\frac{D_o}{D_B}\frac{N_B^o - N_B^*}{(N_B^o - N_B')(N_B^* - N_B')} \quad (45) \qquad \text{(A-1-22)}$$

APPENDIX 2

398

Ag-Zn

TABLE 2

Partial Molar Quantities for Solid Alloys at 873°K

A. Ag Component $Ag_{(s)} = Ag(\text{in alloy})_{(s)}$

x_{Ag}	Phase	a_{Ag}	γ_{Ag}	$\Delta\bar{F}_{Ag}$	$\Delta\bar{F}^{xs}_{Ag}$	$\Delta\bar{H}_{Ag}$	$\Delta\bar{S}_{Ag}$	$\Delta\bar{S}^{xs}_{Ag}$
1.00	α	1.00	1.00	0	0	0	0.00	0.00
0.90		0.91	1.01	- 170	10	(- 100)	(0.1)	(-0.1)
0.80		0.80	1.00	- 400	- 10	(- 200)	(0.2)	(-0.2)
0.70		0.60	0.86	- 890	- 270	(- 210)	(0.8)	(0.1)
0.652*		0.50	0.76	-1210	- 470	(- 210)	(1.2)	(0.3)
0.600*	β	0.50	0.83	-1210	- 330	(100)	(1.5)	(0.5)
0.50		0.35 (±.08)	0.57 (±.16)	-2170 (±500)	- 970 (±500)	(-1000)	(1.4)	(0.0)
0.442*		0.18	0.41	-2960	-1540	(-1800)	(1.3)	(-0.3)
0.402*	γ	0.18	0.45	-2960	-1380	(-1500)	(1.6)	(-0.2)
0.388		0.15	0.39	-3290	-1640	(-2000)	(1.4)	(-0.5)
0.360*		0.10	0.28	-3980	-2210	(-3100)	(1.0)	(-1.1)
0.322*	ϵ	0.10	0.31	-3980	-2010			
0.242*		0.04	0.16	-5580	-3140			

B. Zn Component $Zn_{(s)} = Zn(\text{in alloy})_{(s)}$

x_{Zn}	Phase	a_{Zn}	γ_{Zn}	ΔF_{Zn}	$\Delta\bar{F}^{xs}_{Zn}$	$\Delta\bar{H}_{Zn}$	$\Delta\bar{S}_{Zn}$	$\Delta\bar{S}^{xs}_{Zn}$
0.00	α	0.00	0.17	- ∞	-3040	(-3600)	∞	(-0.6)
0.10		0.02	0.15	-7310	-3320	(-3100)	(4.8)	(0.2)
0.20		0.03	0.15	-6040	-3250	(-2500)	(4.1)	(0.9)
0.30		0.07	0.23	-4570	-2480	(-2400)	(2.5)	(0.1)
0.348*		0.11	0.30	-3910	-2080	(-2400)	(1.7)	(-0.4)
0.400*	β	0.11	0.28	-3910	-2320	(-1800)	(2.4)	(0.6)
0.50		0.20 (±.06)	0.41 (±.12)	-2770 (±500)	-1570 (±500)	(- 500)	(2.5)	(1.2)
0.558*		0.30	0.54	-2070	-1060	(200)	(2.6)	(1.5)
0.598*	γ	0.30	0.51	-2070	-1180	(- 800)	(1.5)	(0.5)
0.612		0.34	0.56	-1860	-1010	(- 500)	(1.6)	(0.6)
0.640*		0.44	0.68	-1440	- 670	(200)	(1.9)	(1.0)
0.678*	ϵ	0.44	0.81	-1440	- 370			
0.758*		0.62	0.82	- 830	- 350			

(Ref. 48)

Ag-Zn 399

TABLE 3

Heats of Formation of Solid AgZn Phases

$0.5\,Ag_{(s)} + 0.5\,Zn_{(s)} = Ag_{0.5}Zn_{0.5(s)}$

x_{Zn}	Phase	T, °K	ΔH
0.5	β	600	- 950(±50)
0.5	β′	324	-1585(±50)
0.5	ζ	324	-1535(±50)

TABLE 4

Integral Quantities for Liquid Alloys at 1050°K

$(1-x)Ag_{(\ell)} + xZn_{(\ell)} = Ag_{1-x}Zn_{x(\ell)}$

x_{Zn}	ΔF	ΔF^{xs}	x_{Zn}	ΔF	ΔF^{xs}
0.1	-1140	- 460	0.6	-2580	-1180
0.2	-1880	- 840	0.7	-2210	- 940
0.3	-2380	-1110	0.8	-1680	- 640
0.4	-2670	-1270	0.9	-1000	- 320
0.5	-2750 (±300)	-1300 (±300)			

TABLE 5

Partial Molar Quantities for Liquid Alloys at 1050°K

	Ag Component $Ag_{(\ell)} = Ag(\text{in alloy})_{(\ell)}$				Zn Component $Zn_{(\ell)} = Zn(\text{in alloy})_{(\ell)}$			
x_{Zn}	a_{Ag}	γ_{Ag}	$\Delta\bar{F}_{Ag}$	$\Delta\bar{F}^{xs}_{Ag}$	a_{Zn}	γ_{Zn}	$\Delta\bar{F}_{Zn}$	$\Delta\bar{F}^{xs}_{Zn}$
0.0	1.00	1.00	0	0	0.00	0.09	- ∞	-5000
0.1	0.88	0.98	- 260	- 40	0.01	0.13	-9010	-4210
0.2	0.76	0.93	- 640	- 170	0.04	0.19	-6870	-3510
0.3	0.57	0.81	-1190	- 450	0.08	0.28	-5170	-2660
0.4	0.39	0.65	-1960	- 890	0.16	0.41	-3750	-1840
0.5	0.25 (±.04)	0.49 (±.07)	-2950 (±300)	-1500 (±300)	0.30 (±.05)	0.59 (±.09)	-2550 (±300)	-1100 (±300)
0.6	0.14	0.34	-4190	-2280	0.49	0.81	-1520	- 450
0.7	0.08	0.25	-5410	-2900	0.67	0.95	- 840	- 100
0.8	0.04	0.22	-6510	-3150	0.80	1.00	- 480	- 10
0.9	0.02	0.22	-8000	-3200	0.90	1.00	- 220	0
1.0	0.00	0.21	- ∞	-3240	1.00	1.00	0	0

(Ref. 48)

396 Ag-Zn

Liquid Alloys. Selected free energies were taken from vapor pressure measurements of Schneider and Schmid (1942), 973°-1123°K, x_{Zn} = 0.30-0.85. Results were extrapolated to x_{Zn} = 0 in such a way that the Gibbs-Duhem integration would yield a ΔF at x_{Zn} = 0.5 which was consistent with the selected values for the solid. The strong assymetry of the results is in accord with the $\Delta\bar{F}_{Zn}$ values calculated along the liquidus from the solid values. For the calculation ideal entropies of formation were assumed. The temperature coefficients of Schneider and Schmid were rejected as inaccurate.

Part II. Tables

Ag Atomic Weight = 107.880

Zn Atomic Weight = 65.38

TABLE 1

Integral Quantities for Solid Alloys at 873°K

$$(1-x)Ag_{(s)} + xZn_{(s)} = Ag_{1-x}Zn_{x(s)}$$

x_{Zn}	Phase	ΔF	ΔH	ΔS	ΔF^{xs}	ΔS^{xs}
0.10	α	- 890	- 400	0.56	- 330	-0.09
0.20		-1520	- 660	0.99	- 650	0.00
0.30		-1990	- 870	1.28	- 930	0.08
0.348*		-2150	- 970	1.35	-1030	0.07
0.40*	β	-2290	(- 650)	(1.88)	-1120	(0.54)
0.50		-2470	- 750	1.97	-1270	0.59
		(±500)	(±50)	(±.6)	(±500)	(±.6)
0.558*		-2460	(- 670)	(2.05)	-1270	(0.69)
0.598*	γ	-2430	(-1090)	(1.53)	-1260	(0.19)
0.612		-2410	-1070	1.53	-1250	0.20
0.640*		-2360	(-1010)	(1.55)	-1230	(0.25)
0.678*	ϵ	-2260			-1170	
0.758*		-1980			-1020	

(Ref. 48)

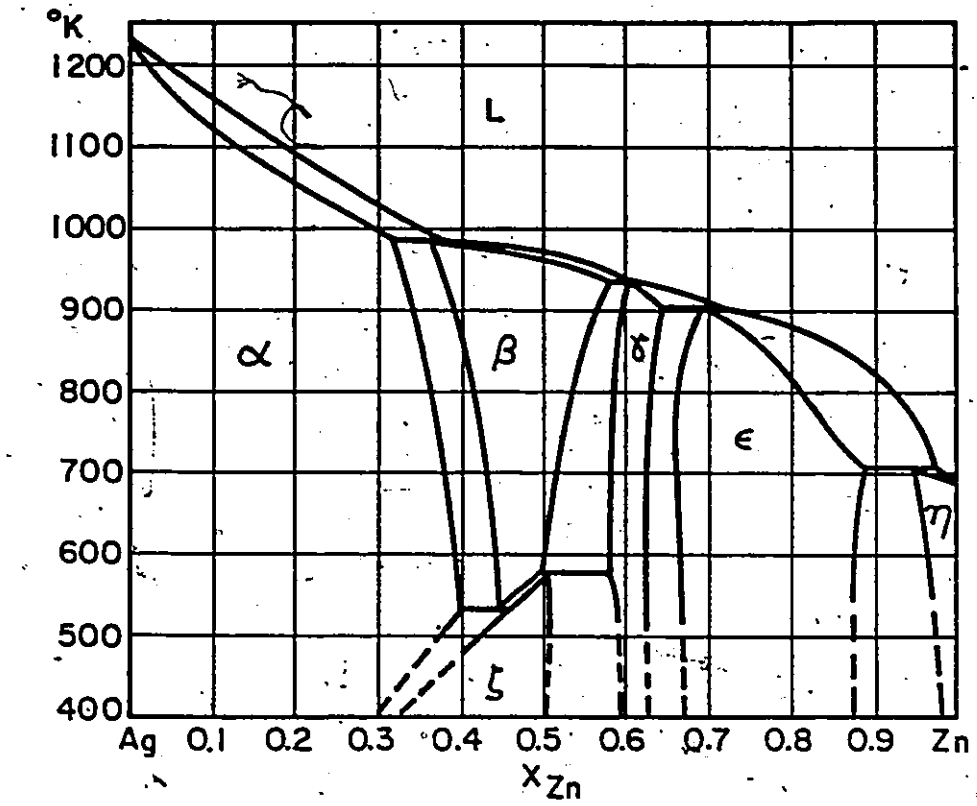

SILVER-ZINC SYSTEM, 873 °K

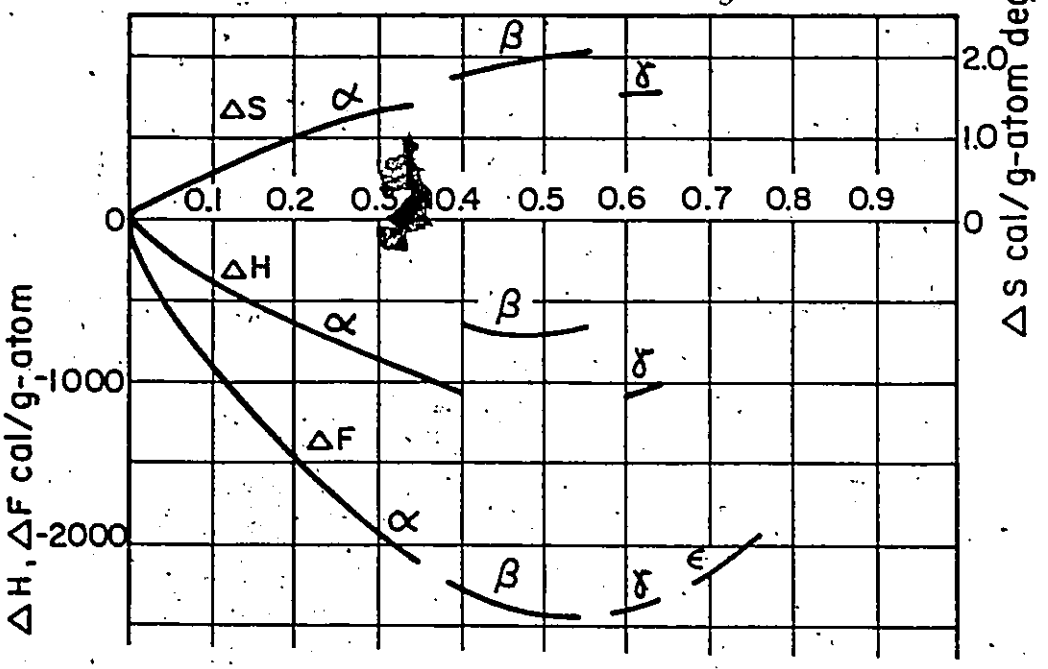

(Ref. 48)

samples, compared with the (n, γ)-damaged samples. (O 38)

Ag_3Sn: Hg Diffusion. Concentration profiles for Hg in Ag_3Sn amalgam were measured at temperatures from 20-100 C using X-ray energy spectra to depths of 30 μm from the boundary. The diffusion coefficient is described by the Arrhenius parameters

$$D_o = 4.2 \text{ cm}^2 \text{ s}^{-1}$$

$$Q = 18.6 \text{ kcal mole}^{-1}. \quad \text{(E 155)}$$

Ag-Zn: Zn Diffusion. Diffusion studies were made in the alpha and beta phases of the silver-zinc system at 600 C with vapor-solid and solid-solid diffusion couples in order to determineintrinsic diffusion coefficients and interdiffusion coefficients. Intrinsic diffusion coefficients, D_{Zn} and D_{Ag}, determined experimentally for both α and β alloys, were compared with those predicted from the models of Darken, Manning, and Dayananda with the aid of thermodynamic and single crystal tracer diffusion data. The experimental values of D_{Zn} were close to those predicted by the models of Darken and Manning, while the experimental D_{Ag} values were higher than those determined by both models. The experimental values of the ratio, D_{Zn}/D_{Ag}, were found to be lower than those predicted by either Darken's or Manning's relations. Also, Dayananda's model was found to be inapplicable with the available tracer diffusion data. This disagreement is considered to reflect the inadequacy of the single crystal tracer diffusivities in the analysis of intrinsic diffusion in polycrystalline Ag-Zn alloys. (Figure 2). (E 128)

Al, Au and Al-Zn: Point Defects. Hall et al. employed positron-lifetime measurements to study defects in specimens of pure aluminum, pure gold, and aluminum-1.7-at.%-zinc, in which the equilibrium concentration of vacancies was high enough to alter positron lifetimes. Analysis of data from lifetime measurements on pure aluminum at temperatures between 200 and 400 C, and on pure gold at temperatures between 360 and 780 C yielded monovacancy formation energies of $E^F_{1V} = 0.62 \pm 0.02$ eV for aluminum and $E^F_{1V} = 0.96 \pm 0.03$ eV for gold assuming no temperature dependence in the specific positron trapping rate. The fit to the data was significantly improved by assuming a temperature dependence in the specific trapping rate of $T^{1.2 \pm 0.3}$ for aluminum and $T^{0.5 \pm 0.2}$ for gold. The best-fit formation energies corresponding to these temperature dependences were $E^F_{1V} = 0.69 \pm 0.03$ eV for aluminum and $E^F_{1V} = 1.00 \pm 0.03$ eV for gold. Equilibrium measurements between 200 and 400 C in aluminum-1.7-at.%-zinc yielded a value for the binding energy of vacancies to impurities $E^B_{VP} = -0.09 \pm 0.03$ eV assuming no temperature dependence in the specific trapping rate. The fit was improved by assuming a temperature dependence in the specific trapping rate of $T^{1.1 \pm 0.2}$, corresponding to a best-fit value for the binding energy of $E^B_{VP} = +0.04 \pm 0.07$ eV. There is a positive temperature dependence in the specific positron trapping rate and vacancies are not strongly bound to zinc impurity atoms in aluminum. (P 53)

Al: Point Defects. Nicolaescu interpreted internal friction, dislocation migration and quenching experiments of aluminum in terms of a bulk process in which vacancies migrate

towards dislocations. The mean free path of vacancy migration is 10^5 times larger than that of impurity migration. Only ~0.3 % of the migrating vacancies reached the external surface of Al grains. (P 69)

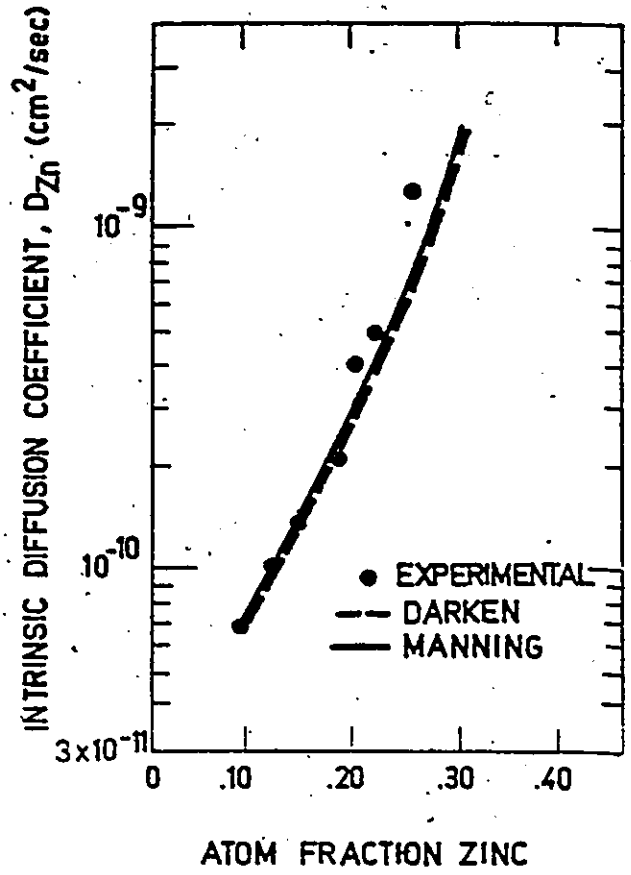

Figure 2. Intrinsic diffusion coefficient of Zn in Ag-Zn alloys. Comparison of experimental values of D_{Zn} with those predicted from various models at 600 C. (E 128)

Al: Vacancy Formation. Positron annihilation measurements in aluminum have been analyzed assuming a temperature dependent vacancy formation energy E as suggested by Popovic et al. and Seeger (1970). Because of a largely compensating variation in the entropy, the effect on the count rate is surprisingly small. (P 95)

Al: Impurity-Vacancy Interactions. High-purity Al, doped with impurities, was quenched to introduce vacancies and annealed to make these defects associate with the impurity atoms. Absorber experiments were done with ^{119}Sn and ^{57}Fe, while source experiments were made with ^{57}Co. Perturbations in the Moessbauer signal, mean shift of line position, and some line broadening were observed. The nature of the defect reactions involved was

(Ref. 105)

(A6) Ag-Cd and Ag-Zn, Interdiffusion

Ugaste et al. employed electron microprobe analysis to study the interdiffusion in the Ag-Cd (figure 1) and Ag-Zn (figure 2) systems. Materials used were 99.99 % Ag, electrolytic Zn, and Cd containing Pb-0.02, Zn-0.01, Cu-0.01, and Fe-0.003 wt % as major impurities. The results obtained are in good agreement with Darken's theory.

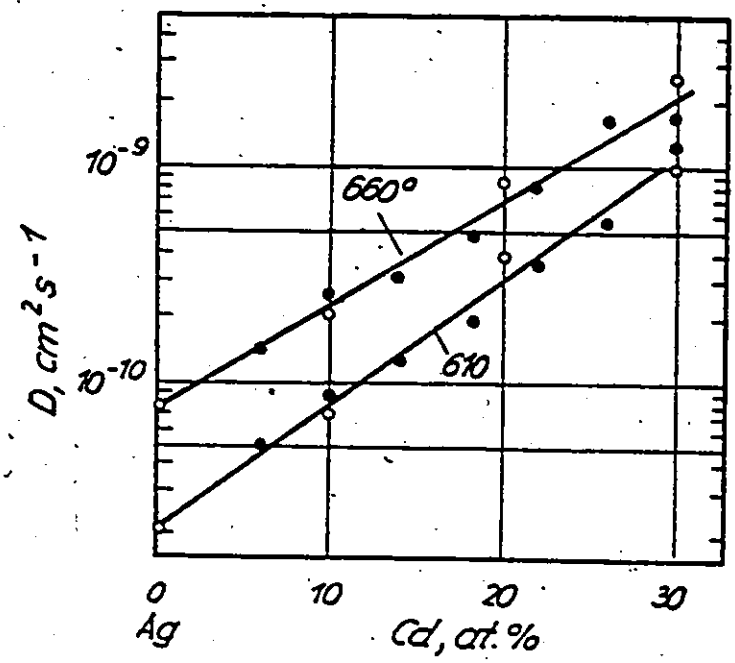

Fig. 1 - Interdiffusion in α-Ag-Cd: •-Ref. (A6), o-Ref. (A7)

(A8) Co in Ag, Impurity Tracer Diffusion

Using the serial sectioning technique, Badrinarayanan and Mathur reinvestigated the diffusion of Co^{60} in Ag (spectroscopic pure Johnson Mattey material) and reported results (table 1) in good agreement with the earlier work of Hirone et al. (A10). The authors suggested that the later results obtained by Hirano et al. (A9) by the residual

(A6) Ugaste, Yu. E., Pimenov, V. N., Khlomov, V. S.: Fiz. Met. + Metalloved. 36, No. 1 (1973)211-3

(A7) Darken, L. S.: Trans. AIME 175(1948)184

(A8) Badrinarayanan, S., Mathur, H. B.: Indian J. Chem. 11, No. 5(1973)465-7

(A9) Hirano, K., Cohen, M., Averbach, B. L.: Acta Metall. 11(1963)463

(A10) Hirone, T., Miura, S., Suzuoka, T.: J. Phys. Soc. Japan, 16(1961)455

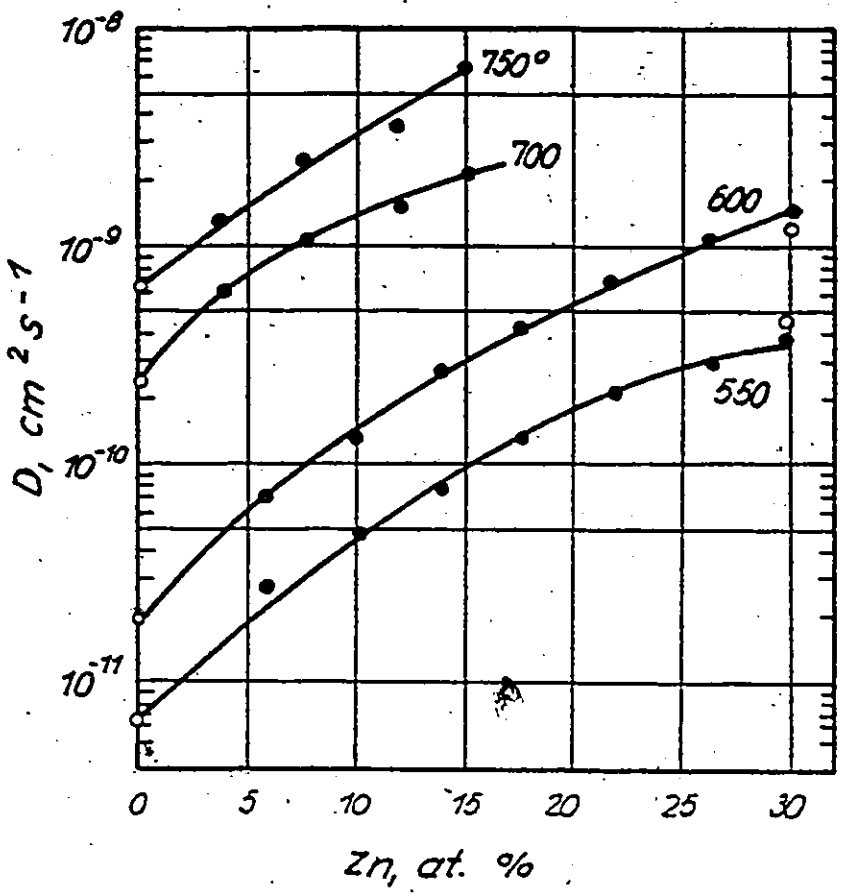

Fig. 2 - Interdiffusion in α-Ag-Zn: •-Ref. (A6), o-Ref. (A7)

TABLE 1. IMPURITY TRACER DIFFUSION OF Co^{60} IN Ag (A8)

Temp. C	Annealing Time s	D cm^2s^{-1}
925	2.511×10^5	5.01×10^{-9}
910	0.297×10^5	4.12×10^{-9}
910	0.297×10^5	4.19×10^{-9}
884	1.872×10^5	3.38×10^{-9}
884	1.872×10^5	3.26×10^{-9}
850	2.511×10^5	1.25×10^{-9}
850	2.511×10^5	1.11×10^{-9}
814	2.520×10^5	5.14×10^{-10}
814	2.520×10^5	5.19×10^{-10}
795	0.720×10^5	3.04×10^{-10}

(Ref. 106)

APPENDIX 3

Table A-3-1

Statistical Results for Ag-1.8, 7.5, 10.9, 12.9 and 18.7 wt % Zn Alloys

Alloy	Slope	Intercept	Standard Deviation	Standard Deviation in Slope	Standard Deviation in Intercept	Correlation Factor
1.8						
High	.0028	-.059	.031	.0001	.101	.98
Average	.0024	-.0655	.052	.0001	.101	.94
Low	.0024	-.0962	.035	.00009	.101	.97
7.5	.00066	.00418	.005	.00002	.100	.99
10.9	.00042	.00272	.014	.00003	.100	.94
12.9			.050	.00012	.103	.43
18.7	.00018	-.000877	.0005	.000003	.100	.97

Figure A.3.1

Colour Optical Photomicrographs

(a) Internal oxidation zone, Ag-7.54 wt % Zn, oxidation time 10 hr, polarized light from a tungsten lamp using a Nomarski interference lens, 170×

(b) Internal oxidation zone, Ag-10.9 wt % Zn, oxidation time 10 hr, 170×


100 μm
a

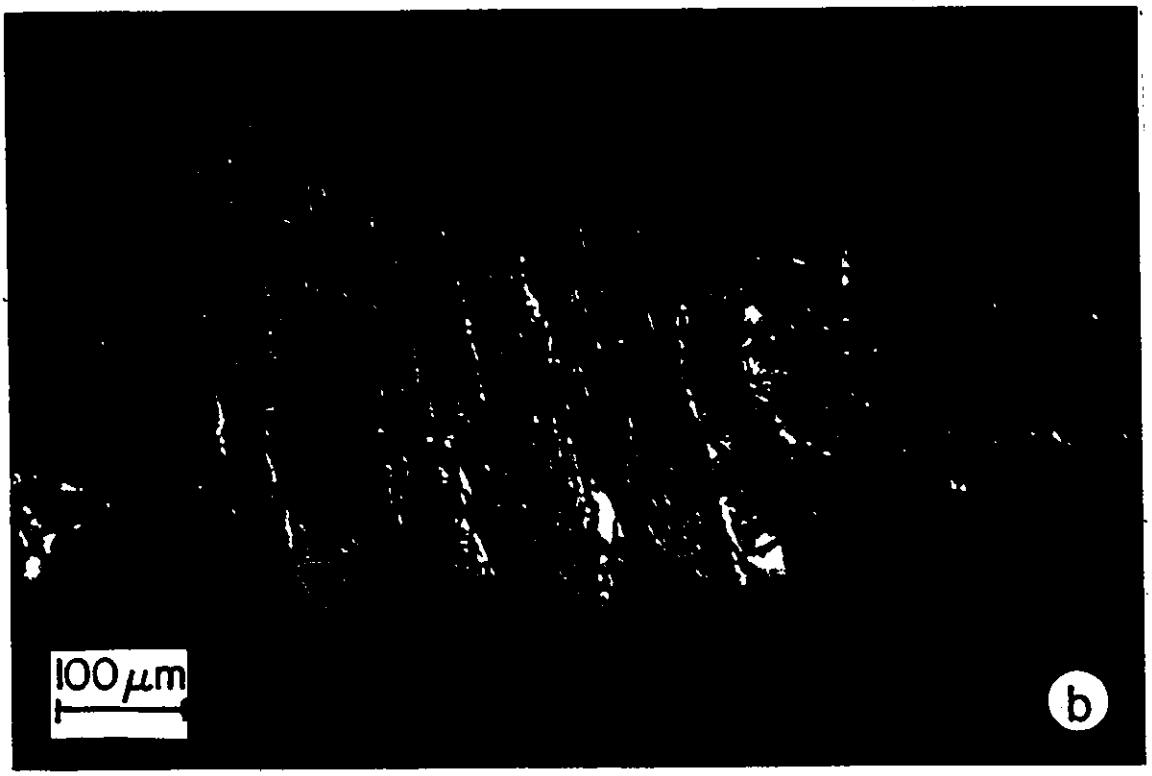
100 μm
b

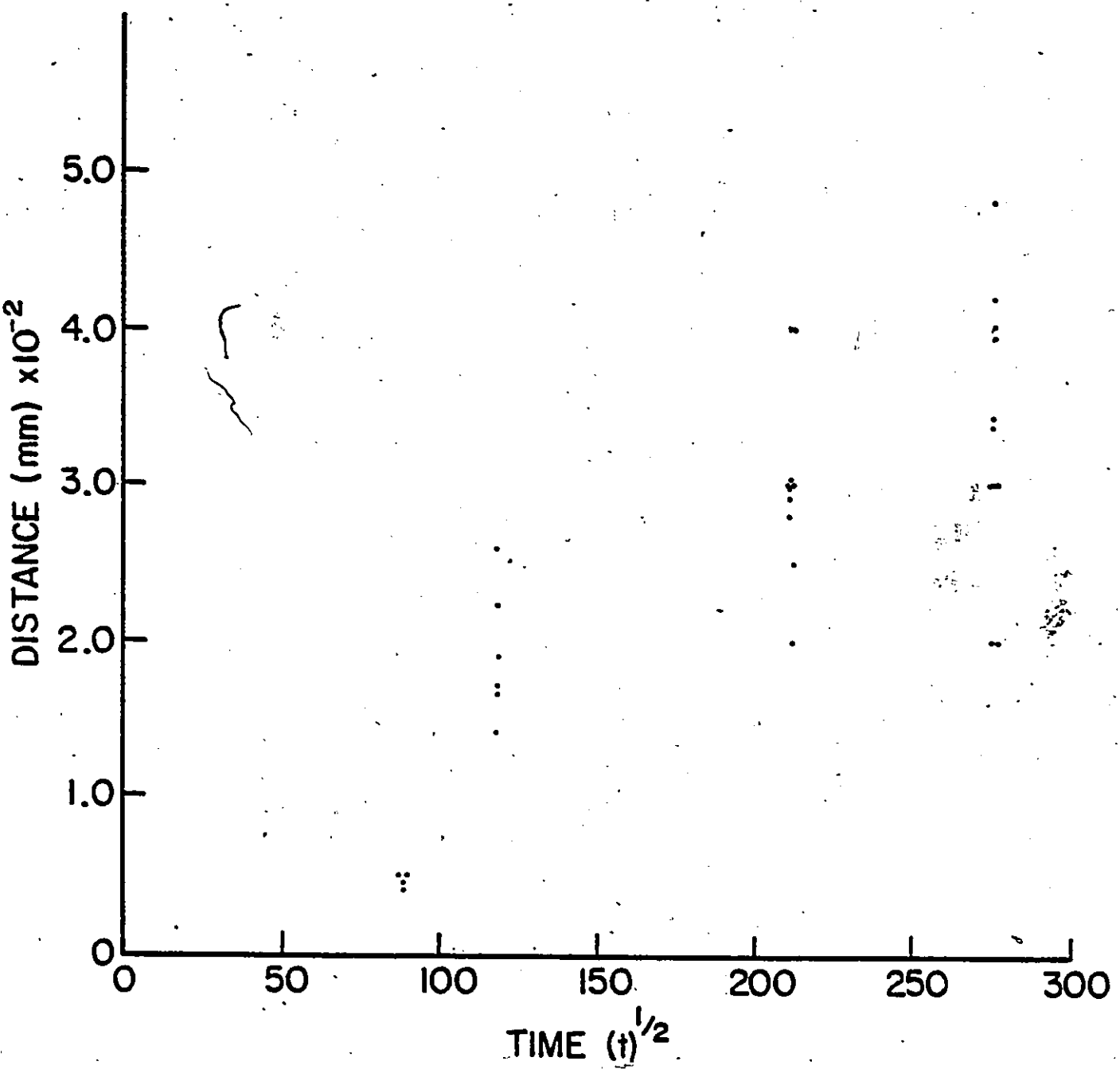

Figure A.3.2 x vs $(t)^{1/2}$, Ag-12.9 wt % Zn

Figure A.3.3

SEM and X-ray Point Count Analysis
for Figures 4.19 (a) + (b)

(a) Point count analysis of the external and internal scales, and matrix. Results given in Table A-3-2

(b) Point count analysis of the external scale and matrix. Results given in Table A-3-3

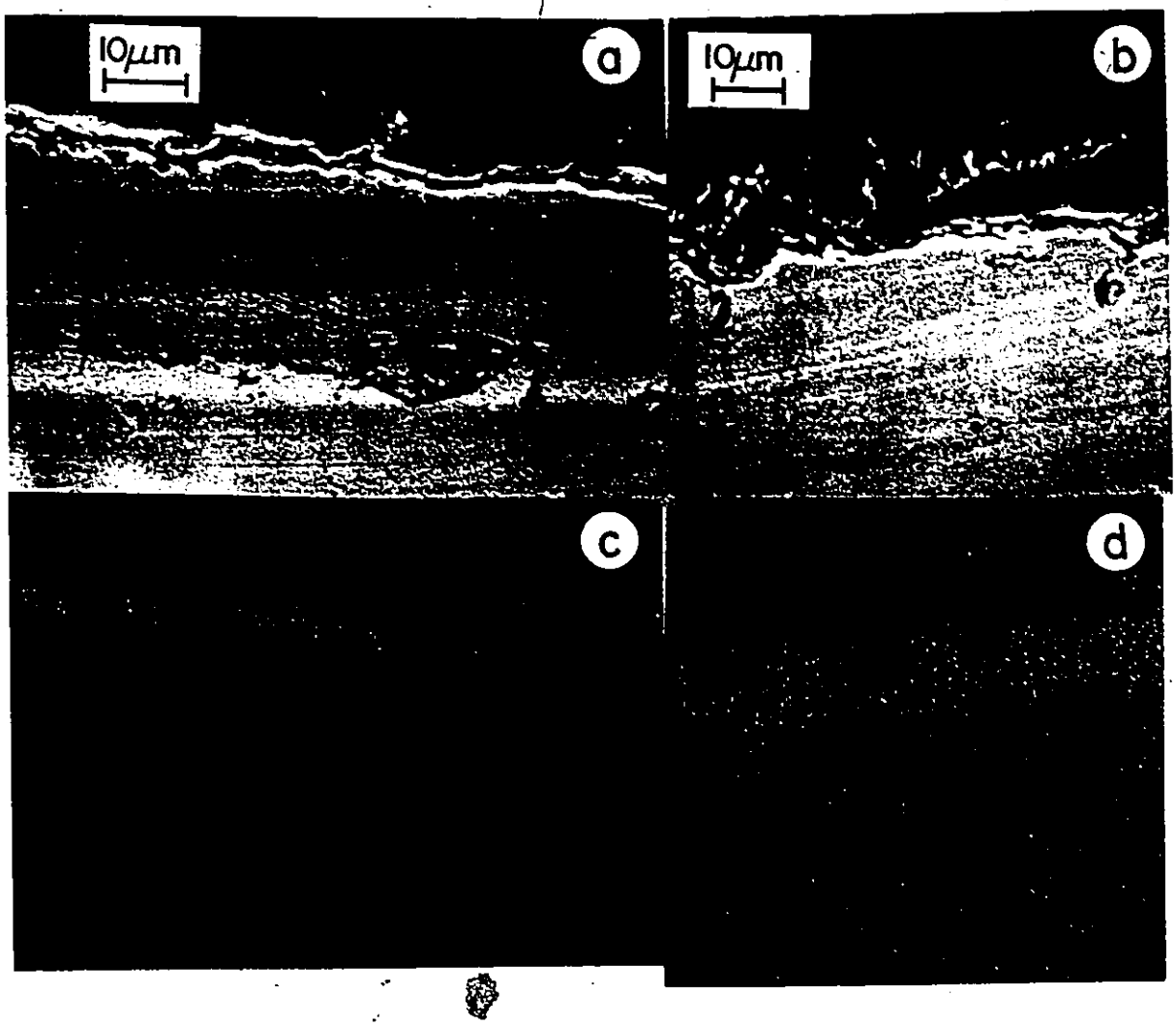
10μm
a
10μm
b
c
d

Table A-3-2

Results for Figure A.3.3 a)

a) Point 1

No.	ECL	Centroid	FWHM	Area	Left	Right	Element
1	1	1.07	0.12	1862	10	31	Zn
2	1	8.72	0.15	5105	608	629	Zn
3	1	9.65	0.10	725	682	702	Zn

b) Point 2

No.	ECL	Centroid	FWHM	Area	Left	Right	Element
1	1	3.04	0.11	3750	164	185	Ag
2	1	3.24	0.01	367	191	201	Ag
3	1	8.69	0.14	303	607	627	Zn

c) Point 3

No.	ECL	Centroid	FWHM	Area	Left	Right	Element
1	1	3.04	0.12	5250	164	185	Ag
2	1	3.24	0.09	971	184	197	Ag
3	1	8.68	0.09	304	606	627	Zn

Table A-3-3

SEM and X-ray Point Count Analysis for Figure A.3.3 (b)

a) Point 1

No.	ECL	Centroid	FWHM	Area	Left	Right	Element
1	1	1.07	0.12	4067	10	30	Zn
2	1	8.68	0.16	4566	606	626	Zn
3	1	9.64	0.15	570	680	701	Zn

b) Point 2

No.	ECL	Centroid	FWHM	Area	Left	Right	Element
1	1	1.07	0.11	2032	10	31	Zn
2	1	8.69	0.14	4533	606	626	Zn
3	1	9.63	0.11	778	680	701	Zn

c) Point 3

No.	ECL	Centroid	FWHM	Area	Left	Right	Element
1	1	3.04	0.13	3729	164	185	Ag
2	1	3.16	0.06	83	183	197	Ag

APPENDIX 4

4-A-1 Determination of $N_o^{(S)} \cdot D_o$

Ag-1.8 wt % Zn

$$N_o^{(S)} = 6.69\times10^{-2} \exp(-11{,}860/RT)$$

$$= 6.69\times10^{-2} \exp(-11{,}860/1.987\times823)$$

$$= 4.7\times10^{-5} \text{ (oxygen atom fraction)} \qquad (19)$$

$$D_o^{Ag} = 3.66\times10^{-3} \exp[-11{,}000/1.987\times823]$$

$$= 4.4\times10^{-6} \text{ cm}^2/\text{sec} \qquad (19)$$

$$\zeta = 2\left[\frac{N_o^{(S)}}{2\nu N_B^o}\right]^{1/2} [D_o t]^{1/2} \qquad (2\text{-}8)$$

$$[N_o^{(S)} \cdot D_o]^{1/2} = \frac{\zeta}{2} \frac{[2\nu N_B^{(o)}]^{1/2}}{(t)^{1/2}}$$

$$= \frac{.027}{2} \frac{[2N_B^{(o)}]^{1/2}}{140}$$

$$= 1.86\times10^{-8} N_B^{(o)}$$

$$= 1.86\times10^{-8} (.03)$$

$$= 5.6\times10^{-10} \text{ atom fraction cm}^2/\text{sec}$$

For literature $N_o^{(S)} \cdot D_o = 2.1\times10^{-10}$ atom fraction cm^2/sec

Ag-7.5 wt % Zn

$N_B^{(o)} = .12$

$$\frac{.011}{2}\,\frac{[2.12]^{1/2}}{160} = [N_o^S \cdot D_o]^{1/2}$$

$$2.8\times10^{-10} = N_o^S \cdot D_o \quad \text{atom fraction cm}^2/\text{sec}$$

Ag-10.9 wt % Zn

$N_B^{(o)} = .17$

$$\frac{.01}{2}\,\frac{[2\cdot.17]^{1/2}}{230} = [N_o^S \cdot D_o]^{1/2}$$

$$1.6\times10^{-10} = N_o^S \cdot D_o \quad \text{atom} \cdot \text{fraction cm}^2/\text{sec}$$

REFERENCES

1. Rapp, R.A., Corrosion - National Association of Corrosion Engineers, 21, 382 (1965).
2. Meijering, J.L., and Druyesteyn, M.J., Philips Res. Rept., 2, 81 & 260 (1947).
3. Chaston, J.C., J.Inst. Metals, 71, 23 (1945).
4. Wood, D.L., Trans. AIME, 215, 926 (1959).
5. Meijering, J.L., Trans. AIME, 218, 968 (1960).
6. Martin, J.W., and Smith, G.C., J. Inst. Metals, 83, 153 and 417 (1954-55).
7. de Jong, J. J., Ingenieus, 64, (1952).
8. Preston, O., and Grant, N.J., Trans. AIME, 221, 164 (1961).
9. Whittle, D.P., El-Dahsahan, M.E., and Stringer, J., Corros. Sci., 17, 879 (1977).
10. Peddler, D.J., Trans. AIME, 9A, 659 (1978).
11. Bradford, S.A., Trans. AIME, 230, 1400 (1964).
12. Van Vlack, L.V., Inst. Met. Rev., Sept., 207 (1977).
13. Chatterjee, R., and Fischer, Trans. AIME, 9A, 1553 (1978).
14. Swisher, J. H., Trans. AIME, 242, 1035 (1968).
15. Mayer, P., and Smeltzer, W.W., Can. Met. Quart., 12, 11 (1973).
16. Rhines, F.N., Johnston, W.A., and Anderson, N.A., Trans. AIME, 147, 205 (1942).

17. Schwarzkopf, W., Z. Electrochem., 63, 830 (1959).

18. Dietrich, I.D., and Koch, L., Z. Metalk., 50, 31 (1959).

19. Schenck, I., Schmidtmann, E., and Muller, H., Arch. Eisenhuttenwesen, 31, 121 (1960).

20. Rapp, R.A., Frank, D.F., and Armitage, J.V., Acta Met., 12, 505 (1964).

21. Rhines, F.N., Trans. AIME, 137, 246 (1940).

22. Maak, F., Z. Metalk., 52, 545 (1961).

23. Rapp, R.A., and Colson, H.D., Trans. AIME, 236, 1616 (1966).

24. Verfurth, J.E., and Rapp, R.A., Trans. AIME, 230, 1310 (1964).

25. Bosch, R.A., Lennel, F.V., and Ansell, G.S., Trans. AIME, 57, 960 (1964).

26. Smeltzer, W.W., and Whittle, D.P., J. Electrochem. Soc., 125, 7, 1116 (1978).

27. St. Pierre, G.R., and Blackburn, R.D., Trans. AIME, 242, 24 (1968).

28. Feldman, S.E., and Kirkaldy, J.S., Can. Met. Quart., 13, 625 (1974).

29. Bolze, G., Coates, D.E., and Kirkaldy, J.S., Trans. AIME, 62, 794 (1969).

30. Aaranson, H. I., and Lee, J.K., 'The Kinetic Equations of Solid-Solid Nucleation Theory', Lectures on the Theory of Phase Transformations, AIME, New York, 83 (1977).

31. Sharma, R.C., and Purdy, G.R., Met. Trans., 5, 939 (1974).

32. Hilliard, J.E., Phase Transformations, ASM, Metals Park Ohio, 497 (1968).

33. Ashby, M.F., and Smith, G.C., J. Inst. Metals, 91, 182 (1962-63).

34. Dondiya, Y.E.P., Rosenburg, V.M., and Teplitsky, M.D., Fiz. Metal. Metalloved., 38, 3, 536-540 (1974).

35. Bolsaitis, P., and Kahlweit, M., Acta Met., 15, 765 (1967).

36. Wood, S., Adamans, D., Guha, A., Soffa, W.A., and Meier, G.H., Met. Trans. A, 6A, 1793 (1973).

37. Peddler, D.J., Met. Trans. A, 9A, 659 (1978).

38. Swann, P.R., Weissmann, S., and Wriedt, D.F., Trans. AIME, 230, 1306 (1964).

39. Podgurgski and Davis, Trans. AIME, 230, 731 (1964).

40. Peddler, D.J., Boyes, E.D., and Smith, G.C., Met. Sci., Dec., 437 (1964).

41. Darken, L.S., Trans. A.S.M., 54, 613 (1961).

42. Jack, K.H., Heat Treatment, Dec., 39 (1973).

43. Jack, D.H., Acta Met., 24, 137 (1975).

44. Wagner, R., and Brenner, S.S., Acta Met., 26, 197 (1978).

45. Kahlweit, M., Prog.Chem.Solid St. 'The Structure of a Precipitate as Determined by the Interplay of Nucleation, Growth and Ageing', 2,134 (1965).

46. Böhm, G., and Kahlweit, M., Acta Met., 12, 641 (1964).

47. Rapp, R.A., Acta Met., 9, 730 (1961).

48. Hultgren, Desai, Hawkins, Gleisen and Kelly, Selected Values of the Thermodynamic Properties of Binary Alloys, ASM, Metals Park, Ohio, 396-399 (1973).

49. Pickering, H.W., J. Electrochem. Soc., 119, 641 (1972).

50. A.S.T.M., Annual book of ASTM Standards (Chemical Analysis), 261 (1978).

51. Cullity, B.D., Elements of X-ray Diffraction, Addison-Wesley, Inc. Don Mills, Ontario, 94, 153 (1967).

52. Rhines, N., Trans. AIME, Feb., 246 (1940).

53. Rhines, N., and Nelson, B., Trans. AIME, 156, 171 (1944).

54. Dunn, J., J. Inst. Metals, 46, 25 (1931).

55. Raether, H., J. Phys. Radium, 11, 11 (1950).

56. Lucas, R., J. Inst. Metals, 99, 69 (1971).

57. Joint Committee on Powder Diffraction Standards, Inorganic Compounds. Powder Diffraction File Microfiche Index of Frequently Encountered Phases, Swarthmore, Penn. U.S.A., 1-444-08 (1974).

58. Barin, and Knackle, Thermochemical Properties of Inorganic Substances, Germany, 879 (1973).

59. Hindam, H., Microstructure and Growth of Al_2O_3 on Ni-Al Alloys, Ph.D. Thesis, McMaster University, 104 (1979).

60. Brigham, R. J., Purdy, G.R., and Kirkaldy, J.S., Crystal Growth, 161 (1967).

61. Purdy, G.R., Private Communication.

62. Liesegang, R. E., Photo. Archiv., 21, 221 (1896).

63. Liesegang, R. E., Naturw. Wschr., 11, 353 (1896).

64. Klueh, R. L., and Mullis, W. W., Acta Met., 17, 59 (1969).

65. Klueh, R. L., and Mullins, W. W., Acta Met., 17, 69 (1969).

66. Wagner, C., J. Colloid Sci., 5, 85 (1950).

67. Giggins, C.S., and Pettit, F. S., Trans. AIME, 245 2495 (1969).

68. Statt, F. H., and Wood, G. C., Corros. Sci., 17, 647 (1977).

69. Wood, G. C., and Statt, F. H., Brit. Corros, J., 6, 247 (1971).

70. Ugaste, Yu. E., Pimenov, V.N., and Khlomov, V.S., Fiz. Met. and Metalloved., 36, No. 1, 211-3 (1973).

71. Kirkaldy, J.S., "Ternary Diffusion and Its Relationship to Oxidation and Sulphidation", Oxidation of Metals and Alloys, A.S.M., Metals Park, Ohio, 101 (1971).

72. Clark, J. B., and Rhines, F.N., Trans. A.S.M., 51, 199 (1959).

73. Kirkaldy, J. S., and Brown, L. C., Can. Met. Quart., 2, 89 (1963).

74. Coates, D.E., and Dalvi, A. D., Oxid. Metals, 2, 331 (1970).

75. Wagner, C., Z. Physik. Chem., B21, 25 (1933).

76. Fehlner, F. P., and Mott, N. F., "Oxidation in the Thin-Film Range", Oxidation of Metals and Alloys, A.S.M., Metals Park, Ohio, 37 (1971).

77. Kubaschewski, and Hopkins, Oxidation of Metals and Alloys, Butterworth and Co. Ltd., Toronto, 53 (1962).

78. Takahashi, N., and Mihama, H., J. Chim. Phys. 53, 633 (1956).

79. Pilling, N.B., and Bedworth, R. E., J. Inst. Metals, 29, 529 (1923).

80. Gebhardt, V. E., Z. Metallk., 37, 87 (1946).

81. Douglass, D. L., "Exfoliation and The Mechanical Behaviour of Scales", Oxidation of Metals and Alloys, A.S.M., Metals Park, Ohio, 138 (1971).

82. Kubaschewski and Hopkins, Oxidation of Metals and Alloys, Butterworth and Co. Ltd., Toronto, 71 (1962).

83. Smeltzer, W. W., and Young, D. J., Progress in Solid State Chem., 10, 17 (1975).

84. L ucas, R. W., J. Inst. Met., 99, 69 (1971).

85. Pfefferkorn, G., Naturwiss., 40, 551 (1953); Z. Metallk., 46, 204 (1955).

86. Goursat, A. G., Oxidation of Iron, M.Sc., McMaster University, 109 (1972).

87. Takagi, R., J. Phys. Soc., Japan 12, 1212 (1957).

88. Poidassi, J., Acta. Met., 6, 778 (1958).

89. Gullbransen, E. A., in "Processus de Nuclèation dans les Réaction des Gaz sur les Métaux et Problèmes

connexes" published in Mem. Sci. Rev. Met., LXll, 253 (1965).

90. Talbot, S., and Bigot, J., ibid., 261 (1965).

91. Holt, J.B., and Himmel, L., J. Electrochem. Soc., 116, 1569 (1969).

92. Hauffe, K., Oxidation of Metals, Plenum Press, New York, 81 (1965).

93. Dunn, J. S., J. Inst. Met., 46, 25 (1931).

94. Rhines, F. N., and Nelson, B. J., Trans. AIME, 156, 171 (1944).

95. Kubaschewski, and Hopkins, Oxidation of Metals and Alloys, Butterworth and Co. Ltd., Toronto, 25 (1962).

96. Kofstad, P., Nonstoichiometry, Diffusion and Electrical Conductivity in Binary Metal Oxides, Wiley and Sons., Inc., Toronto, 334 (1972).

97. Mallwo, E., and Stoeckmann, F., Ann. Phys., L.p.z. 3, 240 (1948).

98. Hogarth, C. A., Z. Phys. Chem., 198, 41 (1951).

99. Von Baumbach, H. H., and Wagner, C., Z. Phys. Chem. (B), 22, 199 (1933).

100. Bevan, D. J. M. and Anderson, J. S., Faraday Soc. Disc., 8, 238 (1950).

101. Hauffe, K., and Block, J., Z. Phys. Chem., 196, 438 (1951).

102. Hauffe, K., Oxidation of Metals, Plenum Press, New York, 202 (1965).

103. Cope, J. O., Trans. Faraday Soc., 57, 493 (1961).

104. Hauffe, K., Oxidation of Metals, Plenum Press, New York, 209 (1965).

105. Wohlbier, F. H., Diffusion and Defect Data, Merkel and Co., Switzerland, 11, 4 and 5 (1975).

106. ibid., 8, 2 and 3 (1974).